

# **Simultaneous Measurement of Strain and Temperature in a Gasket for Condition Monitoring**

Rizkiawan Fauzan

Faculty 4: Electrical Engineering and Computer Science  
Hochschule Bremen

A thesis submitted to fulfil the requirements for the degree of Master of Science  
in Electronics Engineering

Supervisor:

Prof. Dr. rer. nat. Ludger Kempen  
Daniel Gräbner. M.Sc.

## **PREFACE**

The content written in this master thesis is based on the research conducted at IMSAS institute in Universität Bremen. No plagiarism is conducted in the writing of this thesis. External contents such as references and citations included in this thesis have been credited accordingly to their respective author.

**Rizkiawan Fauzan**

## **ACKNOWLEDGEMENT**

The author would like to express his wholehearted gratitude to both of his supervisor Mr. Prof. Dr. rer. nat. Ludger Kempen and Mr. Daniel Gräbner. M.Sc. for their unrelenting support during the whole duration of this master thesis. Their constant supervision, motivation, and guidance contribute greatly in increasing the knowledge of the author regarding the whole processes involved in the completion of this master thesis.

The author would also like to thank Mr. Niclas Schwarz for his assistance in the cleanroom during the fabrication process of the sensors. His technical support and guidance in the cleanroom not only support the fabrication of the sensors but also contribute greatly in increasing the knowledge of the author regarding the equipment used in the cleanroom.

Lastly, the author would like to thank his family and friends for their constant support and motivation throughout the completion of this thesis.

## Table of Content

CHAPTER 1 .....	10
1.1. Motivation.....	10
1.2. Proposed approach and method .....	12
1.3. Existing work and scientific literature .....	14
1.3.1. Process Signature .....	14
1.3.2. Structural health monitoring .....	15
1.3.3. Sensor Integration .....	16
1.3.4. Leakage detection method .....	17
1.3.5. Determining the condition of a gasket by means of strain measurement.....	18
1.3.6. Simultaneous measurement of strain and temperature with two resistive strain gauges ....	19
CHAPTER 2 .....	21
2.1. Compression Set (CS).....	21
2.1 Polymer Ageing .....	23
2.1.1. Physical Ageing of Polymers .....	23
2.1.2. Thermal Ageing of Polymer at Elevated Temperatures.....	29
2.2. Viscoelasticity of Polymeric Structure .....	34
2.2.1. Kelvin-Voigt Model.....	35
2.2.2. Maxwell Model .....	37
2.2.3. Standard Linear Solid Model .....	39
2.3. Effect of Ageing on Polymeric Structure.....	40
2.4 Strain Gauge.....	41
2.4.1. Wheatstone Bridge.....	44
2.5 Temperature Dependency of Strain Gauge .....	48
2.6 Simultaneous Measurement of Strain and Temperature .....	49
CHAPTER 3 .....	51
3.1. Strain Gauge Materials Selection.....	51
3.1.1. Strain Gauge Active Elements, Conducting Paths and Contacts Materials .....	51
3.1.2. Strain Gauge Substrate Material .....	54
3.2. Strain Gauge Fabrication .....	56
3.3. Sensor Integration .....	69
3.4. Wire Bonding.....	72
3.5. Strain Gauge Characterization .....	72
3.5.1. Gauge Factor ( $G_f$ ) Characterization .....	73
3.5.2 Temperature Coefficient of Resistance (TCR) Characterization .....	74

3.7. Gasket Condition Monitoring .....	75
CHAPTER 4 .....	76
4.1. Fabrication Results.....	76
4.1.1. Platinum (Pt) & Gold (Au) strain gauges with Copper (Cu) contacts .....	76
4.1.2. Platinum (Pt) & Gold (Au) strain gauges with Gold (Au) contacts .....	78
4.1.3. Platinum (Pt) & Chromium (Cr) strain gauges with Gold (Au) contacts.....	80
4.1.4. Platinum (Pt) & Aluminium (Al) strain gauges with Gold (Au) contacts .....	82
4.1.5. Platinum (Pt) & Titanium (Ti) strain gauges with Gold (Au) contacts.....	83
4.2. Temperature Coefficient of Resistance (TCR) Characterization .....	83
4.3. Gauge Factor Characterization.....	87
4.4. Gasket Condition Monitoring .....	90
CHAPTER 5 .....	95
5.1. Conclusion .....	95
5.2. Future outlook.....	96
REFERENCES .....	98

## List of Figures

Figure 1: Leaks caused by unrecovered gasket.....	11
Figure 2: Polymer O-ring Gasket with Integrated Sensor.....	12
Figure 3: Half-Bridge Configuration (left) and Nested Configuration (right) .....	13
Figure 4: Different machining process described by the energies involved [13].....	14
Figure 5: Sensor integration inside polymer gasket for strain measurement [19]. .....	19
Figure 6: Compression set measurement setup using ISO 815 [28] or ASTM D 395 Method B standard [27] .....	22
Figure 7: Compression set test device for ASTM D 395 Method A standard using calibrated spring as the known load force [27]. .....	22
Figure 8: The free volume concept [31].....	24
Figure 9: Relation between Segmental Mobility, Free Volume, and Temperature. [31].....	25
Figure 10: Density difference between core and skin of a moulded polystyrene bar at 23°C ageing temperature. [7].....	26
Figure 11: Residual stress distribution of polystyrene bar in 1.5 mm thickness in the as moulded state and the annealed state. [7].....	27
Figure 12: Viscoelastic behaviour of polymer shown by its Young's modulus with respect to temperature and load frequency. [45] .....	35
Figure 13: Kelvin-Voigt model. [46] .....	36
Figure 14: Creep, relaxation, and recovery in Kelvin-Voigt model. [47].....	36
Figure 15: Maxwell's model of viscoelasticity. [48].....	38
Figure 16: Strain and stress with respect to time in stress relaxation. [48].....	38
Figure 17: Standard Linear Solid Model configuration. [47] .....	39
Figure 18: Creep, relaxation and recovery response of standard linear solid model. [47] .....	40
Figure 19: Foil strain gauge geometry. [50] .....	42
Figure 20: Relation between strain and electrical properties of a conducting path .....	43
Figure 21: Wheatstone bridge .....	44
Figure 22: Quarter bridge configuration. Strain gauge figure taken from [50].....	45
Figure 23: Half bridge configuration. Strain gauges figure taken from [50]. .....	46
Figure 24: Deformation in cantilever. [54] .....	47
Figure 25: Full bridge configuration. Strain gauge figure taken from [50] .....	47
Figure 26: Temperature compensation using two strain gauges [54] (left) temperature compensated half-bridge configuration (right) .....	48
Figure 27: Sensor elongation with respect to contact force applied to the gasket for three different embedded substrate materials. [53].....	55
Figure 28: Sensor design made in AutoCAD.....	56
Figure 29: Polyimide deposition on a spin coater.....	57
Figure 30: Polyimide Curing Temperature Profile .....	58
Figure 31: First strain gauge metal deposition.....	59
Figure 32: First strain gauge structuring by means of structuring the positive photoresist. Before exposure (left) and after exposure and development (right) .....	60
Figure 33: Result after wet etching of the first strain gauge and resist removal.....	60
Figure 34: Deposition of the second strain gauge metal on top of the already structured first strain gauge.....	61
Figure 35: Structure used for alignment. Alignment structure on the wafer noted by the orange colour, alignment structure on mask noted by the blue colour. Before alignment (left) and after alignment (right) .....	61

Figure 36: Second strain gauge structuring processes. Before exposure (left) and after exposure, development, metal etching, and resist removal (right) .....	62
Figure 37: Two types of nested strain gauges with different widths .....	63
Figure 38: Conducting path and contacts of the nested strain gauge sensor structured using wet etching.....	63
Figure 39: Copper conducting paths and contacts structuring process. Positive resist exposure (left) and after resist development, copper etching, and resist removal (right) .....	64
Figure 40: Undercuts in negative resist during development (noted by the red circles). Increased surface area caused by undercuts in the resist eases the resist removal process .....	65
Figure 41: Gold conducting paths and contacts structuring by lift-off process. Negative resist exposure (top left), gold sputtering to be used as conducting paths and contacts (top right), negative resist removal in an NMP solution (bottom middle) .....	65
Figure 42: Conducting path and contacts of the nested strain gauge sensor structured using lift off ...	66
Figure 43: Gold conducting paths and contacts by means of direct writing lithography.....	67
Figure 44: Polyimide etching structure. Structure used during masking lithography (top) and structure used during direct writing lithography (bottom) .....	67
Figure 45: Polyimide structuring process by means of dry etching using Inductively Coupled Plasma (ICP). Before exposure (left) and after exposure, resist development, polyimide etching, and resist removal (right) .....	68
Figure 46: Sensor singulation process, before (left) and after singulation (right). Singulation is made by making an incision on the gaps between the polyimide voids followed by peeling off the sensor from the wafer.....	69
Figure 47: Silicone mould used to fabricate the silicone gaskets .....	70
Figure 48: Von Mises stress distribution (N/mm <sup>2</sup> ) of the O-ring gasket with integrated sensor in various locations. [53].....	71
Figure 49: Integrated sensor in gasket .....	71
Figure 50: Wire bonding on top of the contacts of the sensor .....	72
Figure 51: Gauge Factor Characterization Apparatus (right) and the test specimen (left). .....	73
Figure 52: Temperature Coefficient of Resistance Characterization Apparatus.....	74
Figure 53: Compression plates configuration to be used as gasket ageing measurement.....	75
Figure 54: Fabricated platinum and gold strain gauges with copper contacts. Figure (a) represents strain gauges with 10 $\mu\text{m}$ width and Figure (b) represents strain gauges with 20 $\mu\text{m}$ width. ....	77
Figure 55: Dimple generated on the metallic film during sputtering.....	77
Figure 56: Shortages in the conducting paths for Pt & Au nested strain gauges structured using lift-off .....	78
Figure 57: Explanation regarding the problem during negative resist removal. Figure (a) represents the non-directional sputtering during gold metal deposition after negative resist development, Figure (b) represents the gold metals sticking to the sidewalls of the negative resist, Figure (c) represents the point of attack of the NMP negative resist remover .....	79
Figure 58: Fabricated platinum and gold strain gauges structured by direct writing lithography and wet etching. Figure (a) represents Pt & Au strain gauges with 10 $\mu\text{m}$ width, Figure (b) represents Pt & Au strain gauges with 20 $\mu\text{m}$ width. ....	80
Figure 59: Fabricated platinum and chromium nested strain gauges. Cracks appear in both 10 $\mu\text{m}$ width (a) and 20 $\mu\text{m}$ width (b) chromium strain gauges. ....	81
Figure 60: Under etch in aluminium strain gauge causes buckling in the adjacent platinum strain gauge. Figure (A) and (B) represent 10 m and 20 m width strain gauges respectively .....	82
Figure 61: Fabricated platinum and titanium strain gauges with 10 m (a) and 20 m (b) strain gauge width .....	83

Figure 62: Relative changes in electrical resistance due to changes in temperature for Titanium strain gauge .....	84
Figure 63: Relative changes in electrical resistance due to changes in temperature affecting the sensor (Rref is set to be the electrical resistance at 24.47°C) .....	84
Figure 64: Relative changes in electrical resistance due to changes in temperature affecting the sensor (Rref is set to be the electrical resistance at 24.47°C). .....	86
Figure 65: Relative change in resistance with respect to strain for 10 µm width Pt and Ti strain gauges .....	87
Figure 66: Relative change in resistance with respect to strain for 20 µm width Pt and Ti strain gauges .....	87
Figure 67: Relative change in resistance with respect to strain for 20 µm width Pt and Au strain gauges .....	88
Figure 68: Relative change in resistance with respect to strain for 10 µm width Pt and Au strain gauges .....	88
Figure 69: Strain of the test specimen containing sensors with Pt & Ti with respect to time.....	89
Figure 70: Strain of the test specimen containing sensors with Pt & Au with respect to time .....	90
Figure 71: Relative changes in resistivity during gasket ageing for 20µm width Au strain gauge in Pt & Au 20µm width nested strain gauges. ....	90
Figure 72: Relative changes in resistivity during gasket ageing for 20µm width Pt strain gauge in Pt & Au 20µm width nested strain gauges. ....	91
Figure 73: Relative changes in resistivity during gasket ageing for 10µm width Ti strain gauge in Pt & Ti 10µm width nested strain gauges.....	91
Figure 74: Calculated strain and temperature affecting the gasket during condition monitoring .....	94



## List of Tables

Table 1: Gauge factor of various metallic alloys. [50][52] .....	52
Table 2: Gauge factor of semiconductor strain gauges [52] .....	53
Table 3: Sputtering power and time of different metals with different film thicknesses .....	58
Table 4: Positive photoresist deposition program .....	59
Table 5: Parameters of platinum layer activation by argon plasma .....	60
Table 6: Platinum etchant composition, duration of etching, and etching temperature .....	60
Table 7: Metals used as the second strain gauge and its respective etchants .....	62
Table 8: Copper etchant composition, duration, and etching temperature .....	64
Table 9: Negative photoresist spin coater program .....	64
Table 10: ICP parameters used for dry etching of polyimide .....	68
Table 11: TCR value of various strain gauges calculated by linear regression until 150.31°C .....	85
Table 12: TCR value of various strain gauges calculated by linear regression until 110.25°C .....	86
Table 13: Gauge factor value of various strain gauges calculated by linear regression .....	88

# CHAPTER 1

## Introduction

### 1.1. Motivation

Gasket is a mechanical seal that fills the space and acts as an interface between two or more coupled surfaces. Gaskets are mainly used in most static and dynamic technical systems and usually utilized as a sealant to prevent leakage coming in and out the two joined objects during operation, therefore their role in safety and increasing systems efficiency is significant.

In terms of safety, gasket can seal off hazardous chemical or unwanted substances from one object to the other. One of the famous examples of gasket failure in terms of safety is the space shuttle Challenger explosion in 1986. In this case, the O-ring gasket failed to contain and prevent hot gases from leaking through the joint between the two lower segments of the right Solid Rocket Motor during the propellant burn of the rocket motor which eventually exploded the external tank. During the day of the launch the ambient temperature of the surroundings was 36°F or 2,22°C, this cold ambient temperature causes the O-ring gasket to harden which results in the decrease of its resiliency, i.e. reducing its ability to return to its original shape [1]. In terms of increasing systems efficiency, in the example of a pneumatic or hydraulic system, gasket could prevent leakage of air needed to build up pressure in order to operate the pneumatic and hydraulic systems.

Gaskets can be fabricated from various materials, ranging from metal to non-metal substance. Non-metal gasket, such as polymer, has an advantage compared to its metal counterpart due to its higher resiliency to chemical processes such as oxidation. There are three stages that needed to be examined when utilizing gasket in a system. Those stages are gasket installation, gasket application, and gasket ageing.

Basically, in order for gasket to function properly as a sealant, gasket need to be deformed in such a way therefore the gasket is squeezed evenly and tightly enough between the two mating surfaces. If this condition is not met, leakage may occur. Mistakes during installation such as choosing the wrong dimensional configuration of the gasket, corroded or uneven mating surfaces which will create leak paths, inadequate or excessive gasket squeeze by the fasteners holding the mating surfaces will induce a leak therefore failing the gasket function as a sealant [2].

After successful installation of the gasket, failure may still occur during the application of the gasket. Failure might be caused by excessive forces applied to gasket which will induce microcracks or even structural breakage altogether, applying fluctuating load to the polymer which will initiate micro-cracks and propagate at relatively low stress level eventually leading to structure fracture [3][4], low temperature of its surroundings which will hinder its elasticity when using a polymer gasket [5], and wrong material selection of the gasket which will be damaged by the liquid being sealed [6].

Even though all previous stages have been done correctly, it is also important to consider the ageing or deterioration of the gasket. Polymer materials when used as a gasket

will be heavily deteriorated by ageing processes from its surroundings, especially at elevated temperatures. This deterioration may produce harmful by-products which could cause health and safety issues while also harming the environment [6]. Polymer deterioration may come from physical ageing without chemical reaction, chemical changes during curing of a thermoset polymer, thermal conditioning at high temperature and photochemical ageing [7].

During its application, polymer gasket deterioration could be accelerated by the presence of elevated temperature on the environment affecting the gasket. Thermal degradation of a polymer will **permanently change its chemical and physical properties**. Both changes are caused by the chemical processes involved during thermal degradation. These processes may affect the chemical composition of the polymer such as the generation of macroradicals, changes in end-group population, and formation of peroxides and carbonyl species. In addition, it also affects its physical parameter such as chain conformation, molecular weight, molecular weight distribution, crystallinity, chain flexibility, cross-linking, branching, and also its physical processes such as the polymer glass transition ( $T_g$ ), melting, sublimation, evaporation, crystallization, cross-linking, charring, and water absorption may take place as a function of time and temperature [8][9][10]. All those changes will inevitably change the macro structure of the polymer itself in terms of its ductility, mass, shape and structural damages such as cracks and voids.

As the deterioration continues, polymer gasket may **change its response whenever it is being subjected to external forces from elastic to viscoelastic**. This change in behaviour will **hinder its ability as a sealant due to the presence of a slow or retarded response to full recovery after an immediate partial elastic response whenever it is being compressed by external forces**. The result of this phenomena is the **polymer gasket fails to return to its original dimensions after a short period of time**. Failure of the polymer to return to its original shape leads to leakage of the system where the polymer gasket is utilized as a sealant [11]. This deterioration can be qualitatively assessed by its **compression set**, where the amount of compression that is not fully recovered at a short period of time is known as set.

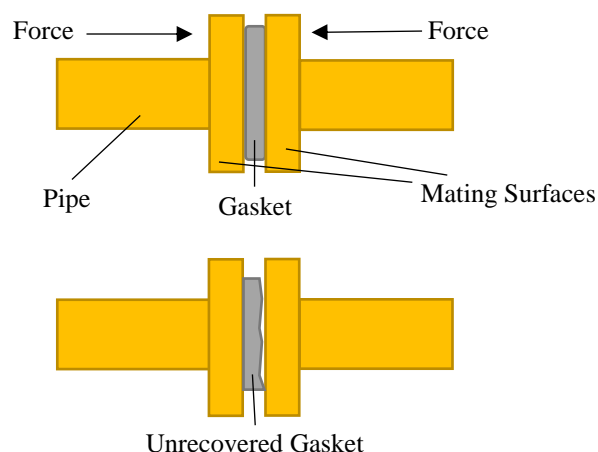


Figure 1: Leaks caused by unrecovered gasket

Until now prevention regarding these issues is only done in terms of passive prevention to the possible failure of the gasket, i.e. no direct monitoring of the condition of the gasket. Prevention regarding gasket failure is only conducted in terms of changing the gasket in a scheduled fashion. Although this may seem as a viable option in terms of tackling this issue, scheduled gasket replacement does not entirely avoid the possibility of the utilization of faulty gasket in a system, i.e. faulty gasket is still being used and not replaced because it is not its schedule. Even worse it could lead to unnecessary expense due to the replacement of fully functional gasket and it is only being replaced due to its schedule.

## 1.2. Proposed approach and method

This master thesis presents a new approach in terms of avoiding the utilization of a faulty gasket in a system by conducting a direct monitoring regarding the strain and temperature affecting the gasket. Knowing these values could eventually help determine the condition of gasket during its application. This new approach will hopefully eliminate the unnecessary expenses on gasket maintenance and increasing the safety in systems where these gaskets are used.

The proposed method in order to achieve simultaneous measurement of strain and temperature influencing the gasket is by integrating the gasket with sensor in form of two strain gauge sensors in a nested configuration which is sensitive to strain and temperature affecting the gasket as shown in Figure 2. The type of gasket used in this master thesis is a polymer O-ring gasket.

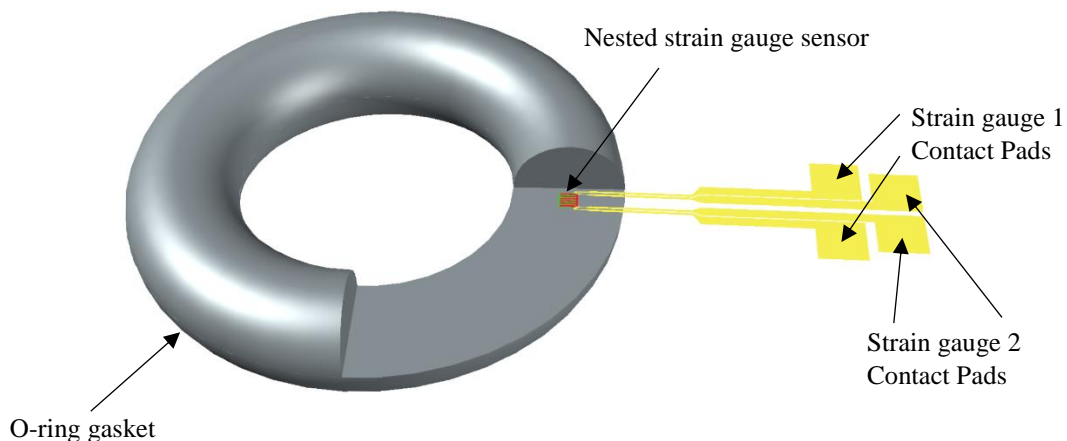


Figure 2: Polymer O-ring Gasket with Integrated Sensor

Nested strain gauge sensor is placed inside the cross section of the gasket. Forces applied to the gasket which eventually compress the gasket and elongate the gasket radially followed by the reduction in its height will then be detected by the strain gauges located inside the gasket and will also apply strain to the nested strain gauges. These strains will eventually be detected by the strain gauges in form of resistivity. Strain measurement from strain gauges are typically temperature cross-sensitive, i.e. the resistance readings from the strain gauges will be affected by the surrounding temperature of the strain gauge.

Temperature cross-sensitivity is usually compensated by the addition of a dummy strain gauge which is not influenced by the strain applied to it due to its placement which is transversal to the applied strain in a half-bridge configuration along with the active strain gauge as shown in Figure 2. Therefore, this dummy strain gauge will change its electrical resistivity mostly due to the temperature affecting it. Changes in electrical resistivity due to temperature affecting the active strain gauge will then be compensated by the changes in electrical resistivity affecting the dummy strain gauge. However, half-bridge configuration of the strain gauges will consume a large place in the sensor. Moreover, there is also the issue regarding the spatial distribution of the temperature affecting the dummy and active strain gauge, i.e. the temperature affecting the active strain gauge may not be in the same value as the temperature affecting the dummy strain gauge.

Nested strain gauge configuration eliminates this temperature cross-sensitivity while also consume less space in the sensor as shown in Figure 3. Nested configuration of these strain gauges not only compensate the temperature for a more accurate measurement of the strain, it also enables the possibility to measure the temperature affecting the gasket as shown in the work of Gräbner, 2018 [12]. The nested strain gauges are made from two different metals each with different thermal coefficient of resistance (TCR) and different gauge factor (GF). A nested form of the sensor has the benefit to minimize the spatial distribution of the strain and temperature applied. Therefore, making the two strain gauges to be active to the applied strains.

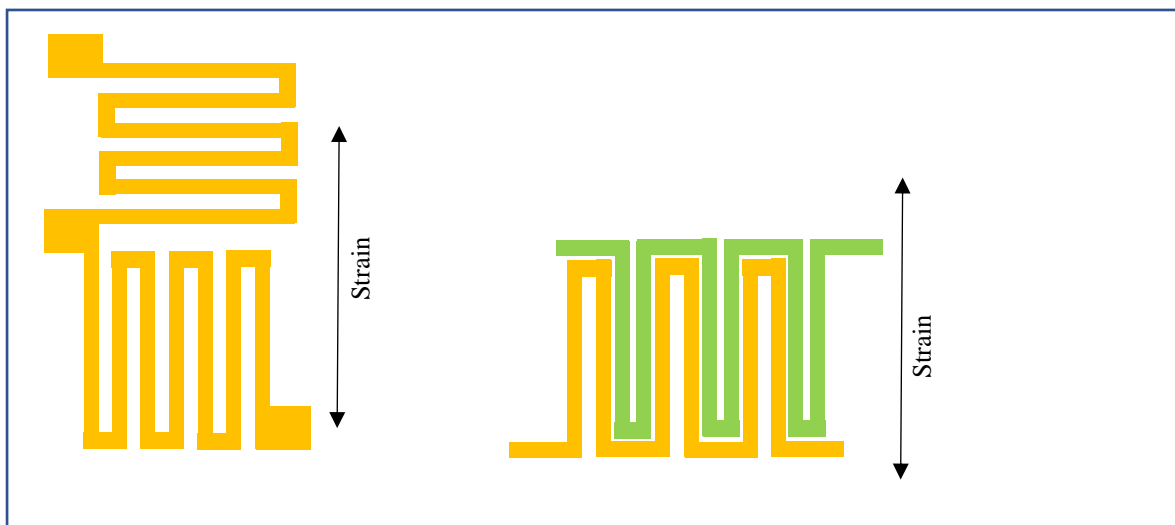


Figure 3: Half-Bridge Configuration (left) and Nested Configuration (right)

Contact pads and conducting path are made from different metals such as those used in the nested strain gauges and is designed to have lower resistivity compared to the strain gauges in order to not disturb the measured resistance data coming out from the nested strain gauges. This is achieved by fabricating the contact pads and conducting path 5 times thicker than the nested strain gauge. The contact pads are placed sticking out of the gasket in order to be able to communicate with the measured data acquisition from the computer.

### 1.3. Existing work and scientific literature

#### 1.3.1. Process Signature

During the application of a gasket such as a sealant, gasket may endure undesired mechanical, thermal, chemical and other environmental factors affecting it. These machining processes revolve around the activity to make alteration to the workpiece in terms of its physical structure or chemical composition. Various machining activity which involves mechanical, thermal, and chemical processes may be different in nature, however they all involve the process of transfer and receiving energy between the machine or surroundings and the workpiece. Therefore, alterations done on the workpiece can be traced back to the amount of converted and dissipated energy affecting it [13].

The term *Process Signature* coined by Brinksmeier and colleagues at their keynote paper [13] suggest the possibility to predict the surface and subsurface properties of a workpiece from its known parameter and the machining parameters done towards it. Therefore, there is a possibility to perform an energy-based approach, rather than describing the nature or source of each various machining process involved, to describe the interaction of machining processes with a workpiece material.

The benefits of perfectly describing the interaction between the machining processes involved and the workpiece material could lead to the ability to perform a specific machining processes in order to obtain a functional workpiece with desirable properties. Process signature thus also contribute to elevate the knowledge regarding the description of the interaction between the machining processes involved and the workpiece material by extending or replaced the ordinary description of manufacturing processes, such as process parameters and material removal rates, with fundamental physical and chemical relationship, i.e. the energy involved during the process, as described in figure 4. The energy involved is also correlated to the interaction time between the material and the processes done towards it. The interaction time will inevitably determine the exposure time of energy conversion and dissipation.

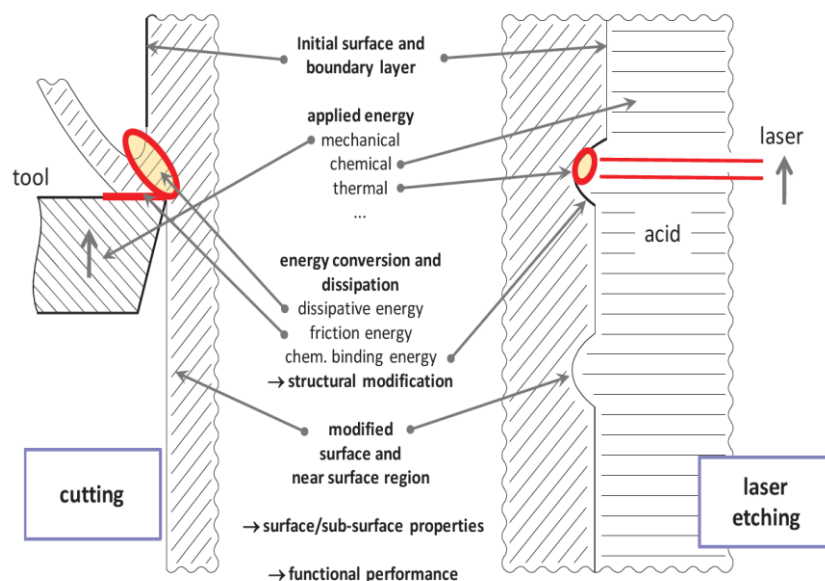


Figure 4: Different machining process described by the energies involved [13].

In terms of knowing the condition of a gasket, process signature could help predict and determine the cause of deterioration or ageing of the gasket during its service lifetime. During the gasket installation on a specific system one could look at the surrounding of the gasket, which include the conditions of the environment and other parts of the machinery affecting the gasket, and assess the type of energies being converted and dissipated in the process. Naturally, besides the type, the exposure time of these energy is also of importance. As mention earlier, determining the exposure time of these energies can be correlated with the interaction time between the gasket and its surroundings. Knowing the exposure time will eventually contribute to determine the energy flow during the process and if the reaction of the gasket material due to this energy flow is known, changes in the functional performance of the gasket can be determined, i.e. determining and predicting the deterioration or ageing of the gasket could be performed.

Conducting condition monitoring of the gasket could help in knowing the energy received by the gasket during its implementation, at least in this master thesis to some extent in terms of the mechanical and thermal energies received by the gasket. By knowing these values, describing the interaction between the gasket and its surroundings regarding the mechanical and thermal energy involved could be achieved. Therefore, it will also help to achieve the goal of process signature which is to determine and predict the deterioration or ageing of gasket by referring to the alteration of the functional performance of the gasket due to the changes in the surface and subsurface properties of the gasket.

### **1.3.2. Structural health monitoring**

Structural health monitoring (SHM) has been the interest of many engineers in the last decades such as in the fields of aerospace and civil engineering [14][15]. SHM revolves around the activity to perform a diagnosis regarding the condition of a constituent material during its lifetime while also providing a prognosis of that material due to the availability of the full history database of the structure and usage monitoring [16]. Performing this activity unlocks the possibility to have a full management of the structure, reduced downtime and maintenance, and structure reconsideration in the future.

Full management of the utilized structure can be shown by the ability to monitor and determine the condition of the structure at any given moment during its operational lifetime. By being able to monitor the condition of the structure, one can make the optimal use of the structure with respect to its surroundings conditions therefore minimalizing the misuse of the said structure which will contribute to the avoidance of catastrophic failure of the whole system. The famous example of accident due to the failure in determining the condition of a structure is the accident of Aloha Airlines Flight 243 in 1988. The maintenance crew failure at determining the presence of significant disbonding and fatigue damage endured by the aircraft during night time maintenance check led to failure of the lap joint and the separation of the fuselage upper lobe [17]. It can be concluded that the absence of knowing the condition of the aircraft structure during its service led to this disaster. This accident can be avoided by means of, for example, implementing an integrated monitoring sensor to the aircraft structure which capable of obtaining the information regarding the health of the structure before, during, and after flight.



As mentioned earlier, implementing a continuous structural health monitoring could lead to the reduction of structure downtime and maintenance. This is because one could eliminate the necessity to perform a scheduled maintenance check of the structure and maintenance should only be performed when there is a damage or deterioration of the monitored structure. Therefore, a transition from a scheduled-based maintenance check to condition-based maintenance check could be achieved [18]. The benefits of this transition can be seen in terms of economic and safety assurance point of view. In economic point of view, one can reduce the frequency to perform maintenance check therefore reducing the cost involved in each maintenance check. Since less maintenance check is performed, thus the downtime of the monitored structure could also be reduced therefore the service lifetime of the structure is extended. Also, it is more economically efficient as well in terms of parts replacement, since the condition of the structure is known, therefore the possibility to replace fully functioning parts with a new one is reduced. In safety assurance point of view, the safety assurance of the utilized structure could be increased due to the fact that the possibility of using a faulty or deteriorated structure could be minimised since every maintenance is done only when there is a damaged or deteriorated structure.

Other benefit of performing structural health monitoring is the ability for the manufacturer to reconsider the development of the already made structure. Due to the presence of structural health monitoring, the manufacturer could receive the performance data gathered from the structure during its operational lifetime. Eventually this data could be the basis for the manufacturer to make adjustments and further development of the structure in the future.

In the implementation of structural health monitoring it is also important to note that the monitoring of the structure is done in a non-destructive manner and provide a reliable, repeatable, and if possible, a linear response to the parameters being measured [19][20]. A non-destructive monitoring ensures that there will be no deterioration of the structure caused by the integration of the sensing element to the host structure, i.e. deterioration only come from the structure surroundings during its operational lifetime. A non-destructive monitoring could be achieved by implementing the sensing element in a non-disruptive way. This could be achieved for example when embedding the sensing element inside the structure is preferred, the sensing element should have the same material properties as the host structure therefore bond between them is achieved and the sensing element should be in a diminutive scale therefore it would not give a relatively high load to the host structure when forces are applied to the host.

### **1.3.3. Sensor Integration**

Sensor integration has been one of the emerging topics of engineering in the last few years. It enables a material or structure to be aware of its condition caused by the environmental condition around it, forces acting on it, energies transferred or dissipated, etc. The ability of a structure or material to perform these actions is what the term “smart” attached to many equipment and appliances in the market nowadays. The awareness of the material and structure comes from the sensors embedded into it which provides useful data to the user which could dictate the behaviour of the material during its operational lifetime, unlocking the possibility for research and development for the next generation of the materials and structures. Therefore,



because of this reason, sensor integration could be one of the practical realizations of performing a Structural Health Monitoring to a structure or a material.

In terms of monitoring the condition of a structure, engineers have managed to perform a monitoring of vital locations of damage by imbedding a fiber Bragg grating (FBG) sensors inside an aerospace fiber reinforced polymer [14]. Mechanical factors subjected to an aircraft during its operation such as impact, vibration and loading could damage the fiber reinforced polymer structure. These damages, such as delamination and matrix cracking in addition to internal material damage, could be invisible to the naked eye. Because of this reason conventional damage and structural integrity evaluation may not be sufficient, as proven by the example of the Aloha Airline flight 243 accident in 1988 [17]. FBG sensors could be used to detect stress gradients along its length and determine the stress variations in the host material by the presence of a chirp in the reflected spectra of the FBG sensor [21][22]. Similar to most embedded sensor, FBG sensors is integrated into the FRP composite during the manufacturing of the composite part. Since the scale of the sensor is diminutive, it has no effect on the strength of the host structure. FBG sensor is made up of glass, therefore it is environmentally more stable and having a long lifetime similar to its FRP composite host material.

Another example of performing SHM to a structure is presented in the work of Schotzko and Lang [19]. In this example, they perform a condition monitoring of a gasket by means of embedding a strain gauge sensor inside the gasket which could detect the strain endured by the gasket during its operational lifetime. The strain, which correlate to the thickness of the gasket, will determine its sealing capability when the gasket is used as a sealant in a system.

Although in some cases, sensor integration could also be used to monitor not the structure or the material itself, but the user of that structure. This is the case of most research regarding wearable sensor today. Most of these researches involve embedding sensor inside a textile structure (suit) which is then wore by the user such as in the work presented by Catrysse, et.al. [23]. In their research, the suit is used to monitor the electrocardiogram and respiration rate of children in a hospital environment. Other electronics beside the sensors is also embedded in this suit, such as interface, data handling, storage, and transmission electronics which makes it possible to store and transmit data wirelessly to a remote observer.

Of course, several difficulties are present in embedding sensor inside a foreign host structure and those difficulties will differ in each host material used. In the case of embedding sensor in a rigid host structure such as in metals, the flexibility of the sensor to deform together with the host structure may not be as much of a problem as the problem of ensuring the sensor functionality at high temperature during metal casting or shaping of the metallic structure. On the other hand, when embedding a sensor in a flexible host structure such as polymers or textile, delamination or breakage of the sensor from the host material due to the inability of the sensor to deform in a wide range of strain could be the main reason of measurement failure.

#### **1.3.4. Leakage detection method**

Gaskets are mainly used to act as a sealant between two mating surfaces. The condition of a gasket will determine its effectiveness in sealing the fluid inside it. Effectiveness of the

sealing capability is determined by the pressure given by the gasket to the mating surfaces due to the elastic behaviour of the gasket which return the gasket into its normal shape. Nowadays, in most largescale systems, such as those in industrial systems, leakage detections are done indirectly by means of applying pressure and flow sensors at various places inside the system [24]. Leaks are detected through drop in pressure and the reduction in the flow rate but only at the location of the sensing element. Because of this reason, the location of the leaks itself could not be determined.

A research regarding on-line, i.e. measurement during its operation, leakage detection and level estimation has also been conducted [25]. The research used data such as air flow rate and pressure patterns, and with the help from various mathematical tools, changes in those data caused only by leakages are determined. However, this method is only suitable to detect sealing leakage above 0.3 mm.

Another method is also present in measuring possible leakages in a system, specifically caused by the uneven or inadequate pressure deforming the gasket. The study regarding the use of a special tactile pressure sensor film (TPSF) to determine the pressure affecting the gasket with respect to the torque given to the bolts of an air-cooled engines has been conducted [26]. In this paper, the author implements various bolt tightening techniques with various torques in each test and with the help from TPSF in each test, such as Pressurex® from Sensor Products Inc. and Fuji Prescale® film from Fujifilm, they could determine the amount of pressure affecting the gasket in every instalment in each test and determine the correct technique and the amount of torque should be given in each bolt tightening procedures. The measurement is done by placing the TPSF between the gasket and the mating surfaces, then the bolts were tightened with specific amount of torque and technique. Afterwards, the mating surfaces were disassembled and the TPSF is removed. The pressure endured by the TPSF will correlate to the pressure affecting the gasket. The TPSF will shows a change in colour intensity based on the pressure variation affecting it. Therefore, with the help from computer aided evaluation, the analysis of the pressure distribution and magnitude between any two surfaces that come into contact could be evaluated. However, since this measurement technique required the installation and disassembly of the mating surfaces in every evaluation, it is only beneficial in the phase of installation in order to obtain the proper installation technique and does not provide a continuous flow of data whenever the gasket is operational.

Thus, in this thesis the author presents a new technique which could detect the source of the leakage occur at the interface between two surfaces held together by the gasket, which commonly act as the major cause of leakage, by means of monitoring the condition of the gasket during operation which results in its sealing capability. This way, it could measure even the slightest leakage opening due to sensor which measure the deformation occur to the gasket directly.

### **1.3.5. Determining the condition of a gasket by means of strain measurement**

A study has been conducted in terms of conducting a direct measurement regarding the condition of a gasket during its installation [19]. The measurement is done by measuring the strain endured by the gasket as a reaction from external forces affecting it. Through this measurement, one could detect whenever there is a mistake during installation or whenever

there is a significantly large force acting on the gasket which will cause leak and damage to the overall system.

The measurement is done by means of fabricating a thin-film platinum strain gauge sensor which rests on top of polyimide layer and then embedding it inside an O-ring polymer gasket. If the gasket is compressed, the inner and/or the outer diameter of the gasket will increase followed by the reduction in the thickness or height of the gasket. The embedded strain gauge will be strained along with the polymer gasket therefore producing a readable electric signal in form of electrical resistivity.

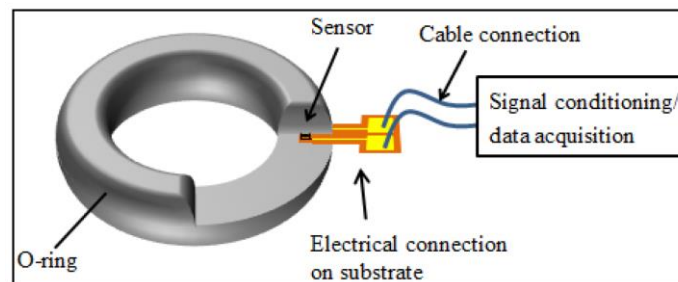


Figure 5: Sensor integration inside polymer gasket for strain measurement [19].

The data from the study shows that there is linear relationship between the force applied to the gasket, i.e. the force which induces strains on the gasket, with the electrical resistance readings of the embedded strain gauge. A hysteresis in the measurement is observed during the loading and unloading of the strain gauge. Hysteresis is caused by the cold hardening done to the metals of the strain gauge, adhesion properties to the substrate material, or the host material of the strain gauge foil causes hysteresis as well as the zero offset [19]. However, the area of hysteresis will diminish as more and more strain cycle, i.e. the loading and unloading cycle, is applied to the strain gauge, suggesting that a prolonged strain gauge usage will produce a more linear and accurate readings as more strain cycle is applied.

Utilizing the method of strain measurement from this study is also a great way to measure the functional capabilities of a gasket, for example as a sealant, during its application. As mentioned previously, one method to determine the condition of a gasket in terms of its sealing capabilities is by measuring its compression set. Compression set give an insight regarding the condition of an elastic structure and its ability to return to its original shape by measuring the height of a structure after a compression is applied. By unlocking the ability to measure the strain of a gasket in a real time, one could measure its compression set, therefore knowing its condition and functional capabilities.

### 1.3.6. Simultaneous measurement of strain and temperature with two resistive strain gauges

A further study has also been conducted in terms of increasing the capability of performing a Structural Health Monitoring by means of conducting a simultaneous measurement of strain and temperature [12]. Measurement is done by utilizing two resistive strain gauges made from different material therefore having different Gauge Factors (GF) and

Thermal Coefficient of Resistance (TCR). These strain gauges are placed close to each other in form of a nested shape. This study acts as a basis for the fabrication of the sensor used in this master thesis. However, in this master thesis the materials used as the strain gauge is different and the functional capabilities of this sensor in order to monitor the condition of a polymer gasket by embedding the sensor inside it is explained.

Materials will produce a change in electrical resistivity whenever they are strained and the amount of the electrical resistivity change with respect to the amount of strain it endures is dictated by the Gauge Factor. Regarding temperature, conductors will also change its electrical resistivity as the temperature affecting it changes. The rate of this electrical resistivity change with respect to temperature is dictated by the conductor's thermal coefficient of resistance.

Both strain gauges will have their electrical resistivity changed by the strain applied to them and by the temperature affecting them. By means of utilizing two strain gauge sensors both made from different metals with different gauge factor and thermal coefficient of resistance value unlocks the ability to determine the amount of strain and temperature which cause those electrical resistivity changes. This determination is done by mathematical formula involving the gauge factor and thermal coefficient of resistance of both materials in the nested strain gauge.

The metals used as the strain gauges in this study consist of platinum as the first strain gauge and titanium as the second strain gauge. During experimentation, these metals are first tested in order to obtain the gauge factor and the thermal coefficient of resistance of each metal by means of applying strain in a three-point bending test setup and heating it with hotplate respectively. After the values are known then a combined strain and temperature measurement test is conducted and it is observed that a change in electrical resistivity is significantly present for platinum strain gauge however it is not too apparent for the titanium strain gauge. This is mainly caused by the low gauge factor of the titanium metal. Therefore, in this master thesis, different metal combinations are studied in order to fully enhance the performance of this method.

# CHAPTER 2

## Theoretical Background

As mentioned previously in Chapter 1, gaskets in most technical systems are mainly used to connect two mating surfaces and perform a seal between them. During installation, the gasket is deformed in order to fit and properly connect the two surfaces, it is typically done by tightening the bolts between the two surfaces. Since stress is introduced in the gasket and the deformation of the gasket occurred, there will be an elastic restoring force exerted by the gasket towards the mating surface in order to make the gasket returns to its original shape. These elastic restoring forces will eventually induce pressure towards the mating surfaces, e.g. flanges.

A spatially uniform pressure applied to the gasket ensure that the gasket surface has uniformly deform to perfectly sealed and enveloped the mating surfaces [26]. Since a uniform deformation of the gasket occur, as a result, a uniform pressure the gasket exerted towards the mating surfaces also present, therefore minimizing the possibility of leakage. However, as the gasket decays due to ageing, the gasket could become brittle or soft depending on the ageing mechanism involved. These effects will hinder the sealing capability of the gasket caused by the reduction of the pressure the gasket gives to the mating surfaces.

### 2.1. Compression Set (CS)

The pressure exerted by the gasket is correlated to the elastic behaviour the gasket has in response to an external force. Elastic properties of the gasket will force the gasket to return to its original shape. However, since its movement is limited between the flanges these forces will be translated to pressure affecting the mating surfaces. One method to determine the elastic properties of a material is by measuring its *compression set* (CS) [27][28].

Compression set could be regarded as the permanent plastic deformation of a material after it is being compressed at specific temperature and for a specified duration. Therefore, elastic properties of the material could be assessed by the amount of irreversible deformation it endures after being subjected to an external force. There exist several ways in determining the compression set of a material. The most prominent ones are the compression set measurement standard proposed by DIN ISO 815 [28] and ASTM D 395 [27].

In the standard proposed by ISO 815 and ASTM D 395 method B, test specimen is placed in a compression plate along with spacers on each of its sides, as shown in Figure 6. The difference between the two is the amount of compression affecting the test specimen. In the case of ASTM D 395 standard, the compression at constant strain applied is fixed at approximately 25% [27], whereas in ISO 815 standard, the compression applied ranges from 25% to 10% and it is based on the hardness of the rubber within the range 10 IRHD to 95 IRHD

[28]. Following both of these methods, the compression set of the test specimen is described as:

$$CS [\%] = \frac{h_0 - h_2}{h_0 - h_1} \times 100 \quad (1)$$

where  $h_0$  represent the original height of the gasket,  $h_1$  represent the height of the gasket while it is being compressed, and  $h_2$  represent the height of the gasket after compression is removed.

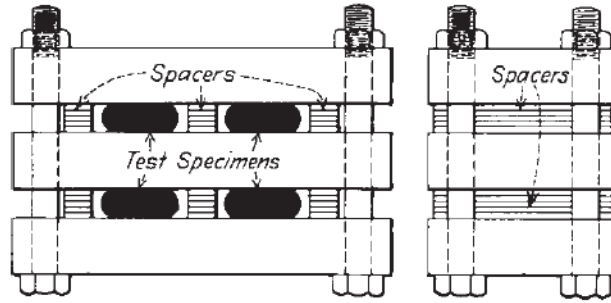


Figure 6: Compression set measurement setup using ISO 815 [28] or ASTM D 395 Method B standard [27]

Other method which is completely different from previous method is proposed by ASTM D 395 method A. In this method, rather than a known deformation applied to the test specimen, a known force is used to conduct the deformation on to the test specimen as shown in Figure 7. A force of 1.8 kN is applied by the compression device to the test specimen [27]. The compression set is determined as the percentage of the original thickness, as described in the following equation where  $h_{initial}$  and  $h_{final}$  represent the height of the gasket before and after compression respectively.

$$CS [\%] = \frac{h_{initial} - h_{final}}{h_{initial}} \times 100 \quad (2)$$

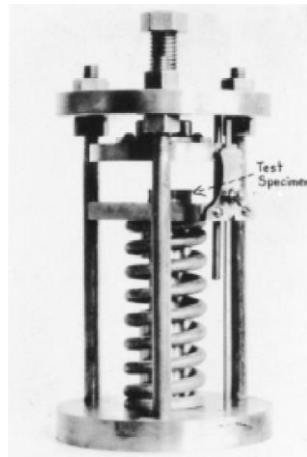


Figure 7: Compression set test device for ASTM D 395 Method A standard using calibrated spring as the known load force [27].

However, as the utilization of the gasket continues, polymer gasket will deteriorate over time. This deterioration will be represented by the appearance of a viscoelastic behaviour of the polymer gasket which is observed by the slow or retarded response of the polymer gasket



to return to its original shape. Thus, the viscoelastic behaviour of the polymer gasket caused by the deterioration of the gasket will increase the amount of the compression set produced by the gasket.

## **2.1 Polymer Ageing**

Polymer gasket is one of the easiest and most cost effective gasket that could be fabricated. It involves extruding a polymer, such as silicone for instance, in its liquid state into a mould with the desired form and let it cools down into its solid form. However, as good as it may seem, most structures made of polymers will over a period of time prone to a deterioration process termed “Ageing”.

Ageing is a term used in polymer science whenever there is a change in its properties over a period of time. Events that occur on molecular level will lead to changes in the morphology and macroscopic physical properties of the polymer. These changes maybe in form of its physical properties such as its density or chemical characteristics such as its reactivity towards certain chemicals. Overall these changes will inevitably change the macroscopic behaviour of the whole structure such as its strength and ductility. The changes occurred during the ageing of polymer may result in the inability of that specific polymer structure to do its function properly in its application.

As an example, in the case of polymer gasket, it was previously stated in chapter 1 that a gasket requires a small amount of deformation in order to completely coupled two mating surfaces and forms a seal between them. However, because of the ageing of polymer, this deformation may not be sustained indefinitely due to alteration in the behaviour of the polymer from elastic to viscoelastic as the ageing of the polymer gasket continues. The viscoelastic behaviour of the polymer gasket makes it lack the required back stress in order to successfully coupled and sealed the two conjoining surfaces. The detection of these viscoelastic behaviour will then be conducted by the strain gauge sensors inside the gasket to give an overall idea regarding the condition of the gasket.

Origin of these ageing may involve physical ageing without chemical reaction, chemical changes during curing of a thermoset, thermal conditioning at elevated temperature, and photochemical ageing during weathering of the polymer structure [7]. However, in this master thesis the material being subjected to experiment is a thermoplastic silicone polymer and the experiment involve the measurement of strain and temperature conducted by the strain gauges. Therefore, polymer gasket deterioration involving physical ageing and thermal conditioning at elevated temperature will be discussed in the following sections.

### **2.1.1. Physical Ageing of Polymers**

In a journal published by Simon [29] in 1931, he showed that amorphous solids are not in thermodynamic equilibrium at temperatures below their glass transition. He suggests that those materials are to be regarded as solidified supercooled liquids who has volume, enthalpy, and

entropy higher than they would be in equilibrium state. This phenomenon is commonly occurred in thermoplastic moulding whenever it is being cooled rapidly from elevated temperature, such as when the polymer is left alone after extrusion. Naturally, since the moulding is left alone to cool down, it will reach thermal equilibrium with its surroundings. However, following the statement mentioned previously, thermal equilibrium may not necessarily be their thermodynamic equilibrium. Therefore, since it is not their equilibrium, there exists some “force” to drive the material to reach equilibrium even when it is below their glass transition temperature ( $T_g$ ). These “force” will be referred as *molecular driving forces* [30] or in terms of polymer structure it can be represented as *segmental mobility* (M) [31] of the polymeric chain. The approach to equilibrium will in turn affects many properties of the material over time, therefore it can be said that the material is undergoing physical ageing process.

Understanding the process behind physical ageing requires a concept known as *the free volume concept* as explained in the work of Struik [31]. In his work he stated that transport mobility of particles or the segmental mobility (M) in closely packed system primarily depends on the degree of packing, i.e. the free volume ( $V_f$ ) as shown in Figure 8. It can be observed that an increase in degree of packing will decrease the mobility. At elevated temperature, typically above  $T_g$  polymer will behaves as a rubber or fluid where small stress will induce large strain which inherently represent large segmental mobility, i.e. large free volume ( $V_f$ ).

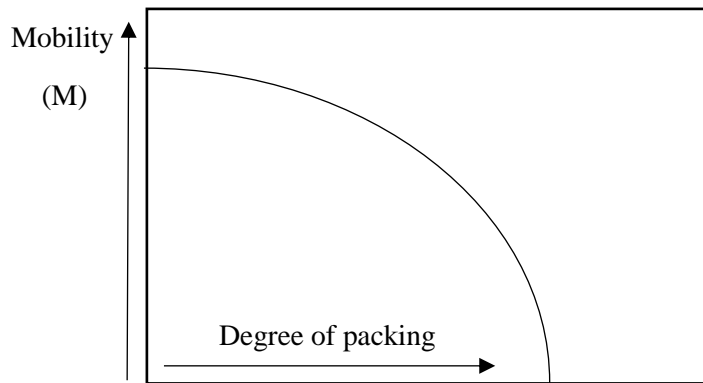


Figure 8: The free volume concept [31].

Before we consider the importance of free volume, let us recall the Gibbs free energy equation and its correlation with thermodynamic equilibrium. Gibbs free energy is a thermodynamic potential that can be used to calculate the maximum of reversible work that may be performed by a thermodynamic system at a constant temperature and pressure. Thermodynamic equilibrium is reached whenever a system has the Gibbs free energy of its lowest value. Gibbs free energy equation can be described as Equation 2 where  $G$  is the Gibbs free energy of the whole system,  $U$  is the internal energy of the system,  $P$  represent the pressure,  $V$  represent the volume,  $T$  represent the temperature, and  $S$  represent the entropy of the system.

$$G = U + PV - TS \quad (2)$$



At elevated temperatures, i.e. at higher  $T$ , the importance of entropy  $S$  will be increased in order to balance the increasing value of  $U$  due to higher kinetics of the molecules at higher temperature and produce the lowest possible value for  $G$ . One way to increase the entropy  $S$  of a system could be done by increasing the free volume ( $V_f$ ) of the system which caused by the increase in the segmental mobility of the polymeric chains. In the case of cooling down the polymer until it reached below its  $T_g$ , the importance of the entropy  $S$  in order to lower the Gibbs free energy value will be decreased due to the low temperature  $T$  multiplier. Since free volume is made up of holes and since molecules attract one another, the existence of free volume represents an increase in internal energy of  $U$  with respect to the zero free volume state [31] due to the increase in energy required to break the bonds between molecules. Therefore, there will be a decrease in the free volume ( $V_f$ ) of the system due to the decrease in the importance of entropy  $S$  and coping with the changes in the internal energy  $U$  to produce the smallest value. The relation between temperature, free volume ( $V_f$ ) and segmental mobility ( $M$ ) could be represented in Figure 9.

However, as can be seen from Figure 7 the changes in free volume required (represented by the dashed line) in order to reach thermodynamic equilibrium could not be achieved. Free volume ( $V_f$ ) cannot decrease indefinitely in order to reach thermodynamic equilibrium. The reason of this is because redistribution of the holes ( $dV_f/dt$ ) is determined by the segmental mobility ( $M$ ) of the polymeric chains and referring to Figure 8, segmental mobility ( $M$ ) is affected by the free volume ( $V_f$ ). Thus, a closed loop scheme is formed between segmental mobility ( $M$ ), free volume ( $V_f$ ), and holes redistribution ( $dV_f/dt$ ) as shown in Equation 3 [31].

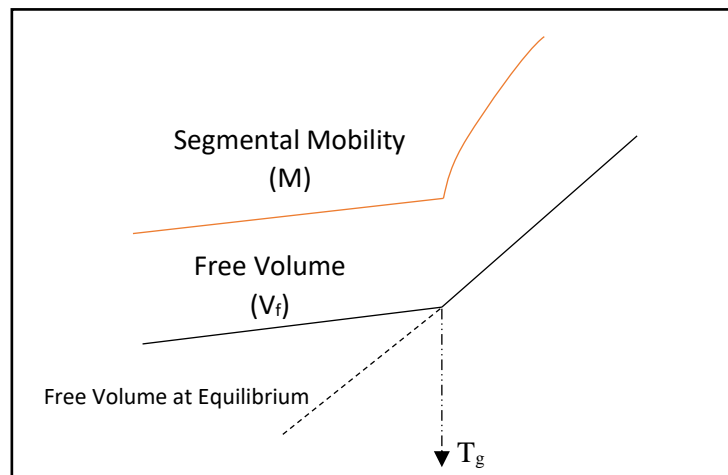


Figure 9: Relation between Segmental Mobility, Free Volume, and Temperature. [31]

$$V_f \Rightarrow M \Rightarrow \frac{dV_f}{dt} \quad (3)$$


Below certain temperature, typically below its  $T_g$ , segmental mobility ( $M$ ) will be so small, i.e. does not change rapidly as it does above  $T_g$ , to accommodate the decrease in  $V_f$  to balance the changes in the internal energy ( $\Delta U$ ) and entropy ( $\Delta S$ ). This is mainly due to less free volume available as the material cools down below  $T_g$  as can be seen from Figure 9. However, as a consequence of Equation 3, decrease in  $M$  requires a decrease in  $V_f$ . Therefore, mobility still exists even in a slow rate at temperatures below  $T_g$  in order to reduce the  $V_f$  until it reaches its equilibrium. This is mainly because even though mobility is affected by the availability of space, i.e. its free volume, it is still thermally activated [32]. Therefore, free volume will decrease slowly and accompanied by the decrease in  $M$ .

The resulting effect of these decrease in free volume is that the density of the polymer will increase over time as long as the physical aging of the polymer continues. However, the density of the polymer will differ between its core and its skin as shown in Figure 10. One of the reasons of this density difference is due to the rapid cooling done in the thermoplastic moulding and the low thermal conductivity of the polymer which provoke a formation in residual stresses between the interior, i.e. its core, of the polymer structure and its near surface layer, i.e. its skin [7].

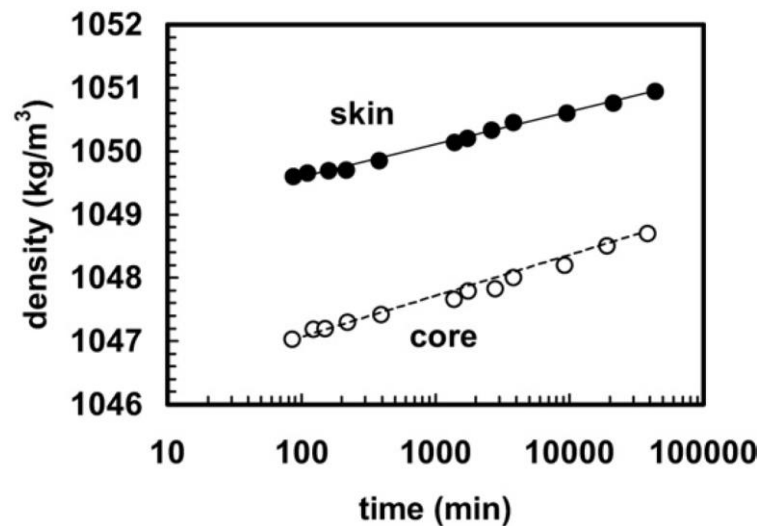


Figure 10: Density difference between core and skin of a moulded polystyrene bar at 23°C ageing temperature. [7]

During the cooling of the thermoplastic polymer, the near surface layer easily dissipates the heat it contains toward the surroundings therefore reducing its free volume faster compared to the interior of the polymer structure. Since the interior is still relatively hotter than the near surface layer, therefore the segmental mobility of the polymeric chains in the interior is higher than those of the near surface layer. Higher segmental mobility indicates larger available free volume. This difference will result in the tensile stresses at the interior of the polymer structure and compressive stresses at the near surface layer. Both of these stresses caused by strong temperature gradients formed a residual stress contained within the structure [33].

Residual stresses could relax partially or completely depending on the  $T_g$  in case of amorphous polymers and crystallinity in case of semi-crystalline polymers [7]. These relaxation leads to the change in residual stresses contained within the structure and will appear

as an ageing phenomenon. Residual stresses will relax quite rapid at the beginning of the ageing time and slows down progressively until finally reached the significant fraction of the original values after moulding. Elevated temperature will affect the rate of residual stresses relaxation while also change the final equilibrium state itself [7]. The increase kinetics and mobility of the polymeric chains during ageing at elevated temperature will ease the residual stresses relaxation process as shown in Figure 11.

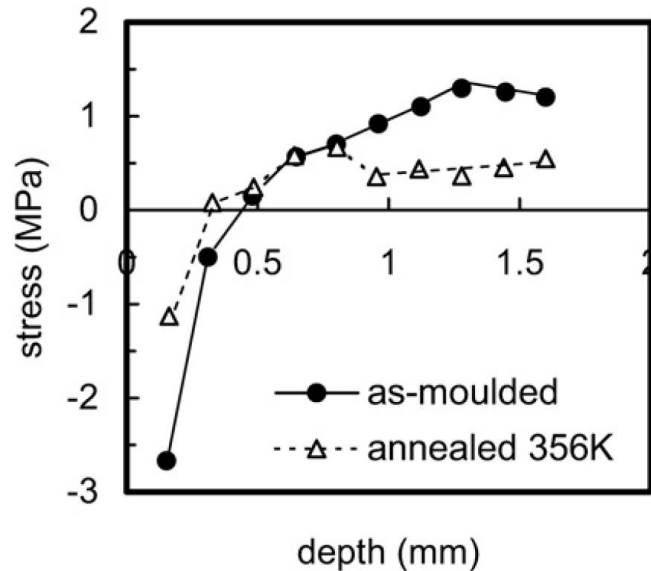


Figure 11: Residual stress distribution of polystyrene bar in 1.5 mm thickness in the as moulded state and the annealed state. [7]

Although the density of the polymer structure will differ between its core and the near surface layer, the density growth rate of these two locations will be quite similar. The rate of densification depends on the departure from equilibrium at the ageing temperature  $T_a$  [7].  $T_a$  is the temperature where it has reached the thermal equilibrium with its surroundings and the polymeric material is left alone to undergoes ageing.

In respect to the  $T_a$  of the material compared to its  $T_g$ , two density growth regimes might be observed. The first regime is when the  $T_a$  is not too far below its  $T_g$ . In this case, the ageing process will be quite rapid initially, however it will slow down as its approach to equilibrium. The second regime is when the  $T_a$  is far below its  $T_g$ . In this regime, the thermodynamic driving force to push the density of the material towards its equilibrium will be large, therefore the system will favour change. However, due to low temperature, the kinetics of the polymeric chains will be lowered, resulting in the limitation of the rate of change [7]. It can be concluded that, both of these changes in densities are driven by the thermodynamic driving force and the kinetics of the polymeric chains.

Thermodynamic driving forces are present in order to push the material into its thermodynamic equilibrium state. Thermodynamic equilibrium is reached when a system is on its thermal equilibrium, mechanical equilibrium, and diffusive equilibrium with its surroundings, and no external driving forces affecting the system are present. In the case of a thermoplastic polymer mould being cooled down in order to have the same temperature with

its surroundings, it can be concluded that it has already reached thermal equilibrium with its surroundings. However, it is also important to note that it is not necessarily at its thermodynamic equilibrium. One of the reasons that it might not be at its thermodynamic equilibrium is due to its displacement from mechanical equilibrium.

In thermodynamics, mechanical equilibrium is reached when there is a uniform pressure affecting both systems, i.e. the system and its surroundings. In the case of our thermoplastic polymer with respect to its surroundings, the volume of the thermoplastic mould after it has been cooled down to reach thermal equilibrium with its surroundings, it may have been cooled down until it reached the temperature which is already far below its  $T_g$ . Referring to the graph on Figure 9, the mobility of the polymeric chains is already falling too steeply when the temperature drops below the  $T_g$ . As already mentioned above in Equation 3, the mobility of the polymeric chains ( $M$ ) affects the rate of change in the free volume of the system  $\left(\frac{dV_f}{dt}\right)$ . Since the system is already situated at a low temperature, the necessity of a high value of entropy is diminished, therefore it drives the system to reduce its free volume. Since the reduction in free volume requires mobility in the polymeric chains and since the polymeric chains mobility could not keep up with the changes required by the free volume in order for it to reach equilibrium, therefore it can be concluded that the system's current volume, which also represents the system density, is still characteristic of a higher temperature. Due to this reason, thermodynamic driving forces are present and act as a motor which drives the physical ageing process of the polymer shown by the changes in its density.

In general, thermodynamic equilibrium could be indicated when the system has reached its highest entropy ( $dS = 0$ ) [30]. In a same manner as it has been described by the Gibbs free energy equation mentioned above (Equation 2), the differential expression for entropy and fundamental energy could be written as the following Equation 4 and Equation 5 respectively [30].

$$dS = \left(\frac{\partial S}{\partial U}\right)_{V,N} dU + \left(\frac{\partial S}{\partial V}\right)_{U,N} dV + \sum_{j=1}^n \left(\frac{\partial S}{\partial N_j}\right)_{U,V,N_{i \neq j}} dN_j \quad (4)$$

$$dU = \left(\frac{\partial U}{\partial S}\right)_{V,N} dS + \left(\frac{\partial U}{\partial V}\right)_{S,N} dV + \sum_{j=1}^n \left(\frac{\partial U}{\partial N_j}\right)_{S,V,N_{i \neq j}} dN_j \quad (5)$$

Where  $S$  represents the entropy,  $V$  represents the volume, and  $N_j$  represents the particle number. Each partial derivative in the fundamental energy Equation 5, corresponds to a measurable physical property. Those physical properties are temperature  $T$ , pressure  $P$ , and chemical potential  $\mu_j$  which is represented in the following Equation 6.

$$T = \left(\frac{\partial U}{\partial S}\right)_{V,N}, \quad P = - \left(\frac{\partial U}{\partial V}\right)_{S,N}, \quad \mu_j = \left(\frac{\partial U}{\partial N_j}\right)_{S,V,N_{i \neq j}}. \quad (6)$$

In the case of our polymer system when it has reached thermal equilibrium with its surroundings, we could assume that there will be no energy exchange ( $dU$ ). Also, since the system is isolated, we could assume that there will also be no change in particles ( $dN_j$ ).

Therefore, with respect to Equation 4, the only changes it would have undergoes is the change in its volume ( $dV$ ). Highest entropy ( $dS = 0$ ) therefore could be achieved by the following derivation.

$$dS = \left( \frac{\partial S}{\partial V} \right)_{U,N} dV = 0 \quad (7)$$

Since reduction in the volume of the system ( $dV_B$ ) results in the increase in the volume of the surroundings ( $dV_A$ ), therefore the following constraint is applied.

$$dV_A = -dV_B \quad (8)$$

Since two systems  $dV_A$  and  $dV_B$  are considered in this example, therefore Equation 7 could be written as Equation 9.

$$dS = \left( \frac{\partial S_A}{\partial V_A} \right)_{U,N} dV_A + \left( \frac{\partial S_B}{\partial V_B} \right)_{U,N} dV_B = 0 \quad (9)$$

Substituting the partial derivatives element from Equation 9 and applying the constraint from Equation 8, we would obtain the following Equation 10.

$$dS = \left( \frac{P_A}{T_A} - \frac{P_B}{T_B} \right) dV_A = 0 \quad (10)$$

Therefore, Equation 10 could be satisfied when  $\frac{P_A}{T_A}$  is equal to  $\frac{P_B}{T_B}$ . Because the system has reached thermal equilibrium with its surroundings, therefore  $T_A$  is equal to  $T_B$ . Resulting in the condition that should be met is  $P_A = P_B$ . Due to the fact that the current polymer volume is characteristic to that of a higher volume therefore  $P_A > P_B$ . Thus, the maximum entropy the system could reach in order to reach thermodynamic equilibrium between the system and the surrounding is by the increase in  $V_A$  and the decrease of  $V_B$ , i.e. shrinking of the polymer which results to increase in its density.

### 2.1.2. Thermal Ageing of Polymer at Elevated Temperatures

As already mentioned in the introduction of this master thesis, temperature play a huge role in the degradation process of a polymer. When polymeric materials are affected by heat, major unrecoverable changes in physical and chemical properties might present. These changes might be in form of changes in its molecular weight and its distribution, crosslinking, branching, etc. All of these changes will result in macroscopic changes of the whole structure such as changes in colour, mass, density, shape, cracks and voids [34].

The effect of elevated temperature with respect to the physical ageing of the polymer has been discussed in the last subchapter. In that particular subchapter, we have taken into consideration that the annealed polystyrene bar which has been subjected to elevated temperature has shown a different regime of physical ageing compared to those which has not been affected by the annealing process. However, in that case, there was no consideration regarding the chemical reaction the polymer would undertake with its surroundings that could be accelerated at high temperature.

Elevated temperature applied to a polymer in the presence of an aggressive chemical agent, such as oxygen, could trigger chemical reactions that may occur very slowly or even not at all at ambient temperature [7]. These exposure to aggressive chemical agent, oxygen for example, will results in fragmentation and/or the formation of a crosslinked networks [34]. These fragmentations could lead to small and volatile fragments while also keeping the molecular weight and the structure of the residual polymer remains relatively intact. The result of this phenomena is that there will be no change in the glass transition temperature  $T_g$ . However, certain phenomena such as chain scission which would decrease the molecular weight of a polymeric chain resulting in the production of large fragments throughout the whole polymer structure which temporarily stays with the polymer and cause plasticization while also forming a low-molecular-weight species, such as monomers. Changes in the molecular weight would eventually leads to the decrease in glass transition temperature  $T_g$  [35][34]. In the contrary, crosslinking between the polymeric chains may also occur during thermal degradation of a polymer. In this case, glass transition temperature  $T_g$  will increase accompanied by the possibility of char formation both in thermoplastic and thermosetting polymers as the degradation continues. It is during this phenomenon that significant changes in the glass transition temperature  $T_g$  is expected [34].

It is generally considered that heat is the major driving force in the degradation of a polymer when situated at an elevated temperature. However, there exists several other factors besides heat that would contribute to thermal degradation of a polymer. Those factors are the macromolecular structure of the polymer, environmental conditions, and additives [35]. These factors will be discussed in the following paragraphs.

Degradation of polymer structure at elevated temperature mainly involve bond scission. Bond scission require the separation of one molecule to the other, naturally it involve overcoming the bond energy formed between the two molecules. These bond energies correlate to the elemental constituents of the polymer, the type of covalent or noncovalent bonds, and degree of unsaturation [8]. As an example, polytetrafluoroethylene (PTFE) which has repeating unit of  $-(CF_2-CF_2)_n-$ , found on most non-stick cooking utensils, consists of C-F bond has the bond energy of 116 kcal/mol. Whereas polyethylene (PE) which has repeating unit of  $-(CH_2-CH_2)_n-$  and consists of C-H bond, has the bond energy of 97 kcal/mol. Since it requires higher energy, i.e. higher heat, in order to break the bond in PTFE polymers compared to PE polymers, thermal stability and therefore resiliency in deterring bond scission is higher in PTFE.

The presence of C-H bonds or unsaturation contained within the polymer chain will also ease the triggering of a thermal activated degradation process called thermo-oxidative degradation [35]. Thermo-oxidative degradation is namely so due to the presence of oxygen molecules in its degradation process. Any unsaturated C-H bonds, such as those found in natural rubber, will be absorbed by the oxygen molecules to form peroxy radicals. Whereas saturated structure, such as polyethylene PE, is more resilient to thermo-oxidative degradation.

Functional groups such as molecular weight and size, molecular weight distribution, degree of branching, cross-linking, crystallinity, and amorphousness will also have an impact on degradation [35]. Increase in molecular weight and size of the macromolecules will



heightened the thermal stability of the molecule as proven by the research of [36] which shows that thermal degradation stability of PMMA and polystyrene particles decreases as the particle size is reduced. In the case of amorphousness and crystallinity of the material, the amorphous regions in the polymer is proven to be more susceptible to thermo-oxidative degradation process due to its higher permeability to molecular oxygen compared to the crystalline regions of the polymer [37]. Branching will reduce the intramolecular and intermolecular forces within the polymer which would eventually affects the crystallinity. Therefore, branching will result in the reduction of thermal stability and making the polymer to be more susceptible to thermo-oxidative degradation process. On the other, higher number of intra- and intermolecular forces between the elements of the polymeric chain present in cross-linked structure create a higher thermal stability since it requires a simultaneous breakdown of many bonds in order to reduce the molecular weight for thermal degradation.

Besides the functional groups which are present in a polymeric material, the order of the polymers could also contribute to thermal stability. An ordered or tactic structure will generate higher thermal and thermo-oxidative degradation resiliency. A head-to-tail arrangement of polymeric chain could also enhance thermal degradation resiliency due to the copolymerization that occur between them [38].

Other factor that influence the thermal degradation of polymer is regarding the environmental condition such as humidity, temperature, and UV light which affecting the polymer structure [39]. These weathering degradation processes is slower in a hot dry climate compared to hot wet climates. Humidity, particularly at high temperature plays a huge role in increasing photodamage in polymers. Also, when the polymer is located in an oxygen rich environment, degradation is hastened due to the interaction between the polymer and the oxygen which generate reactive intermediate species.

Additives that added to the polymer could also cause the polymer to be more susceptible to thermal degradation. As an example, it is found that polyolefins polymer such as Polyethylene's (PE) oxidation could be increased by combining metal into the polymer which would act pro-oxidants [40]. Manganese (Mn) for example, when added into polyolefins which are exposed to the environment would form a free radical chain which could react with oxygen from atmosphere and form hydro-peroxides that would be hydrolysed and photolyzed. This effect may be preferable in case of fabricating a degradable polymer structure such as plastic bags which mostly made up of Polyethylene. However, in case of our polymer gasket structure, this degradative process is undesirable.

#### **2.1.2.1. The Mechanism of Thermal Degradation of Polymers**

Thermal degradation of polymers involves three major steps, namely, *initiation*, *propagation*, and *termination*. The indication of degradation in polymer structures are the formation of free radicals. Free radicals are formed due to the introduction of energy either in form of heat or electromagnetic radiation, e.g. ultraviolet (UV) radiation, which enable the

atoms or monomers inside the polymeric chains to break its bonds and form a volatile groups (radicals) which could influence other polymeric chains to form even more free radicals.

Generally, under typical situation, thermal degradation of polymer and photochemical degradation of polymer, i.e. also commonly referred to as *weathering*, both undergoes an oxidative degradation process. Oxidative degradation involves the introduction of oxygen in its process to help break down the long polymeric chains to smaller polymeric chains. The main difference between the two processes are the sequence of initiation steps which lead to the auto-oxidation cycle and the thermal degradation reactions that occur in the whole structure of the polymer compared to the degradation process that occur only on the surface in case of the photochemical degradation [41].

#### 2.1.2.1.1. Initiation Step

In its initiation, thermal degradation of polymer follows two undistinguishable processes, namely the random scission of links and the chain-end scission of C-C bonds which generate volatile products [42]. In the case of chain-end degradative process, the degradation starts at the end of the chain and successively releases monomer units, hence this process is also known as *depolymerization*. This process occurs when the backbone bonds are weaker than the bonds of the side groups which can be found on polymer molecules carrying active chain ends with a free radical, cation, anion, etc. [42]. The process of chain-end degradation could be described by Equation 11.



Where  $P_n$  is the polymer molecule with  $n$  degree of polymerization and  $R_s$  is a radical with a length of  $s$ . Chain-end degradation causes the molecular weight of the polymer to decrease slowly. However, this degradation process releases large amounts of monomers simultaneously.

The second type of degradation that occur during initiation step is the random chain scission endured by the polymeric chains. Random chain-scission will alter the long polymeric chains with high molecular weight to smaller polymer chains with lower molecular weight. The difference between this type of degradation compared to chain-end scission is the amounts of monomers that are produced during each reaction. In random chain-scission, each reaction is most likely not to produce any monomer. However, the possibility of a minor monomer to be formed may still exist. The random chain-scission could be described by Equation 12.



Unlike chain-end degradation, random chain scission does not demand the polymer chain to carry any active site [43]. When subjected to air, radicals formed from both processes in the initiation step will react with oxygen and form a reactive peroxide or hydroperoxide intermediates [35].



#### 2.1.2.1.2. Propagation Step

Thermo-oxidative degradation involves two major process during its propagation step, namely the formation of hydroperoxide and the decomposition of the said hydroperoxide [42]. Firstly, the formation of hydroperoxide is started when the polymer sample is subjected to the environment which contain oxygen molecules ( $O_2$ ). The free radicals ( $R\cdot$ ) formed during initiation step react with the oxygen from its surroundings. The result of this reaction is the formation of a peroxy radical ( $ROO\cdot$ ). Since peroxy radical is a volatile molecule, it will absorb a hydrogen atom from another polymer chain which would eventually create a hydroperoxide molecule ( $ROOH$ ).

Afterwards, the decomposition of the hydroperoxide molecule started when the generated hydroperoxide molecules splits into two new free radicals, ( $RO\cdot$ ) and ( $\cdot OH$ ). These two new radicals then are able to absorb new hydrogen molecule from other polymer chains resulting in the creation of new radicals ( $R\cdot$ ) which would repeat the hydroperoxide formation and decomposition all over again. The processes which are involved in propagation step are determined by the easiness of removing hydrogen atom from other polymer chains and the rate of termination of the free radicals via recombination and disproportionation. All of the processes above are described in the following Equations [44].



#### 2.1.2.1.3. Termination Step

At the end of thermal degradation process, the termination is done by means of coupling together the already formed radicals or by means of hydrogen absorption. The reactions that occur in termination step are always present and can be accelerated by addition of stabilizer.

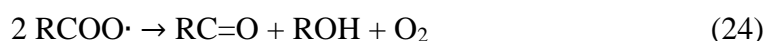
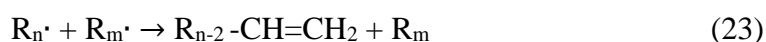
Eventually, there will be two types of mechanical properties present in the polymer as a result of termination of the free radicals. The polymer will become either more brittle or softer depending on the type of the polymer and the conditions in which the degradation process is conducted.

Polymer will become brittle whenever there is a recombination of two chain radicals, and the recombination of the two chain radicals will increase the molecular weight and crosslink density. Increase in crosslink density will eventually accelerate the formation of char in the polymer structure in addition to the possibility of formation of cracks. The following Equations describe the recombination of two radicals in the termination step [44].





Meanwhile, polymer may also become softer due to the termination of these radicals by means of chain-scission. Chain-scission will reduce the molecular weight and also its mechanical properties. The following Equations describe the termination by means of chain-scission [44].



## 2.2. Viscoelasticity of Polymeric Structure

Before we discuss about the effect of ageing on polymeric structure, it is also of importance to assess regarding the viscoelastic behaviour of polymeric structure when it is being subjected to loads. In the application of polymer gasket, the viscoelastic behaviour of the gasket will compromise its sealing capability due to the inability of the gasket to deform quickly and return to its original shape in a relatively short time as shown in Figure 1. Viscoelasticity of a material, as the name implies, means that a material will exhibit an elastic and viscous behaviour whenever it is subjected to loads. An elastic behaviour which is commonly found in most solids meaning that the material will have an instantaneous response of strain when it is being subjected to stress. The material “remember” the original dimension before its deformation and whenever the load is released, the material will return to its original shape. On the other hand, viscous behaviour which are common in most liquids, do not show similar characteristic, it exhibits a time-dependent behaviour in form of a continuous strain whenever it is being subjected to stress. The continuous strain performed by a viscous material is done in order to alleviate the stress applied to it. However, this action results in the inability of the material to return to its original shape. Both of these behaviours are dictated by the molecular reorganization making up both materials.

Polymeric structure exhibits the combination of these two behaviours however the dominant behaviour is dictated by the temperature, which correlate to the  $T_g$  of the polymer, and the frequency of the applied loads. The temperature plays an important role in the movement of the polymeric chains. As stated previously, when the temperature of the polymer is below its  $T_g$  the polymeric chains in the material will have less free volume which results in the obstructed movement of the chains. Therefore, since the polymeric chains are obstructed, the polymer can not strain easily to alleviate the stress applied to it, hence viscous behaviour is not so apparent. On the other hand, when a high heat is applied to the polymer material, the weak bonds in the polymer chains could be overcome, hence the mobility of the polymer chains

is eased. Since higher mobility is achieved, deformation in favour to reduce strain is performed, thus making the material to exhibit a viscous behaviour. However, due to the weak bonds that has been broken in the previous step, the polymer chain could not return to its original position, thus making the polymer shape to be altered. In regards to the frequency of the applied loads, longer time period between each consecutive load enable the polymer chain to creep further accompanied by the long period in the disentanglement of the polymeric chains which help the material to alleviate stress applied to it by forming further strain deformation. These explanations can be depicted in Figure 12.

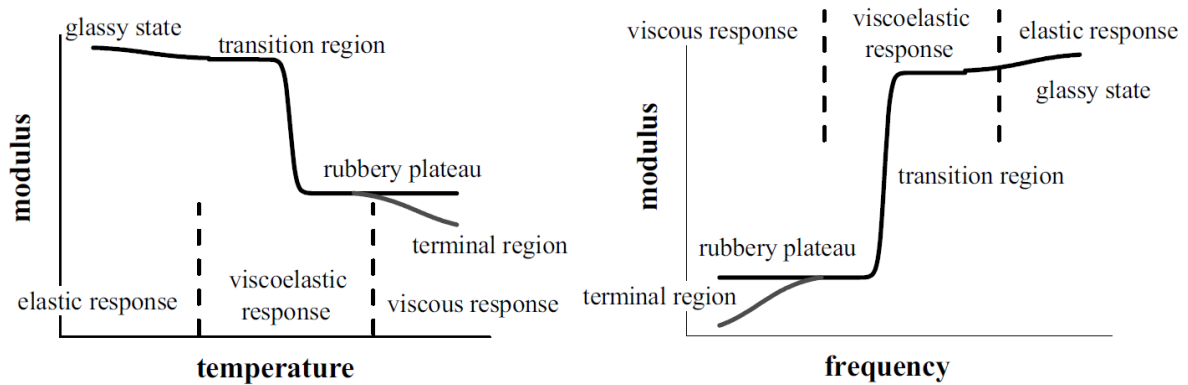


Figure 12: Viscoelastic behaviour of polymer shown by its Young's modulus with respect to temperature and load frequency. [45]

Viscoelastic behaviour of a material could be described by mechanical models which consists of elastic spring which represent the elastic behaviour and viscous dashpots which represent the viscous behaviour. There are two most well-known models which described the viscoelastic behaviour of a material, namely, the Kelvin-Voigt model and the Maxwell model. Both models have their own advantage and limitation in describing viscoelastic behaviour.

### 2.2.1. Kelvin-Voigt Model

Kelvin-Voigt model describe viscoelastic behaviour by utilizing spring with a modulus of  $E_k$  and dashpot with viscosity of  $\eta_k$  in a parallel configuration as shown in Figure 13. In this model, stress applied will be shared by the spring and dashpot. On the other hand, the resulting strain endured by both components will be the same. Mathematically the stress and strain could be described by the following Equations.

$$\text{Total stress} = \sigma_{total} = \sigma_{spring} + \sigma_{dashpot} \quad (25)$$

Where  $\sigma_{spring}$  and  $\sigma_{dashpot}$  is described as:

$$\sigma_{spring} = E_{spring} * \epsilon \quad (26)$$

$$\sigma_{dashpot} = \eta_{dashpot} * \frac{d\epsilon}{dt} \quad (27)$$

Therefore, total stress could be written as:

$$\sigma_{total} = E_{spring} * \varepsilon + \eta_{dashpot} * \frac{d\varepsilon}{dt} \quad (28)$$

$$\text{Total strain} = \varepsilon_{total} = \varepsilon_{spring} = \varepsilon_{dashpot} \quad (29)$$

Due to the presence of the dashpot which located in parallel to the spring, strain could not exist instantaneously. However, strain will increase with respect to time. Therefore, there will be a dependency to viscosity in which deformation could occur, i.e. a creeping phenomenon will occur during loading and unloading. Beside creeping phenomenon, due to the loss in energy caused by the viscous behaviour, i.e. energy needed to push the dashpot, there will be a permanent strain remain on the material after unloading cycle is conducted. The resulting deformation which is represented by the strain with respect to time is shown in Figure 14.

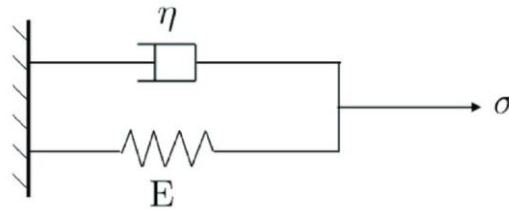


Figure 13: Kelvin-Voigt model. [46]

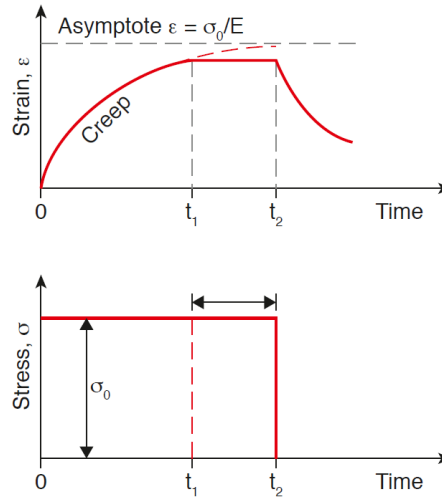


Figure 14: Creep, relaxation, and recovery in Kelvin-Voigt model. [47]

Kelvin-Voigt model could describe creeping phenomenon occur in most polymeric material during loading and unloading quite perfectly. Under constant stress (creep) the strain deformation endured can be described by Equation 30.

$$\varepsilon(t) = \varepsilon_0 \exp \left( -\frac{t}{\tau} \right) \quad (30)$$

In terms of creep compliance it could be written as Equation 31.

$$\varepsilon(t) = J\sigma \left[ 1 - \exp \left( -\frac{t}{\tau} \right) \right] \quad (31)$$

Where  $J$  denotes the creep compliance factor and  $\tau$  denotes the relaxation time which correlates to  $\frac{E_{spring}}{\eta_{dashpot}}$ .

While Kelvin-Voigt model is excellent in describing the creep behaviour of a viscoelastic polymer, it is unable to describe stress relaxation which occur in viscoelastic polymer. Stress relaxation is a phenomenon in viscoelastic material where whenever a constant deformation is quickly applied and held, the stress inside the material caused by the deformation is slowly reduced. In Kelvin-Voigt model referring to Equation 28, whenever a constant strain is applied ( $\frac{d\varepsilon}{dt} = 0$ ) the stress inside the material does not decay overtime however it would remain constant at  $E_{spring} * \varepsilon$  as shown in Equation 32.

$$\sigma_{total} = E_{spring} * \varepsilon + \eta_{dashpot} * 0 = E_{spring} * \varepsilon \quad (32)$$

### 2.2.2. Maxwell Model

Maxwell model on the other hand describe the viscoelasticity behaviour of polymer by placing the spring and dashpot in a series configuration as shown in Figure 15. Stress applied to this model will have an instantaneous deformation or change in strain due to its elastic behaviour represented by the spring component, then further strain will occur due to the viscous behaviour represented by the dashpot component. The instantaneous deformation caused by the elastic is a reversible deformation whereas the time-dependent creep deformation is an irreversible deformation. In this configuration the total stress applied will be the same between the spring and the dashpot, whereas the total strain is the accumulation from the strain exhibited by the spring and the dashpot.

$$\text{Total stress} = \sigma_{total} = \sigma_{spring} = \sigma_{dashpot} \quad (33)$$

Where  $\sigma_{spring}$  could be described as:

$$\sigma_{spring} = E_{spring} * \varepsilon \quad (34)$$

$$\frac{d\sigma_{spring}}{dt} = E_{spring} * \frac{d\varepsilon_{spring}}{dt} \quad (35)$$

$$\text{Total strain} = \varepsilon_{total} = \varepsilon_{spring} + \varepsilon_{dashpot} \quad (36)$$

The total strain rate could be written as:

$$\text{Total strain rate} = \frac{d\varepsilon}{dt} = \frac{1}{E_{spring}} * \frac{d\sigma}{dt} + \frac{\sigma}{\eta_{dashpot}} \quad (37)$$

Rearranging the above Equation we obtain the Maxwell's model in differential form

$$\sigma + \frac{\eta_{dashpot}}{E_{spring}} \frac{d\sigma}{dt} = \eta_{dashpot} \frac{d\varepsilon}{dt} \quad (38)$$

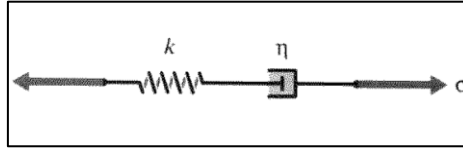


Figure 15: Maxwell's model of viscoelasticity. [48]

The advantage of Maxwell model in describing viscoelastic behaviour compared to Kelvin-Voigt model is that it can describe the stress relaxation phenomenon occurring in viscoelastic polymeric material. Stress relaxation of a viscoelastic material is a phenomenon where the stress it endures due to constant deformation decays over time, as shown in Figure 16. Referring to Equation 37, whenever a constant strain is applied and held, the rate of stress will decay over time as shown in following Equations.

$$\frac{d\varepsilon}{dt} = 0 = \frac{1}{E_{spring}} * \frac{d\sigma}{dt} + \frac{\sigma}{\eta_{dashpot}} \quad (39)$$

Rearranging Equation 39 we obtain

$$\frac{d\sigma}{\sigma} = - \frac{E_{spring}}{\eta_{dashpot}} dt \quad (40)$$

Integrating Equation 40 we obtain

$$\int_{\sigma_0}^{\sigma} \frac{d\sigma}{\sigma} = - \int_0^t \frac{E_{spring}}{\eta_{dashpot}} dt \quad (41)$$

$$\sigma(t) = \sigma_0 \exp\left(-\frac{t}{\tau}\right) \quad (42)$$

In Equation 42,  $\tau$  represent the relaxation time, i.e. the time it took until stress is  $1/e$  of its initial value and it is described as

$$\tau \equiv \frac{E_{spring}}{\eta_{dashpot}} \quad (43)$$

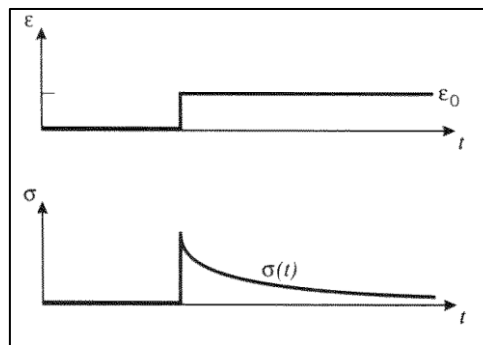


Figure 16: Strain and stress with respect to time in stress relaxation. [48]

On the other hand, this model could not describe creep behaviour as well as Kelvin-Voigt model. Creep, i.e. constant stress, applied to this model during loading will result in the increase of strain with respect to time after an instantaneous deformation. Recovery on the hand showing an instantaneous decrease in strain from the elastic part however there is no apparent recovery from the viscous part. This Newtonian flow behaviour is generally not true for most viscoelastic

material. The rate of change in strain in Maxwell model referring to Equation 37 under constant stress ( $\frac{d\sigma}{dt} = 0$ ) is described in Equation 44.

$$\frac{d\varepsilon_{spring}}{dt} = \frac{1}{E_{spring}} * 0 + \frac{\sigma}{\eta_{dashpot}} = \frac{\sigma}{\eta_{dashpot}} \quad (44)$$

As can be seen from Equation 44, under constant stress the rate of change in the strain is positive, whereas in reality it is decreasing as described by the Kelvin-Voigt model.

### 2.2.3. Standard Linear Solid Model

Since both models mentioned above have their own limitation in describing viscoelastic behaviour, a new model namely the standard linear solid model, is made. Standard linear solid model of viscoelastic behaviour is used to simulate the short-term behaviour of solid polymer components. It is modelled by utilizing the Maxwell's model for viscoelasticity with the addition of a spring attached in parallel with it as shown in Figure 17.

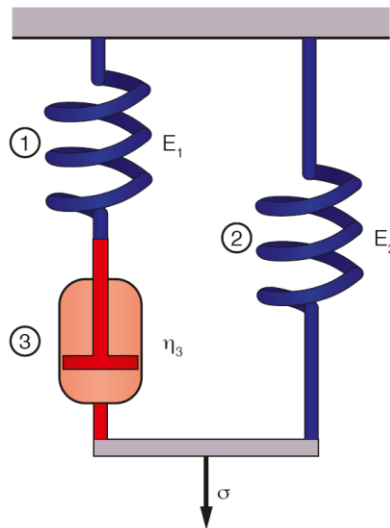


Figure 17: Standard Linear Solid Model configuration. [47]

The addition of an extra spring attached in parallel with the Maxwell's model enable Standard Linear Solid Model to mimic the creeping behaviour present in most viscoelastic material under constant stress which is an advantage over the Maxwell's model where it exhibits an unrestricted flow or deformation during constant stress. Creeping behaviour, which limit conformational change of the polymer, exist in most polymer due to the limitation caused by the network of entanglement of the polymeric chains or other types of junction points [48]. The behaviour of standard linear solid model during creep, relaxation, and recovery is shown in Figure 18.

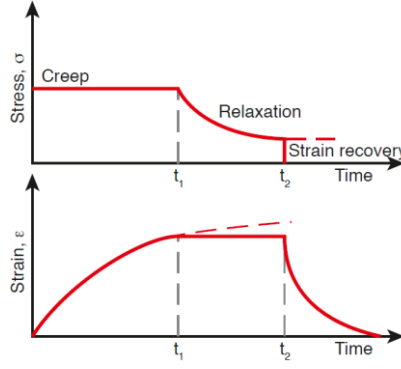


Figure 18: Creep, relaxation and recovery response of standard linear solid model. [47]

In the configuration shown in Figure 17, the stress applied to the model will be shared between the Maxwell's model part and the extra spring, i.e. total stress will be the sum of the stress endured by the Maxwell's model part and the additional spring. On the other hand, strain endured will be the same between the Maxwell part and the extra spring. The total stress endured can be formulated by the following Equations [47].

$$\sigma_{total} = \sigma_{spring\ 1} + \sigma_{spring\ 2} \quad (45)$$

$$\sigma_{spring\ 1} = \sigma_{dashpot} \quad (46)$$

Whereas the strain could be described by the following Equations [47].

$$\varepsilon_{total} = \varepsilon_{spring\ 1} + \varepsilon_{dashpot} \quad (47)$$

$$\varepsilon_{total} = \varepsilon_{spring\ 2} \quad (48)$$

Combining the Equations from 45 through 48 and using the equations for stress and strain for both spring and dashpot, the equation for standard linear solid model could be described as [47]:

$$\eta \frac{d\sigma}{dt} + E_{spring\ 1} \sigma = \eta (E_{spring\ 1} + E_{spring\ 2}) \frac{d\varepsilon}{dt} + E_{spring\ 1} E_{spring\ 2} \varepsilon \quad (49)$$

Where the strain during creep could be described as [47]:

$$\varepsilon = \frac{\sigma_0}{E_{spring\ 2}} + \left( \frac{\sigma_0}{E_{spring\ 1} + E_{spring\ 2}} - \frac{\sigma_0}{E_{spring\ 2}} \right) e^{-\left( \frac{E_{spring\ 1} E_{spring\ 2}}{\eta (E_{spring\ 1} + E_{spring\ 2})} \right) t} \quad (50)$$

Stress during stress relaxation is solved as [47]:

$$\sigma = \varepsilon_0 (E_{spring\ 2} + E_{spring\ 1}) e^{-\left( \frac{E_{spring\ 1}}{\eta} \right) t} \quad (51)$$

### 2.3. Effect of Ageing on Polymeric Structure

In the previous subchapter we have discussed regarding the probable causes which would age a polymeric material, namely due to physical ageing and thermal ageing. In this subchapter, the author would like to elaborate regarding the effect of ageing on polymer material



specifically in terms of the changes it causes in mechanical properties. Changes in mechanical properties is important in the application of polymer as a gasket due to the alteration in its sealing capabilities.

As mentioned previously, changes in mechanical properties of a polymer during physical ageing is mostly contributed by the increase in the density of the material. Changes made to the density of the material is related to the free volume ( $V_f$ ) inside the polymer. As explained, the reduction in the free volume limits the segmental mobility of the polymeric chains ( $M$ ) inside it. Since segmental mobility is limited, the mechanical properties of the glassy polymer material will be influenced by ageing due to the changes in the relaxation times [31]. Creep or stress relaxation will be longer in the time scale the longer the ageing time takes place, i.e. the tensile creep compliance will be reduced.

Considering the creep compliance is reduced, polymer structure could not deform fast enough to relieve the stress applied upon it during loading. The resulting effect of this phenomenon is the structure will become stiffer and sufficiently high loads will results in the formation of cracks inside the structure. During unloading on the hand, the limitation of the segmental mobility makes the polymeric chains to require more time in order to try to return to its original dimension. However, the structure could not return to its original dimension since it has loss some of its energy in order to creep by overcoming the weak bonds during loading.

Degradation in mechanical properties endured by the polymer due to thermal ageing is mostly contributed by the changes made on its polymeric chain constituents. As mentioned previously, during the termination step in thermal degradation of a polymer two possible reactions which are affecting the radicals are present, namely crosslinking and chain scission. Crosslinking will increase the molecular weight of the radical whereas chain scission will result in the reduction of the molecular weight.

Cross links that are present inside a polymeric material will greatly reduces its creep capabilities. Additional cross links that are formed as a result of thermal degradation will further decrease the creep rate. Decrease in creep rate will turn the polymer material to be less ductile, therefore limiting the rate of deformation it can withstand. These limitations eventually could cause cracks inside the material. Cross linking has no major effect on creep of polymers at temperatures far below their glass transition region. Polymers far below their glass transition region is already showing a rigid behaviour, i.e. molecular motions are so frozen, that an additional restriction made by cross links hardy noticeable. However, high loads done on the polymer, loads at very long times, or temperatures not far below the polymer glass transition temperature, crosslinking should reduce creep [49].

## 2.4 Strain Gauge

Strain gauge plays an important role in this master thesis due to the fact that strain gauges enables the possibility to measure the deformation applied or conducted by a structure in term of its strain. At previous chapters the author has described regarding the degradation affecting the polymer gasket which would eventually affects the behaviour of deformation it made under

applied stress either in form of a time dependent creeping behaviour during loading or the permanent strain deformation after unloading. These defects caused by ageing could be identified with the help of strain gauge embedded inside the polymer gasket.

The amount of strain deformation measured by the strain gauge is performed by means of measuring the change of resistivity exhibited by the strain gauge. Strain gauge sensors are able to exhibit a change in its resistivity due to the elongation or contraction affecting the metallic conductor or semiconductor contained within it. Whenever the gasket is deformed by means of applied stress or due to ageing, strain gauge sensor embedded inside it will also be deformed causing the change in the conformation of the metallic conductor or semiconductor inside it.

Most strain gauges are constructed in form of an active elements which consists of metallic conductors or semiconductor placed in a meandering configuration with the addition of contact pads at the end of each path which then could be connected with wires to measure the electrical resistance change made towards the strain gauges as shown in Figure 19. Changes in electrical resistance  $\left(\frac{\Delta R}{R}\right)$  of the strain gauge caused by its deformation could be formulated by the Equation 52.

$$\frac{\Delta R}{R} = \varepsilon * G_f \quad (52)$$

Where  $\varepsilon$  represent the strain deformation of the strain gauge and  $G_f$  represent the gauge factor of the active element of the strain gauge.

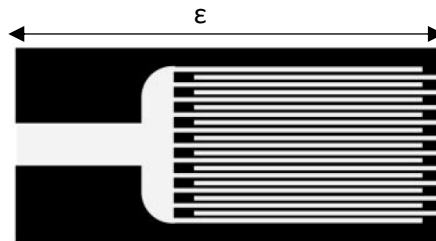


Figure 19: Foil strain gauge geometry. [50]

Gauge factor ( $G_f$ ) correlates the amount of strain applied to the strain gauge with the corresponding electrical resistance and it is defined as:

$$G_f = \frac{\Delta R/R}{\Delta L/L} = \frac{\Delta R/R}{\varepsilon} \quad (53)$$

Gauge factor of the active element of the strain gauge varied between each possible conducting metal or semiconductor. Therefore, it is important to establish an understanding about the correlation between the change in electrical resistance with strain in the conducting active element of the strain gauge. Resistance in any conductive path could be described as Equation 54 and pictured in Figure 20:

$$R = \rho \frac{L}{A} \quad (54)$$

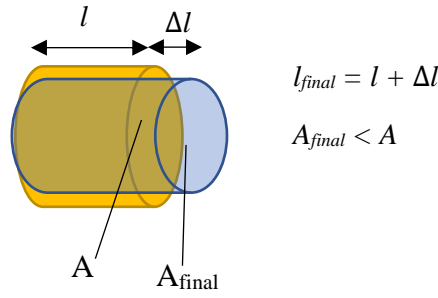


Figure 20: Relation between strain and electrical properties of a conducting path

Where  $\rho$  denotes the specific electrical resistance,  $L$  denotes the length, and  $A$  denotes the area of the conductive element.

As can be seen from Figure 20, deformation done towards a conductive element, e.g. by means of elongating it, will change the geometry and therefore its crystal lattice. These changes will eventually lead to the change of electrical resistivity as described in Equation 54. It is also important to note that during such deformation material could also exhibit Poisson effect. Poisson effect states that a material will also deform in the direction perpendicular to the applied deformation. In the case of Figure 20, since the conductive path is deformed by means of elongating it, the conductor is also deformed perpendicularly shown by the reduction in its area, i.e. its thickness.

Beside geometrical aspect, specific electrical resistivity ( $\rho$ ) change could also affect the gauge factor of the active element of the strain gauge. These changes in specific electrical resistivity is caused by the piezoresistive effect exhibited by some conductor or semiconductor when utilized as the active element of the strain gauge. Strain deformation made to conductor or semiconductor will affect the inter-atomic spacing inside it which would eventually affect the bandgaps of the electrons. Changes in the bandgaps will result in the ability of the electron to jump into the conductive band which would eventually dictates the electrical conductivity of the material. During elongation by means of applying a high tensile stress for example, inter-atomic spacing of the material increases, therefore the potential to bound electrons within the atom decreases making the bandgap smaller which would in turn ease the electron to be excited to the conductive band. The equation governing the change in resistivity with respect to mechanical deformation, i.e. piezoresistive coefficient  $\rho_c$ , could be described as:

$$\rho_c = \frac{\Delta\rho}{\rho \cdot \varepsilon} \quad (55)$$

Therefore, gauge factor of the active element of strain gauge with respect to geometrical change and the change in specific electrical resistivity could be explained as [50][51]:

$$G_f = 1 + 2\nu + \frac{d\rho}{\rho \varepsilon} = 1 + 2\nu + \pi \varepsilon \quad (56)$$

Where  $\nu$  represents the Poisson's ratio of the material and  $\pi$  represents the piezoresistive coefficient ( $\text{m}^2/\text{N}$ ). As can be seen from Equation 56, the segment  $1+2\nu$  represent the geometrical aspect whereas the  $\left(\frac{d\rho}{\rho \varepsilon}\right)$  segment represent the piezoresistive aspect. Incompressible materials, i.e. materials which shows no change in volume during deformation,

would exhibit a Poisson's ratio of 0.5 therefore the segment  $1+2\nu$  is equal to 2. In most metals the geometrical aspect dominates the determination of the gauge factor compared to its piezoresistive effect, where the geometrical aspect provides a  $G_f$  of 1.4 to 2.0 compared to the 0.3 contribution from its piezoresistive aspect [52].

### 2.4.1. Wheatstone Bridge

In its application, the measured change in resistance data gathered from strain gauges during deformation is relatively small, i.e. in order to measure strain accurately a very small changes in resistance must be detected. Therefore, it is beneficial to implement a signal processing circuit which is able to amplify the changes in resistance exhibited by the strain gauge. The most common method in order to achieve this is by treating the strain gauge as one, or more, of the resistances in a Wheatstone bridge circuit as shown in Figure 21.

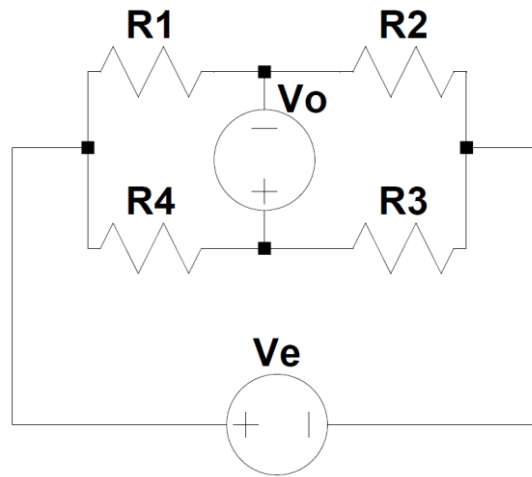


Figure 21: Wheatstone bridge

Wheatstone bridge circuit is made up of four resistive components and an excitation voltage  $V_e$ . The voltage measured as a result of this configuration is indicated as voltage output  $V_o$ . Therefore, from this configuration, the output voltage could be formulized as:

$$V_o = V_e \left( \frac{R_3}{R_3 + R_4} - \frac{R_2}{R_1 + R_2} \right) \quad (57)$$

As can be seen from Equation 57, the output voltage value could be amplified by the excitation voltage  $V_e$ . Also, it should be noted that whenever  $R_3/R_4 = R_1/R_2$ , the output voltage  $V_o$  will be zero. It is important during the initial installation of the strain gauges or before strain deformation occur to achieve this condition, i.e.  $R_{sg} = R_1 = R_2 = R_3 = R_4$ . This is done in order to achieve output voltage reading after strain deformation occur is due to the changes in resistance exhibited by the strain gauges. Therefore, proper sizing of the resistances used to accompany the strain gauges should be conducted.

As an example, changing  $R_1$  in the Wheatstone bridge to the total resistance of the strain gauge  $R_{sg, total} = R_{sg} + \Delta R_{sg}$ , leads to the quarter bridge configuration of the Wheatstone bridge as shown in Figure 22 and explained in Equation 58.

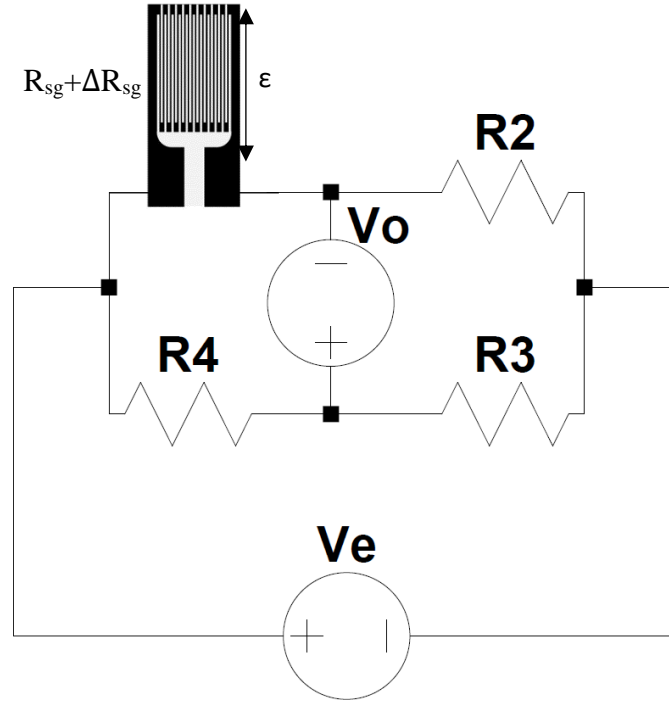


Figure 22: Quarter bridge configuration. Strain gauge figure taken from [50].

$$V_o = V_e \left( \frac{R_3}{R_3 + R_4} - \frac{R_2}{R_{sg} + \Delta R_{sg} + R_2} \right) \quad (58)$$

Since  $R_{sg} = R_1 = R_2 = R_3 = R_4$ , therefore:

$$V_o = V_e \left( \frac{1}{2} - \frac{R_{sg}}{R_{sg} + \Delta R_{sg} + R_{sg}} \right) \quad (59)$$

Equalizing the nominator results in:

$$V_o = V_e \left( \frac{\Delta R_{sg}}{4R_{sg} + 2\Delta R_{sg}} \right) \quad (60)$$

Approximation of  $R_{sg} \gg \Delta R_{sg}$  has been made since changes in resistance of the strain gauge is significantly smaller than its initial resistance, therefore:

$$V_o \approx V_e \left( \frac{\Delta R_{sg}}{4R_{sg}} \right) \quad (61)$$

Rearranging Equation 61 will obtain the voltage output with respect to the changes in resistance of the strain gauges:

$$4 \frac{V_o}{V_e} \approx \left( \frac{\Delta R_{sg}}{R_{sg}} \right) \quad (62)$$

Of course, the sensitivity of the strain gauge system could be improved by means of adding an extra strain gauge as  $R_2$  which results in the half bridge configuration or even replacing all the resistance with strain gauges altogether resulting in the full bridge configuration, as shown in Figure 23 and 25 respectively. However, in the case of half bridge configuration, higher sensitivity is achieved if the second strain gauge is placed where it will compress under deformation, i.e.  $R_{sg2, total} = R_{sg2} - \Delta R_{sg2}$ . Resulting in the equations below:

$$V_o = V_e \left( \frac{1}{2} - \frac{R_{sg} - \Delta R_{sg}}{R_{sg} + \Delta R_{sg} + R_{sg} - \Delta R_{sg}} \right) \quad (63)$$

$$V_o = V_e \left( \frac{1}{2} - \frac{R_{sg} - \Delta R_{sg}}{2R_{sg}} \right) \quad (64)$$

$$V_o = V_e \left( \frac{2\Delta R_{sg}}{4R_{sg}} \right) \quad (65)$$

$$2 \frac{V_o}{V_e} = \left( \frac{\Delta R_{sg}}{R_{sg}} \right) \quad (66)$$

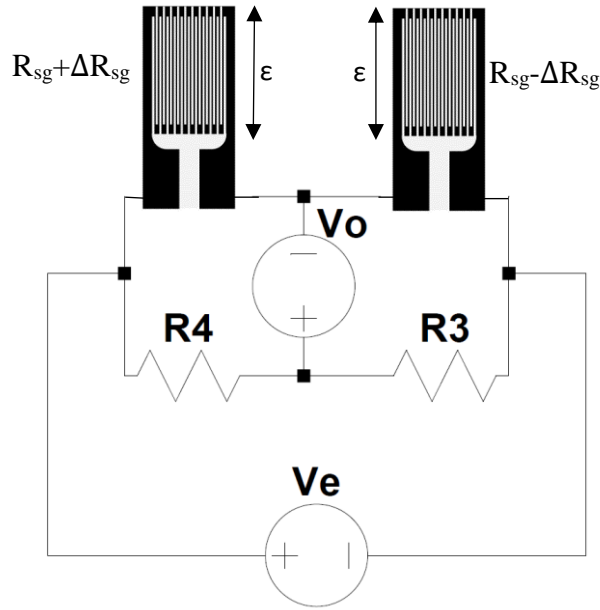


Figure 23: Half bridge configuration. Strain gauges figure taken from [50].

This configuration of half bridge may be beneficial in measuring the deformation that occur in cantilever when subjected to force, where strain and compression occur in opposite sides. However, in the implementation of a gasket in this master thesis, the gasket is subjected to force which will expand the gasket radially, therefore most deformation is in form of radial strain of the gasket as shown in Figure 1. Thus, half bridge configuration will be beneficial in amplifying the change in resistance in case of gasket deformation if the second strain gauge replace  $R_3$ , where strain endured by both strain gauges in this configuration will increase the sensitivity of the measurement [53], as proven in equations below:

$$V_o = V_e \left( \frac{R_{sg} + \Delta R_{sg}}{R_{sg} + \Delta R_{sg} + R_4} - \frac{R_2}{R_{sg} + \Delta R_{sg} + R_2} \right) \quad (67)$$

Since  $R_{sg} = R_2 = R_4$  in order to satisfy  $V_o = 0$  during initial step, therefore:

$$V_o = V_e \left( \frac{R_{sg} + \Delta R_{sg}}{2R_{sg} + \Delta R_{sg}} - \frac{R_{sg}}{2R_{sg} + \Delta R_{sg}} \right) \quad (68)$$

$$V_o = V_e \left( \frac{\Delta R_{sg}}{2R_{sg} + \Delta R_{sg}} \right) \quad (69)$$

With approximation of  $R_{sg} \gg \Delta R_{sg}$ , the resulting equation will be:

$$V_o = V_e \frac{1}{2} \left( \frac{\Delta R_{sg}}{R_{sg}} \right) \quad (70)$$

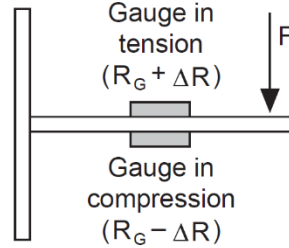


Figure 24: Deformation in cantilever. [54]

An even higher sensitivity towards the change of resistivity could be achieved by means of replacing all the resistances in the Wheatstone bridge with strain gauges which results in the full bridge configuration shown in Figure 25. However, if amplification in the change of resistance is desired, based on Equation 57, the resistance at R1 and R3 must be replaced with strain gauges that experience tensile deformation whereas the resistance at R2 and R4 is replaced with strain gauges that endured compressive deformation. The equation for describing the correlation between the voltage output and the change in resistance is described as follows:

$$V_o = V_e \left( \frac{R_{sg} + \Delta R_{sg}}{R_{sg} + \Delta R_{sg} + R_{sg} - \Delta R_{sg}} - \frac{R_{sg} - \Delta R_{sg}}{R_{sg} + \Delta R_{sg} + R_{sg} - \Delta R_{sg}} \right) \quad (71)$$

$$V_o = V_e \left( \frac{\Delta R_{sg}}{R_{sg}} \right) \quad (72)$$

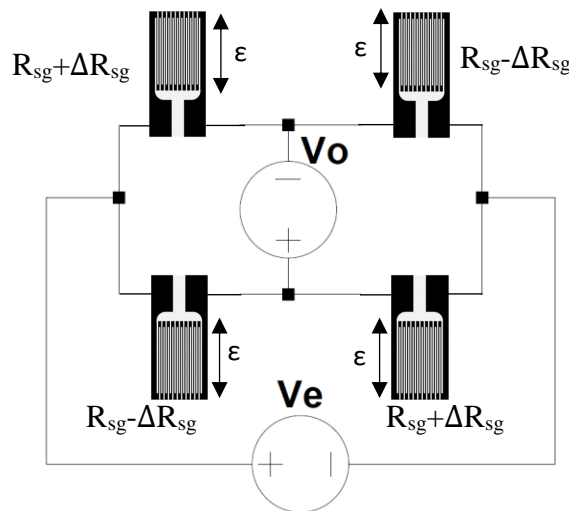


Figure 25: Full bridge configuration. Strain gauge figure taken from [50]

Measurement done using Full bridge configuration can be beneficial for example during the installation of an O-ring gasket. As explained previously, in order to produce voltage output of 0 during its initial step a similar value of resistance must be achieved. In the case of faulty installation where there is an uneven compression affecting the gasket, an uneven value of



resistance is produced by the strain gauges which eventually produce an offset value to the output voltage.

## 2.5 Temperature Dependency of Strain Gauge

Although the main reason of using strain gauge is to measure the strain applied to it by means of measuring the change in its electrical resistivity, other factor such as temperature will also affect the change of electrical resistivity of a strain gauge [50]. Changes in resistivity of the strain gauge caused by temperature is mostly contributed by the conductors acting as the active element of the strain gauge. These changes in resistivity of the conductors is linear with the change of temperature and it is correlated with temperature coefficient of resistance  $\alpha$  specific to each material. The equation of changes in resistivity due to temperature could be described as:

$$\frac{\Delta R}{R} = \alpha \Delta T \quad (73)$$

Naturally, in typical application of the strain gauge where only changes in resistance caused by strain is desired, these resistance changes due to temperature is unwanted. Therefore, a temperature compensation component is required in the strain gauge measurement system to mitigate the effect from temperature. The temperature compensation component which is common nowadays is the addition of a similar second strain gauge, namely the *passive strain gauge*, which is not sensitive to strain however it is still affected by the more or less similar temperature affecting the strain sensitive *active strain gauge*. A passive strain gauge could be made insensitive to strain due to the orientation of the meandering active element of the strain gauge which is placed perpendicular to the intended strain deformation, as shown in Figure 26. Due to the similarities in the temperature affecting both strain gauges, if the strain gauges are placed in a half bridge configuration where R1 is replaced by the active strain gauge and R2 is replaced by the passive strain gauge. The ratio of the resistance  $\left(\frac{R_1}{R_2}\right)$  in the end does not change even though both experience an increase in its resistance caused by temperature. Therefore, output voltage ( $V_o$ ) changes caused by temperature does not occur and the effects of temperature change are minimized.

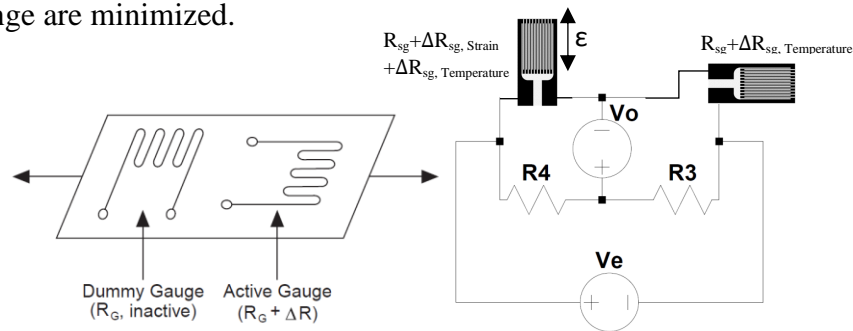


Figure 26: Temperature compensation using two strain gauges [54] (left) temperature compensated half-bridge configuration (right)

## 2.6 Simultaneous Measurement of Strain and Temperature

In typical utilization of strain gauges, the increase in electrical resistance caused by temperature might not be desirable during measurement. Therefore, temperature compensation is normally implemented in most strain gauge measurement systems. However, recent study conducted by Brinksmeier, et.al. [13] regarding *process signature* has shown that by being able to measure the amount of energy dissipated towards a material, changes towards the material properties in the subsurface zone could be correlated. The simplest way to measure the energy dissipated towards a material is by means of measuring its temperature.

Several methods have been established in measuring temperature of a workpiece. The most common practice is the insertion of thermocouple inside the workpiece [55][56]. The insertion is done by means of drilling a hole into the workpiece and afterwards thermocouple is inserted into it. Practically speaking, a simultaneous measurement of the strain and temperature could be achieved this way, e.g. using thermocouple to measure the temperature and utilizing a half-bridge Wheatstone strain gauge configuration to measure the strain without affected by temperature. Although this method is relatively simple, often times the data gathered by the thermocouple could not be regarded as actual temperature inside the workpiece. This is due to the accuracy and response of the thermocouple is not sufficient caused by the poor thermal coupling of the workpiece to the sensing element. Poor thermal coupling often caused by the housing of the thermocouple. Therefore, a sensing element which could directly in contact with the workpiece and is exposed to the same strain and temperature as the workpiece can be beneficial, one of the alternatives is the utilization of strain gauge as temperature measurement.

As mentioned previously, strain gauge is sensitive due strain and temperature. This sensitivity will be exhibited by the changes in resistance. Combining both effects together, the equation for changes in resistance caused by temperature and strain can be described as [12]:

$$\left(\frac{\Delta R}{R}\right) = \frac{\Delta R_{strain} + \Delta R_{temperature}}{R} = \varepsilon * G_f + \Delta T * \alpha \quad (74)$$

As observed from Equation 74, in order to determine the strain and temperature affecting the host material of the strain gauge, a single strain gauge is not sufficient since the changes in its resistance is caused by two unknown variables namely the strain and the temperature difference. A study conducted by Gräbner [12] has shown that by the utilization of two strain gauges placed in nested shape and each with different material characteristics, i.e. different gauge factor ( $G_f$ ) and temperature coefficient of resistance ( $\alpha$ ) as shown in Equation 75 and 76, the determination of temperature and strain affecting the strain gauges host material could be conducted.

$$\left(\frac{\Delta R}{R_{sg1}}\right) = \varepsilon * G_{f,mat1} + \Delta T * \alpha_{mat1} \quad (75)$$

$$\left(\frac{\Delta R}{R_{sg2}}\right) = \varepsilon * G_{f,mat2} + \Delta T * \alpha_{mat2} \quad (76)$$

By combining and rearranging the above equations, strain and temperature affecting the strain gauges can be measured by [12]:

$$\Delta T = \frac{G_{f,mat1} * \frac{\Delta R}{R_{sg2}} - G_{f,mat2} * \frac{\Delta R}{R_{sg1}}}{G_{f,mat1} * \alpha_{mat2} - G_{f,mat2} * \alpha_{mat1}} \quad (77)$$

$$\varepsilon = \frac{\alpha_{mat2} * \frac{\Delta R}{R_{sg1}} - \alpha_{mat1} * \frac{\Delta R}{R_{sg2}}}{G_{f,mat1} * \alpha_{mat2} - G_{f,mat2} * \alpha_{mat1}} \quad (78)$$

Naturally, in order to utilize these equations the temperature coefficient of resistance and gauge factor of both strain gauges must be known. Therefore, tests in order to characterize each strain gauge materials must be conducted before the integration of the sensor towards the gasket. As shown by the equations above, temperature compensation, i.e. removing the effect of changes in resistance caused by temperature, is also achieved by means of obtaining both measurements for strain and temperature separately using the technique described in this subchapter.

A nested shape design for the two strain gauges, as shown in Figure 3 is chosen in this research due to the fact that in dynamic machining process where very high spatial temperature strain occurs, the influence they have towards the strain gauges will not differ from one another since the strain gauges are located close to each other, i.e. the strain gauges will be affected by the same temperature and strain from its host workpiece. This benefit might not be the same when the temperature measurement is done by thermocouple or temperature compensation done by half bridge configuration. Other benefits of utilizing a nested shape is in the reduction of size of the sensor compared to other temperature measurement techniques.

# CHAPTER 3

## Research Methodologies

This master thesis revolves around the simultaneous measurement of strain and temperature affecting the gasket which then could be utilized in determining its condition during application. In order to do so, several methods have been established in the preceding chapters such as the use of thermocouple accompanied by half-bridge Wheatstone strain gauge configuration and the utilization of two strain gauges in nested configuration. However, since the subject of research in this master thesis is the gasket itself which is relatively small in its dimensions, the use of a bulky sensor such as the thermocouple with two additional strain gauges may disrupt the mechanical stability of the gasket. Therefore, the use of nested strain gauge due to its small structure and precise measurement is preferred.

### 3.1. Strain Gauge Materials Selection

In fabricating strain gauges used in the nested strain gauges configuration, deciding the materials which are going to be used is of importance. Two major sections of the strain gauge namely the active element and the substrate will have great impact towards the applicability of the nested strain gauges in a gasket. Incompatibility of the nested strain gauges to the gasket host structure leads to the inaccurate measurement of the strain gauges with respect to the conditions endured by the gasket, breakage of the strain gauges, or even worse, the gasket will have an early deformation caused by the embedded strain gauges, i.e. the gasket perceives the strain gauges as a foreign body. Therefore, the conditions that have to be met by the strain gauges is explained in the following paragraphs.

#### 3.1.1. Strain Gauge Active Elements, Conducting Paths and Contacts Materials

First and foremost, the most important condition that has to be met by the strain gauges is the change in its measurable output due to the strain deformation and temperature affecting the gasket which also affects the strain gauges embedded inside it. One of the most measurable output is the change in its resistance. A sensitive strain gauge which is represented by the large readout in the change of electrical resistance is desirable since it will produce an accurate measurement at even small strains. Currently there are many candidate materials that meet this condition and can be used as the strain gauge active element and they are classified as metal, semiconductor, and elastic strain gauge active elements [51].

Metallic and semiconductor strain gauges are typically suited to measure small displacement usually less than 20 $\mu$ m and typically require large actuation force, unlike the elastic strain gauge classification where it is more suitable to measure rather large displacement [51]. This order of displacement is what we anticipate during the deformation of our gasket and also considering the amount of force that the gasket along with the strain gauges will be

subjected to, therefore it is reasonable to choose between semiconductor and metallic strain gauge active elements.

Since the output in the form of resistance is desired, it is also important therefore to consider how both materials will exhibit their change of resistance when subjected to strain deformation and also to temperature changes. As mentioned in previous chapter in Equation 52, the amount of resistance changes affecting the strain gauge active elements, i.e. its sensitivity, is dictated by the gauge factor ( $G_f$ ) of the materials making up the strain gauge active elements. Gauge factor in metal is mostly influenced by the geometrical aspect denoted by the  $1+2\nu$  segment in Equation 56. However, piezoresistive effect, noted by the  $\left(\frac{d\rho}{\rho\varepsilon}\right)$  segment, still has an impact to the total gauge factor value [52]. In the case of metallic strain gauges, many of them have a Poisson's ratio ( $\nu$ ) between 0.25 and 0.35, resulting in the  $1+2\nu$  segment to produce a value around 1.5 to 1.7 [50]. Small contribution to gauge factor due to the piezoresistive effect at around 0.3 [52] rounds up the common gauge factor for most metal to be around 2. The following table shows the gauge factor of several metallic strain gauges [50][52].

Materials	Gauge Factor
Platinum (Pt 100%)	+6.1
Platinum-Indium (Pt 95%, Ir 5%)	+5.1
Platinum-Tungsten (Pt 92%, W 8%)	+4.0
Isoelastic (Fe 55.5%, Ni 36%, Cr 8%, Mn 0.5%)	+3.6
Constantan/Advance/Copel (Ni 45%, Cu 55%)	+2.1
Nichrome V (Ni 80%, Cr 20%)	+2.1
Karma (Ni 74%, Cr 20%, Al 3%, Fe 3%)	+2.0
Armour D (Fe 70%, Cr 20%, Al 10%)	+2.0
Monel (Ni 67%, Cu 33%)	+1.9
Manganin (Cu 84%, Mn 12%, Ni 4%)	+0.47
Nickel (Ni 100%)	-12.1

Table 1: Gauge factor of various metallic alloys. [50][52]

On the contrary, semiconductor exhibit a much more larger gauge factor than those of metallic strain gauges. In semiconductor strain gauges, the piezoresistive aspect denoted by the  $\left(\frac{d\rho}{\rho\varepsilon}\right)$  segment in Equation 56 plays a larger role in contributing to the total gauge factor value compared to its geometrical aspect. Similar to metal, the geometric effect in semiconductor strain gauges provide a gauge factor of approximately 1.4 to 2.0. However, the piezoresistive effect, such as those found in silicon and germanium semiconductor, could contribute up to 50 to 100 times larger than the geometric term [52]. Despite its benefit in producing larger resistance changes value, semiconductor strain gauges are known to exhibit a nonlinear behaviour, higher sensitivity to temperature, and more expensive than metallic strain gauges [51][50]. Therefore, in this research the use of metallic strain gauges is preferred. The following table exhibit the gauge factor or strain sensitivity of silicon and germanium semiconductor strain gauges [52].

Materials	Gauge Factor
Silicon type P	100 to 170
Silicon type N	-100 to -140
Germanium type P	102
Germanium type N	-150

Table 2: Gauge factor of semiconductor strain gauges [52]

Another aspect that needs to be considered in determining the proper metals to be used as the active element in the strain gauge is the suitability of the metal in terms of its mechanical properties with respect to the substrate it is on and the host gasket material. Measurements done in this master thesis involve a compression of the gasket which will deform the gasket and the strain gauge sensors inside it. Since the gasket used in this master thesis is a PDMS (Polydimethylsiloxane) silicone and it is classified as an elastomeric polymer, it will have a lower Young's modulus compared to the strain gauges, i.e. small stress will result in large strain deformation. Naturally, this will present as a dilemma for the metallic strain gauges embedded inside it regarding which metals with certain Young's modulus is going to be utilized.

Using metals with low Young's modulus, although still higher than the elastomeric polymer Young's modulus, will risk the metals to be over-expanded and damaged considering metals has lower maximum elongation than polymer. As an example, a 100nm Platinum thin films will break at strain of 0.0077 (nm/nm) at a fracture stress of 810 MPa [57] whereas Silicone structure could have a strain of 1 (mm/mm) at engineering stress of only ~4.15 MPa [58]. However, the benefit of this approach is that the metal will be more susceptible to strain changes affecting the gasket, therefore producing a more sensitive measurement regarding the deformation of the gasket. On the other hand, strain gauge with metals possessing a high Young's modulus will become more stable during integration and may prevent the risk of over-expansion. However, this will hinder its capability in measuring the strain deformation affecting the gasket host material, i.e. the strain gauge active element will be less sensitive to strain.

Several candidate metals have been selected to be utilized as the active element of the strain gauges. Selection is based on the requirements described above, the availability of the metals, and the suitable microsystem technology available to the deposition and patterning. Metals available to be selected as the active element of the strain gauges are platinum, gold, titanium, aluminium, and chromium. The thickness of the metals used is 100nm. This thickness is selected in order to possess a sufficiently high fracture stress and fracture strain while also does not contribute significantly in the reduction of the electrical resistance in order to obtain a readable resistance data, as shown in Equation 54 where  $A$  is related to the thickness of the active element. As an example, a 75nm thick platinum films will generate higher resistance compared to 100nm thick platinum films however it will have lower fracture strain between 0.0056 – 0.0074 compared to fracture strain between 0.0072 – 0.0077 possessed by the 100nm

thick platinum films [57]. Therefore, a 75nm thick platinum films will be more susceptible to damages caused by its host polymer gasket deformation.

Platinum is chosen as the first strain gauge in the nested strain gauge sensor due to the exceptional resistance both possess in oxidation and corrosion [59]. It is also important to note that platinum possess a gauge factor of 6 [50] which makes it sensitive to strain deformation. In addition, platinum can be easily deposited and structured using standard microsystem technologies. Other strain gauges are also fabricated as the second strain gauge using different metals available in the cleanroom such as gold, titanium, chromium, and aluminium. Both of these metals are also chosen due to the compatibility in the etching process available in the cleanroom.

In selecting the metal for contacts and the conducting path of the nested strain gauge, the most important feature that needs to be considered is minimizing the added resistance the contacts and conducting paths give toward the measured data. In addition, the conducting paths are also deformed caused by the deformation of the gasket, therefore it will also experience resistance changes. These resistance changes given by the conducting paths, although miniscule, is unwanted since the desired resistance changes are only those which are given by the strain gauges. Minimization of the added resistance could be achieved by means of depositing a significantly thicker film compared to the strain gauges. As previously mentioned, based on Equation 54, a thicker film represents a thicker cross section area ( $A$ ) which would reduce the resistance of that structure. Due to this reason, a 500nm thick film conductor and conducting path is used in most sensors presented in this thesis. It is also beneficial to select a metal with lower gauge factor and TCR compared to those used as the active element. This is done in order to reduce the change in resistance caused by strain and temperature affecting the conducting paths. The metal chosen to be the conducting path and contacts is Gold, due to its low gauge factor of  $\sim 2$  [60] and TCR of  $3.6 \times 10^{-3} K^{-1}$  [61]. Copper is also chosen as the second candidate for the conducting path and contacts thanks to its resiliency in preventing electromigration due to superior electrical and thermal conductivity while also possess high melting point [67][68].

### 3.1.2. Strain Gauge Substrate Material

Strain gauge substrate or the backing material of a strain gauge performs three different functions namely providing a support platform for the foil, facilitating the fixation of the strain gauges to a surface, and provide an electrical insulation between the metal foil and the test subject [50]. Therefore, a proper material selection for the substrate of a strain gauge is required in order to ensure the functionality of the nested strain gauge.

It can be deduced that the main goal of the backing material of the strain gauge is to protect the foils on top of it by means of limiting the amount of deformation to the foils caused by the polymer gasket the gauges is placed in. As mentioned previously, deformation limitation is required considering the metallic foil supported by the backing material possess lower fracture strain than the polymer gasket. This requirement could be achieved by utilizing a stable and



sturdy backing material which can be represented by the high Young's modulus. A high Young's modulus backing material ensures the strain gauge to be more resistant toward possible shear forces during the integration process into the gaskets [53].

Despite its resiliency toward possible shear forces, high Young's modulus of the substrate will limit the deformation of the substrate, therefore compromising the sensitivity of the strain measurement of the strain gauges. Therefore, a moderate Young's modulus is desired in order to obtain a sturdy backing material while also compliant enough to be deformable thus a sensitive strain gauges is acquired. The following graph depicts the elongation of the sensor with three different substrate materials with respect to the contact force applied to gasket. This graph is produced in a FEM simulation [53].

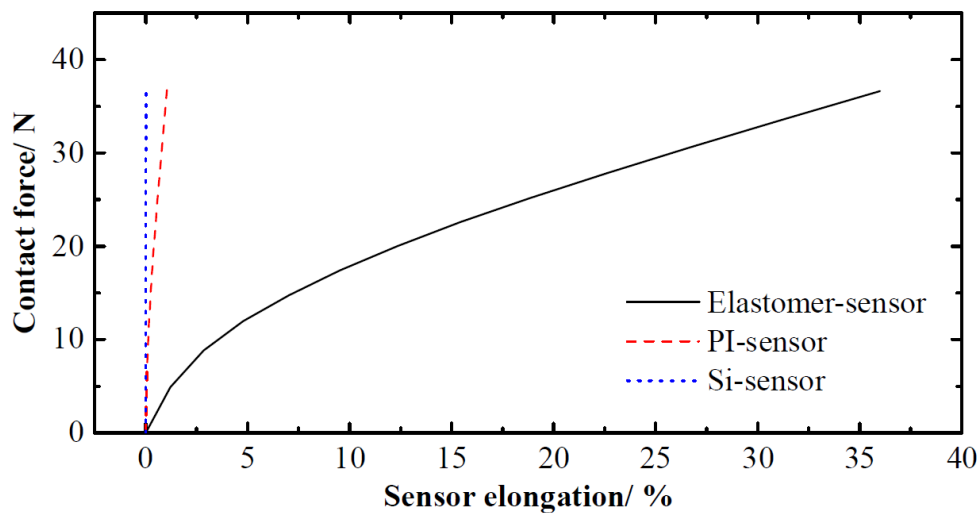


Figure 27: Sensor elongation with respect to contact force applied to the gasket for three different embedded substrate materials. [53]

As can be seen from Figure 27, sensor utilizing Polyimide (PI) as its substrate results in an elongation of approximately 1.1% compared to the other two extremes where the elastomer substrate which uses the same elastomer as the gasket results in the elongation of 35% and the silicon substrate results in the elongation of merely 0.02% [53]. As previously mentioned, using the elastomer substrate will damages the strain gauge foils on top of it due to its large elongation, whereas a very low sensitivity of the strain gauges towards strain will occur if silicon substrate utilized. Polyimide substrate on the other hand possess, although not as much, both benefits from the two extremes. It possesses the sturdy and stable behaviour of the silicon substrate whilst also possesses the stretchable characteristic of elastomer sensor. Due to these reasons, a polyimide substrate material is chosen in this master thesis.

It is also important to note that polyimide typically have a high coefficient of thermal expansion, i.e. approximately  $30-60 \times 10^{-6} \text{ K}^{-1}$  [62]. A large difference in the coefficient of thermal expansion, e.g. between the metals and the substrate, would introduce a shear stress effect between them. In addition, generally polyimide exhibit a shrinkage behaviour during its curing process or when exposed to elevated temperatures marked by the residual strains contained within polyimide film after the curing process [63]. Both of these effects would

introduce a large residual stress in the polyimide layer. Large residual stress typically results in the buckling, cracking, or even delamination of the films [64]. Since shrinkage is inevitable during the curing of the polyimide, in order to minimize the effect of residual stress, a polyimide with low thermal expansion coefficient is used. A polyimide precursor *U-Varnish-S* manufactured by *UBE Industries Ltd.* possess a low thermal expansion coefficient of  $3 \times 10^{-6} \text{ K}^{-1}$  for a polyimide with thickness of  $20 \mu\text{m}$  [65], as a result, this polyimide precursor is chosen.

### 3.2. Strain Gauge Fabrication

Before fabrication takes place, the design of the sensor needs to be conducted. The design is created in AutoCAD and will take into account the size of the sensor and also all the functional structures on it such as the strain gauge active elements, conducting paths, and contacts. The sensor is designed to be tapered at the top near the strain gauges. The tapered portion of the strain gauges is the part which will be embedded inside the polymer gasket. Tapering is done in order minimize the amount of metal contained inside the gasket which would acts as foreign bodies. The contacts are made to be broader than the rest of the conducting path in order to ease the manual adhesion with wires. These broad contacts will be placed sticking out of the gasket, therefore the metals on it does not pose as foreign bodies to the gasket. The sensor is surrounded by the void of polyimide (noted by the purple structures in Figure 28) with gaps between them. Since the whole sensor will be deposited and structured on top of the polyimide, the polyimide on the purple structures will be etched away using dry etch. Therefore, the only thing that connecting one sensor to the other is just the polyimide which remains between the gaps of the polyimide void structures. In this way, the singulation of the sensor can be done by cutting the remaining polyimide. Wide gaps of  $150 \mu\text{m}$  between the spacing of the polyimide void and nearest metal structure is made in order to give room during manual sensor singulation using scalpel.

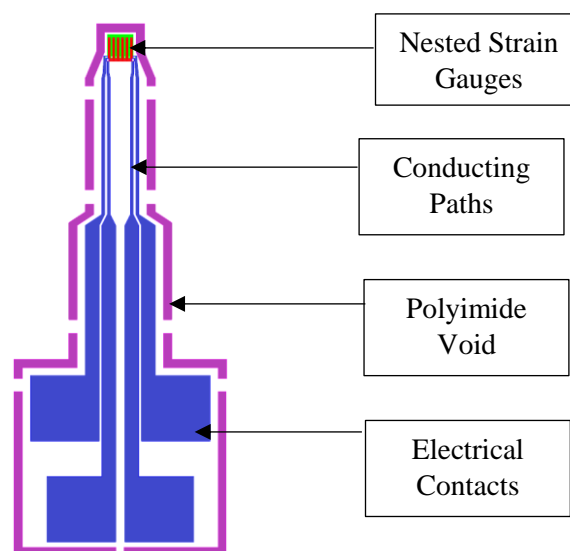


Figure 28: Sensor design made in AutoCAD

After the sensor design is created, each functional structure is allocated to different layer in the AutoCAD which will then be printed into separate lithography masks. The lithography masks are made from a soda lime glass with chromium film which could be structured by direct writing lithography.

After the lithography masks has been fabricated and all consideration regarding the material selection for the nested strain gauge has been applied, the next step is to fabricate the sensor. Fabrication begin by depositing the substrate material, i.e. polyimide film, on to the silicon wafer. The deposition is done by first installing the 100 mm silicon wafer on the spin coater, then the *U-Varnish-S*<sup>®</sup> polyimide precursor from *UBE Industries Ltd.* is poured atop the wafer. The spin coater will then spin to create a uniform layer with a thickness of 5  $\mu\text{m}$  above the wafer. Afterwards, the wafer with the deposited polyimide precursor is cured in a vacuum ( $10^{-3}$  mbar) hotplate to initiate the curing process. The polyimide deposition process can be seen in Figure 29.

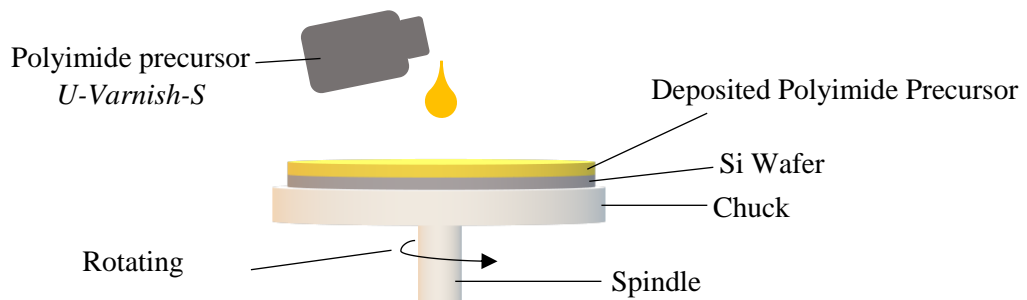


Figure 29: Polyimide deposition on a spin coater

The curing process is done in several steps due to the nature of polyimides which are generally insoluble in any solvents and degrade at high temperatures near their glass transition temperature ( $T_g$ ) [66]. The steps involved in the curing process include the evaporation of the solvents stage which occurs at temperatures less than  $150^\circ\text{C}$ , imidization stage at temperatures between  $150^\circ\text{C}$  and  $250^\circ\text{C}$ , and annealing stage at temperatures more than  $250^\circ\text{C}$ . The full history of the curing process can be observed in Figure 30. Each step is undertaken in order to increase the mechanical properties of the polyimide film and also increase its  $T_g$ . In the solvent evaporation stage, no imidization reaction occur, the mechanical properties and  $T_g$  is improved gradually due to evaporation of the solvent [66]. During imidization stage, the  $T_g$  increases as the imidization degree increases. Finally, during annealing at high temperatures ( $350^\circ\text{C}$  –  $400^\circ\text{C}$ ) the properties of the PI films is improved caused by further imidization and the development of the crystallized structure [66]. A desired 5  $\mu\text{m}$  thick polyimide film substrate is typically achievable due to the programmable rotational speed of the spin coater during the deposition of the polyimide precursor and also due to the weight loss occur during the curing process.

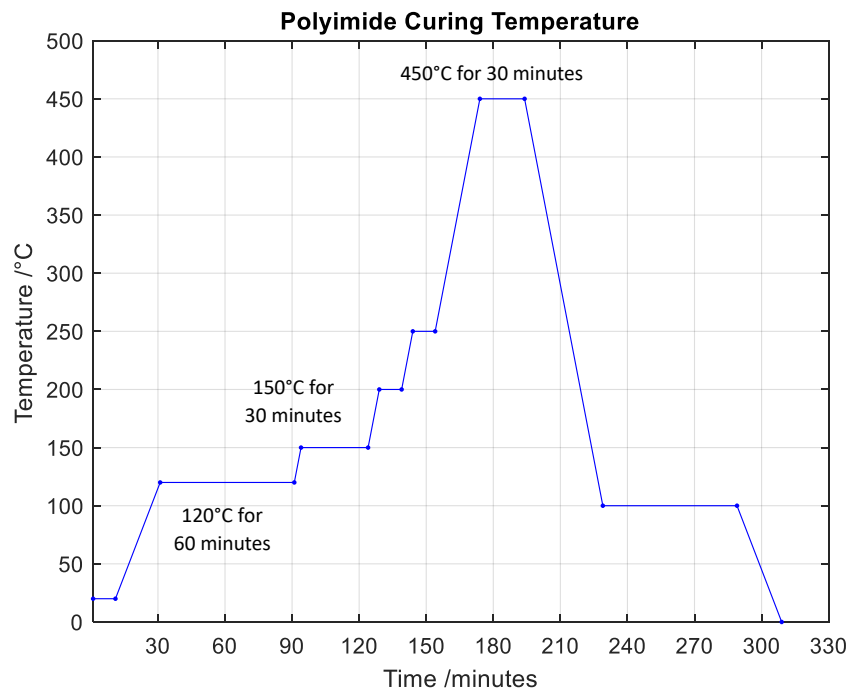


Figure 30: Polyimide Curing Temperature Profile

Once the polyimide film is ready, the first strain gauge metal is deposited. The deposition is done via physical vapor deposition (PVD) by magnetron sputtering. First, the wafer is inserted in a vacuum chamber inside the magnetron sputtering apparatus which also includes the target metal to be sputtered such as platinum, gold, titanium, copper, aluminium, and chromium. Afterwards, the sputtering program for each metal with its respective thickness is loaded. The program used includes the time and power of the sputtering as shown in Table 3. However, for the first strain gauges the metal used was platinum with a thickness of 100 nm.

Metals	100 nm		500 nm	
	Power	Time	Power	Time
Pt	200 W	68 s	-	-
Au	100 W	58 s	200 W	145 s
Ti	200 W	360 s	-	-
Cr	100 W	167 s	-	-
Cu	150 W	210 s	300 W	525 s
Al	250 W	500 s	-	-

Table 3: Sputtering power and time of different metals with different film thicknesses

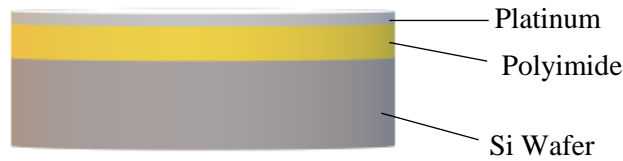


Figure 31: First strain gauge metal deposition

After the deposition of the metal, structuring the first strain gauge is done by wet chemistry. The first step in structuring the metal is done by depositing the photoresist which is done by spin-coating. A positive photoresist (AZ 1518® from *Micro Chemicals*) with a thickness of 1.8µm is used in the first strain gauge. The spin-coating program used to deposit 1.8 µm positive resist is presented in Table 4.

Positive photoresist AZ 1518, Thickness 1.8µm			
Step	Period [sec]	RPM [U/min]	Output
1	2	400	
2	8	400	3.5 mL AZ1518
3	10	400	
4	45	3800	
5	3	200	

Table 4: Positive photoresist deposition program

Following the resist spin-coating, the wafer is then pre-baked on a hotplate at 100°C for 2 minutes in order to evaporate the solvents in the resists, increases the adhesion of the resist, and improves the flatness of the surface. Afterwards, the photoresist is mounted in a mask aligner. In the mask aligner, the selected lithography mask which correlate to the desired first strain gauge structure is installed. Since this is the first metal to be structured, alignment is only done by making sure all the structure on the mask is fitted inside the wafer. After alignment is complete, the wafer along with the photoresist on top is exposed with UV light for 4 seconds. By doing so, the solubility of the positive photoresist which are not covered by the structure from the mask, i.e. exposed to UV light, will be altered, making it soluble in the developer AZ 726 MIF® from *Micro Chemicals* during development. The resist development is done by submerging the whole wafer in the AZ 726 MIF developer solution for 1 minute. Waves are also generated in the solution by means of moving the tray which contains the developer solution and the wafer by hand in order to accelerate the development process. Figure 32 shows the photoresist structuring process before and after exposure and development.

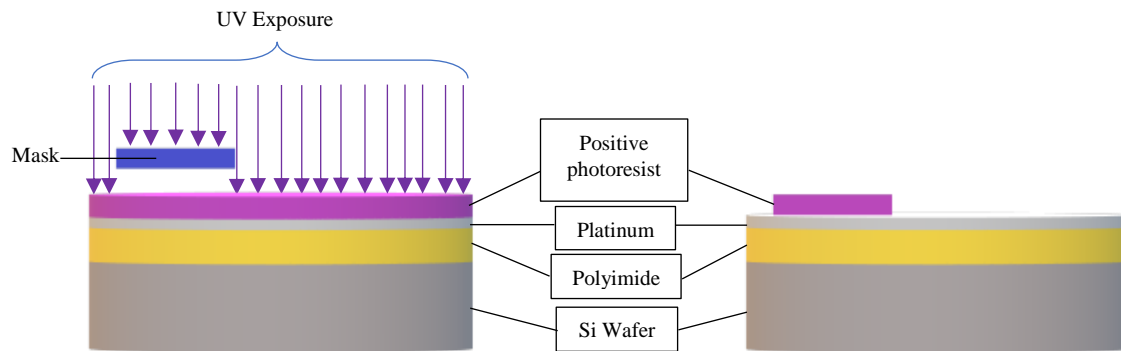


Figure 32: First strain gauge structuring by means of structuring the positive photoresist. Before exposure (left) and after exposure and development (right)

Following the structuring process of the photoresist, the next step is to etch away the metals which are not covered by the photoresist. Before etching is conducted, the platinum layer needs to be activated by argon plasma in order to accelerate the etching process. The parameter used in the argon plasma can be seen in Table 5. Platinum used as the first strain gauges can be etched by using a solution of heated and diluted aqua regia. The composition, temperature, and duration of the platinum etching can be observed in Table 6. It is important to structure platinum first before any other metals whenever platinum is used as one of the structures in the sensor. The reason behind this is because aqua regia will etch most metals present on the wafer. After the platinum has been structured, the remaining resist could be removed by submerging it in a 50°C AZ 100<sup>®</sup> resist removal solution from *Micro Chemicals* for 5 minutes

.Plasma	Power	Duration	Pressure
Ar <sup>+</sup>	50 W	5 minutes	120 mTorr

Table 5: Parameters of platinum layer activation by argon plasma

Metal	Etchant	Duration	Temperature
Pt	Aqua Regia (430 mL hydrochloric acid 37 wt%, 430 mL deionized water, 60 mL nitric acid 65-70 wt%)	3 minutes	82-84°C

Table 6: Platinum etchant composition, duration of etching, and etching temperature



Figure 33: Result after wet etching of the first strain gauge and resist removal

The deposition second metal to be used as the second strain gauge undergoes similar procedure as the first strain gauge. In the second strain gauge, several candidate metals are chosen as the active element material. These metals are gold, titanium, aluminium, and

chromium. All of these candidate materials are also deposited on to the wafer via PVD by magnetron sputtering. The thickness used in this strain gauge is similar to the first strain gauge which is 100 nm. The power and time of the magnetron sputtering can be referred to in Table 3.



Figure 34: Deposition of the second strain gauge metal on top of the already structured first strain gauge

Structuring the second strain gauge metal is also done by means of wet etching. The processes involved are almost identical to those in structuring the first strain gauge. First, the similar positive photo resist is deposited onto the wafer by spin-coating, followed by pre-bake on a hotplate at 100°C for 2 minutes. Afterwards, the wafer is mounted on a mask aligner with its own dedicated mask, i.e. the mask used for second strain gauges. Since the first strain gauges are already present on the wafer, alignment between the structures on the mask and on the wafer is required. The alignment is done by means of superimposing the alignment structure on the mask to the alignment structure on the wafer. The alignment structure used and the superimposing procedure are shown in Figure 35.

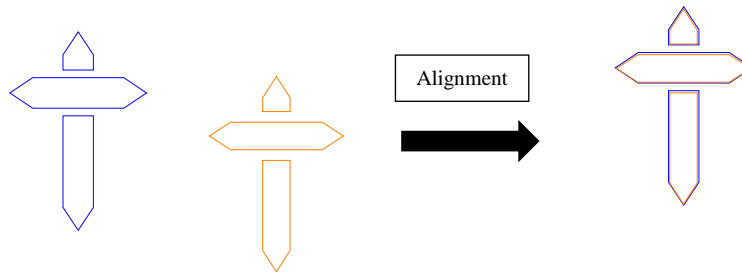


Figure 35: Structure used for alignment. Alignment structure on the wafer noted by the orange colour, alignment structure on mask noted by the blue colour. Before alignment (left) and after alignment (right)

After alignment is conducted, the wafer with the photoresist on top is exposed by UV light for 4 seconds, therefore altering the positive photoresist chemical properties to be soluble in the developer AZ 726 MIF in 1 minute at room temperature. Since the remaining positive photoresist remains on the desired location after the resist development, thus structuring the metal for the second strain gauges could be performed. In the case of second strain gauges different metals are used, therefore requiring various etchants in order to structure them. The etchants used for each metal is listed in Table 7. The resulting composition of the wafer before and after the exposure, resist development and etching are presented in Figure 36.



Metals	Etchant	Duration	Temperature
Au	Iodine solution (200 mL 0,5mol/L Iodine-potassium iodide solution, 100 mL 2-Propanol, 700 mL deionized water)	30 seconds	Room Temperature
Ti	Oxide Etch modified (Oxide Etch 7:1 modified, contains ammonium hydrogen difluoride and ammonium fluoride, from <i>Honeywell Specialty Chemicals</i> )	1 minute	20°C
Cr	Chrom Etch 3144 (contains perchloric ammonium citrate (IV) nitrate solution, from <i>Honeywell Specialty Chemicals</i> )	90 seconds	Room temperature
Al	Phosphoric acid solution (contains <i>Honeywell® Riedel de Haen®</i> and 2 mL Triton X-100® in 10 L solution)	1 minute	35°C

Table 7: Metals used as the second strain gauge and its respective etchants

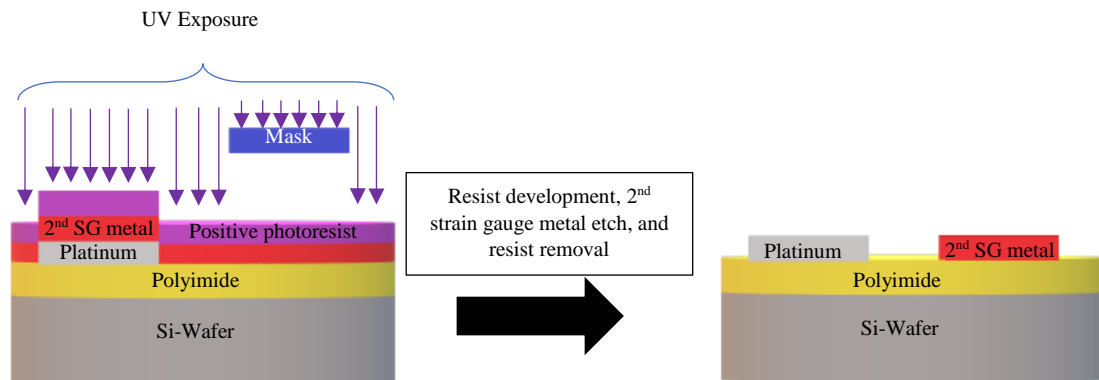


Figure 36: Second strain gauge structuring processes. Before exposure (left) and after exposure, development, metal etching, and resist removal (right)

In this master thesis two types of nested strain gauge sensors are fabricated on to a single wafer. The main difference between the two is the width of the active element. The first type is the nested strain gauge using strain gauges with a width of 10 nm for its active element whereas the second type of nested strain gauges utilizes strain gauges with a width of 20 nm for its active element, both are shown in Figure 37. The reason behind both of these designs is in order to assess the difference in the electrical resistance both gives during measurement when strains and temperatures are applied to them. However, both types endure the same fabrication process since the mask used already contain both types of sensors.

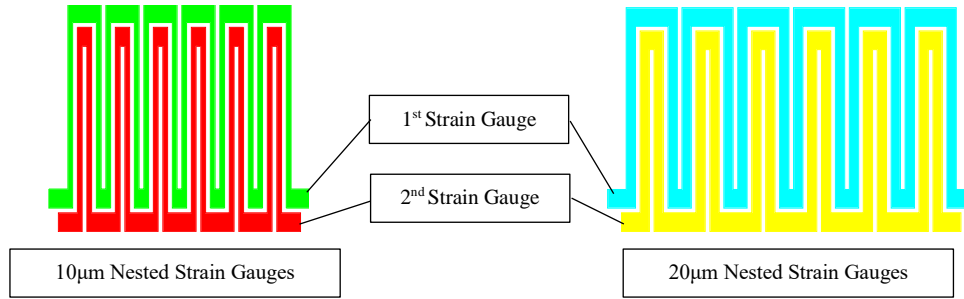


Figure 37: Two types of nested strain gauges with different widths

After the active element of the strain gauges has been fabricated, the next step to be conducted is to deposit and structure the metals to be used as the conducting paths and contacts. The structure of the conducting paths and contacts can be observed in Figure 38. As mentioned previously, two candidate metals have been chosen in order to do this role, namely copper and gold.

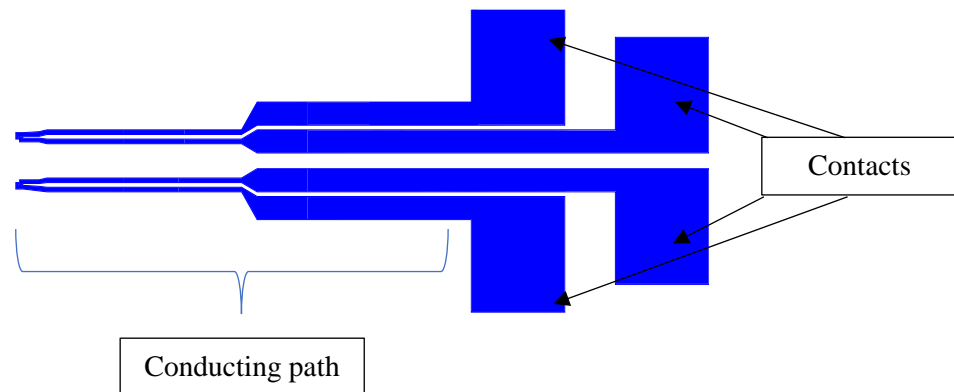


Figure 38: Conducting path and contacts of the nested strain gauge sensor structured using wet etching

In the first experiment copper is selected to be used as the conducting paths and contacts, accompanying the first strain gauge made of platinum and second strain gauge made of gold. Utilizing copper does not pose as a threat to the already existing structure on the wafer during its deposition and etching. A 500 nm thick copper film is deposited on to the wafer by magnetron sputtering to be used as the conducting paths and contacts, the power and time for the sputtering can be referred to in Table 3. Structuring copper could be achieved by normal wet chemistry, similar to those done in structuring the strain gauges. Firstly, the wafer with the copper on top of it is covered by photo resist AZ 1518 with a thickness of 1.8  $\mu\text{m}$  via spin coating, followed by pre-bake the resist on a hotplate. Afterwards, before exposure is conducted, alignment between the mask and the wafer is also performed in this case since both strain gauges structures are already present on the wafer. After exposure for 4 seconds, the resist will then be developed using the same developer AZ726 MIF and the same procedure. Finally, after the etching is performed, the etching of the remaining copper metals outside the intended structure is conducted. The etchants used for copper wet etching can be seen in Table 8. The result of the etching process is observed under a microscope, if the result is satisfactory then the removal of the remaining positive photoresist is done by submerging the wafer in 50°C

AZ100 resist removal for 15 minutes. The processes involved in structuring copper can be observed in Figure 39.

Metal	Etchant	Duration	Temperature
Cu	Alketch I + Alketch II (2:1 solution) from <i>Candor Chemie</i>	3 minutes	25°C

Table 8: Copper etchant composition, duration, and etching temperature

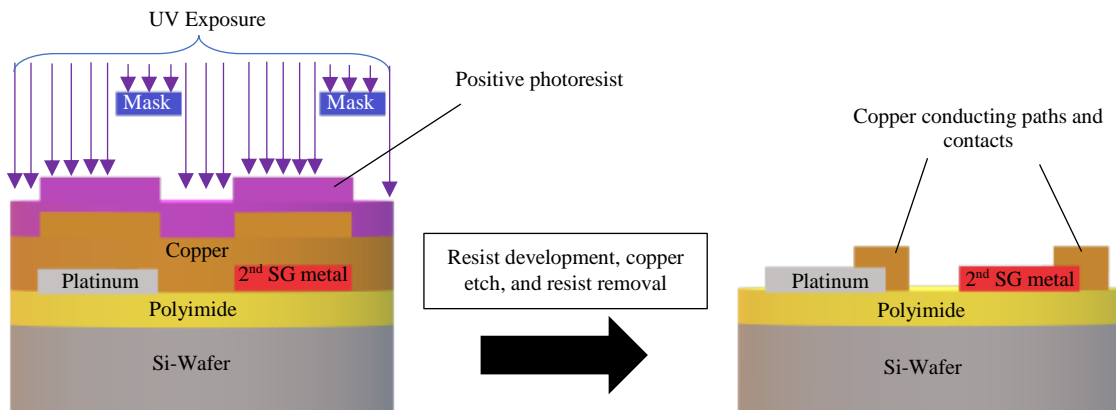


Figure 39: Copper conducting paths and contacts structuring process. Positive resist exposure (left) and after resist development, copper etching, and resist removal (right)

Gold conducting paths and contacts are also used in this research. Gold conducting paths and contacts used to accompany the nested strain gauges combination of Pt-Ti, Pt-Al, and Pt-Cr endure the same deposition and structuring processes as those endured by copper conducting paths and contacts. The only difference between them is the power and time of the sputtering, which could be referred to in Table 3, and the etchants in gold structuring which uses iodine solution. However, the same method could not be conducted when structuring the gold conducting paths and contacts is done on top of the already structured Pt-Au nested strain gauges. This is caused by the etchants used in structuring the gold conducting paths and contacts layer will inevitably attacks the gold strain gauges beneath it, therefore two structuring methods are chosen to mitigate this problem.

The first method chosen is to structure the gold conducting path and contacts by means of lift-off process. In lift-off process a negative photo resist nLOF 2070® from *MicroChemical* with a thickness of 7 µm is deposited on to the wafer and then distributed evenly by spin-coating consecutively after the structuring of the second strain gauges has been finished. The parameters used during the spin coating of the negative resist can be observed in Table 9.

Negative photoresist AZ nLoF 2070, thickness 7µ			
Step	Duration [sec]	RPM [U/min]	Output
0	0	0	6 mL nLOF 2070
1	15	700	
2	45	4500	
3	9	700	

Table 9: Negative photoresist spin coater program

After resist deposition, both the wafer and the negative resist on top of it is pre-baked on a hotplate at 100°C for 6 minutes. Afterwards, the wafer is mounted on a mask aligner where alignment is made between the mask and the wafer. The mask used is similar to the one used for structuring copper. After the structures are aligned, exposure is done on the mask aligner for 5 seconds. Following the exposure, the negative resist is post-baked on a hotplate at 110°C for 1 minute. The negative resist is then developed with AZ 726 MIF from *MicroChemicals* to remove the exposed negative resist. The development of the resist is conducted for 3-4 minutes in order to ensure undercutting in the negative resist. After the development of the resist is finished, gold metal with a thickness of 500 nm is deposited on to the wafer by magnetron sputtering (the power and the time for the sputtering can be refer to in Table 3). Removal of the negative resist with the unwanted gold metal on top of it is done by submerging the whole wafer in an NMP (N-Methyl-2-pyrrolidone) solution for 24 hours. Undercuts are desired in the resist during its development since it will ensure a pronounced gold structures during sputtering while also ease resist removal process due to the increased surface area in the undercuts which can be in contact with the NMP negative resist remover, as shown in Figure 40. The lift off procedure used in this method is presented in Figure 41.

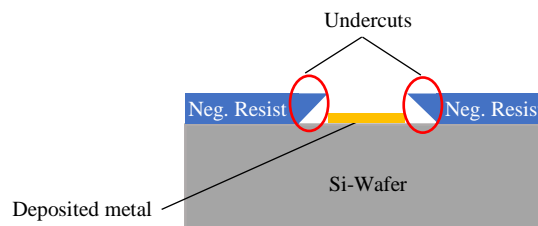


Figure 40: Undercuts in negative resist during development (noted by the red circles). Increased surface area caused by undercuts in the resist eases the resist removal process

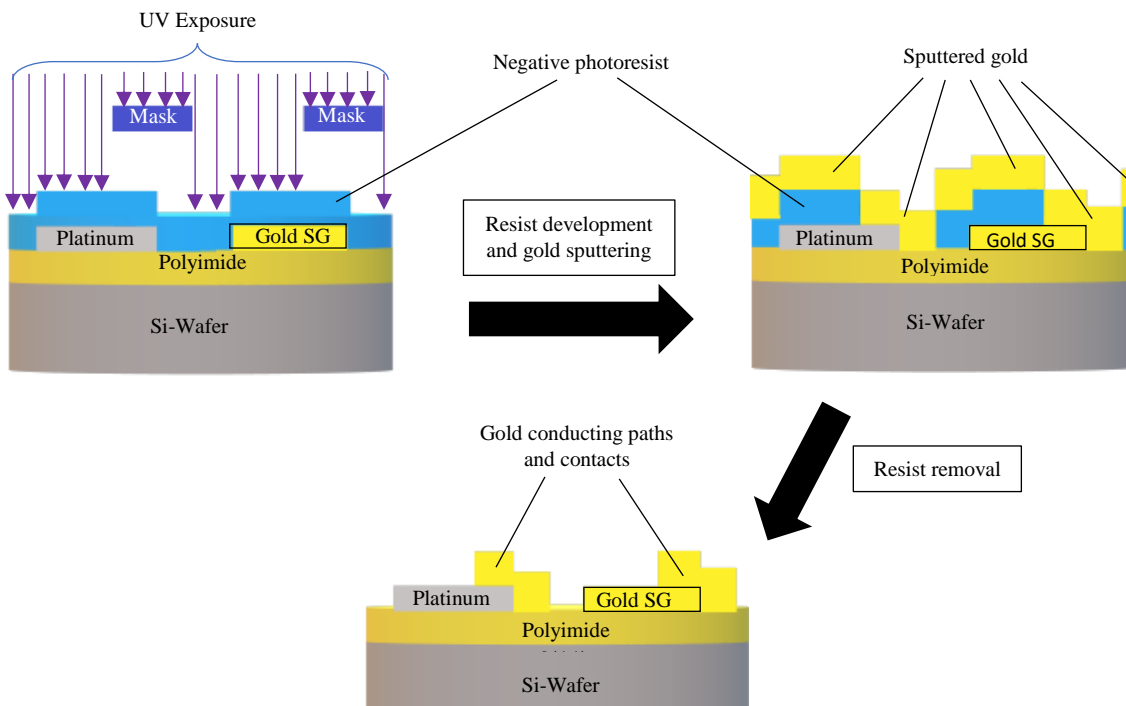


Figure 41: Gold conducting paths and contacts structuring by lift-off process. Negative resist exposure (top left), gold sputtering to be used as conducting paths and contacts (top right), negative resist removal in an NMP solution (bottom middle)

The second method chosen to structure the gold conducting paths and contacts is by means of direct writing lithography with positive photoresist. Direct writing lithography is chosen in this method since mask is not required in this process. In this method the gold sputtered to be used as the second strain gauges will also be utilized as the conducting paths and contacts. The drawback of this method is in terms of the thickness of the gold metal used as the conducting paths and contacts. Both of their thickness is only 100 nm since it corresponds to the thickness of the second strain gauges. Naturally, the thinner the thickness of the conducting paths, the higher the electrical resistance it will contribute to the measurement data from the active element of the nested strain gauges. Resolving this issue involves creating a new mask design which exhibits a wider conducting paths structure to balance out the reduction of the structure's thickness in order to suppress a substantial reduction in the cross section area of the conducting paths which is the main cause of the increase in the contribution of the electrical resistance of the measured data. The new mask designed is presented in Figure 42.

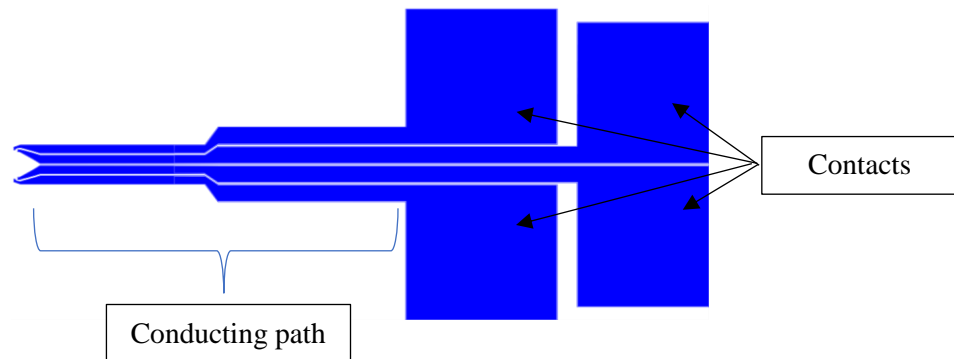


Figure 42: Conducting path and contacts of the nested strain gauge sensor structured using lift off

Structuring both the second strain gauges and the conducting paths along with the contacts are similar to normal gold wet etching process where positive photoresist AZ 1518 is spin coated on to the wafer, pre-baked on a hotplate at 100°C for 2 minutes, aligned and exposed by UV light while using the new mask design on a mask aligner, followed by the resist development in AZ 726 MIF for 1 minute, etching the unwanted gold outside the intended structures with iodine solution, and finally removing the resist by submerging the wafer in AZ 100 resist removal at 50°C for 5 minutes. The advantage of this method compared to the lift-off process is less time are required during the structuring process, where the whole wet etching process starting from metal deposition to structuring the metal could be concluded in 1 hour. The whole process involved in this method is shown in Figure 43.

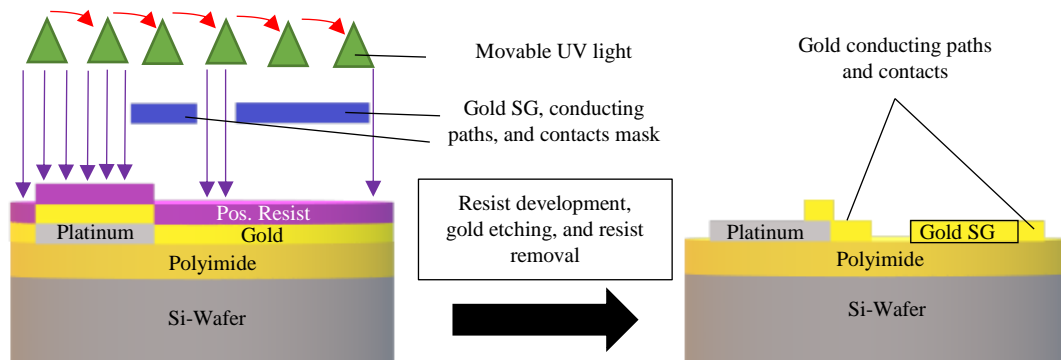


Figure 43: Gold conducting paths and contacts by means of direct writing lithography

After all metals making up the nested strain gauges has been deposited, the last step is the removal of the sensors from the wafer. The removal is done by structuring the polyimide which would cover all the structures on top of it first. In order to structure the polyimide, a positive resist AZ 9260 from *MicroChemicals* with a thickness of  $10\mu\text{m}$  is deposited on the wafer by spin-coating. After the resist is spin-coated on to the wafer, pre-bake of the resist is conducted for 3 minutes at  $110^\circ\text{C}$  before exposure. The pre-baking of this resist takes longer duration due to its higher thickness of  $10\mu\text{m}$  compared to the  $1,8\mu\text{m}$  thickness from the AZ 1518 positive photoresist. Before exposure, alignment between the mask and the wafer is required and it is done by using the same alignment structure shown in Figure 33 and the same alignment process involved. However, in this case, the structure used for polyimide etching has two varieties as shown in Figure 44 and each variety corresponds to separate masks. One version of the polyimide structure is used for the smaller sensor which contains thinner conducting paths and contacts width which are structured by mask lithography, the other version is used for the bigger sensor which contains wider conducting paths and contacts which are structured using direct writing lithography process.

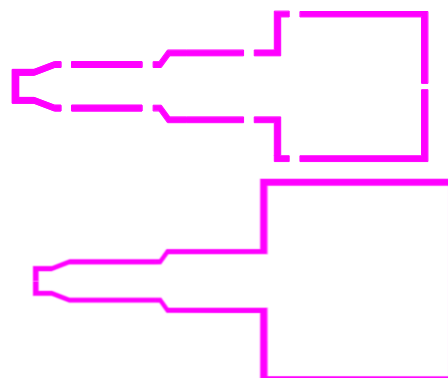


Figure 44: Polyimide etching structure. Structure used during masking lithography (top) and structure used during direct writing lithography (bottom)

Since thicker positive resists are used, exposure of these resists takes longer duration than the 1,8 $\mu$ m resist. After the mask and the wafer are aligned, the exposure with UV light is conducted for 120 seconds and this is the same for both mask varieties. Following exposure, the resist is then developed using the same developer AZ 726 MIF for 14 minutes. Structuring the polyimide is done by dry etching using inductively coupled plasma (ICP) in a vacuum chamber. The parameters used in this process is presented in Table 10. By doing so, the polyimide which are not covered by the photoresist will be dry etched. Therefore, gaps between the polyimide void structure which connecting each sensor on the wafer could be cut by hand using scalpel and the separated sensor could be peeled off from the wafer easily. The whole process of polyimide structuring from lithography exposure, polyimide etching, and sensor singulation is presented in Figure 45 and Figure 46.

Parameter	Quantities
Etching depth (corresponds to the thickness of the polyimide)	5 $\mu$ m
Etching duration	10 minutes
CF <sub>4</sub> flow	8 sccm
O <sub>2</sub> flow	40 sccm
Pressure	5 mTorr
Coil power	800 W
Temperature	10°C

Table 10: ICP parameters used for dry etching of polyimide

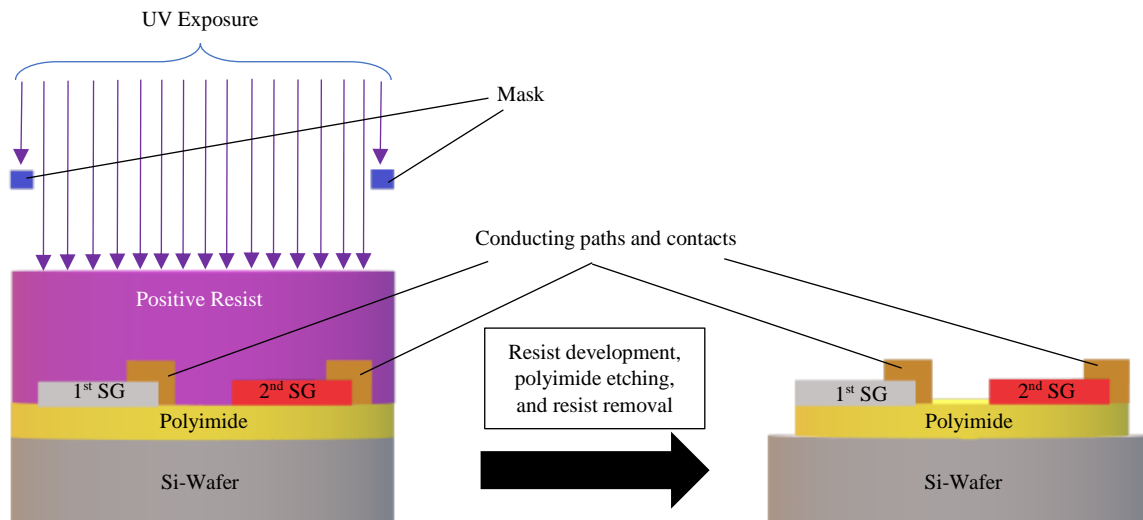


Figure 45: Polyimide structuring process by means of dry etching using Inductively Coupled Plasma (ICP). Before exposure (left) and after exposure, resist development, polyimide etching, and resist removal (right)



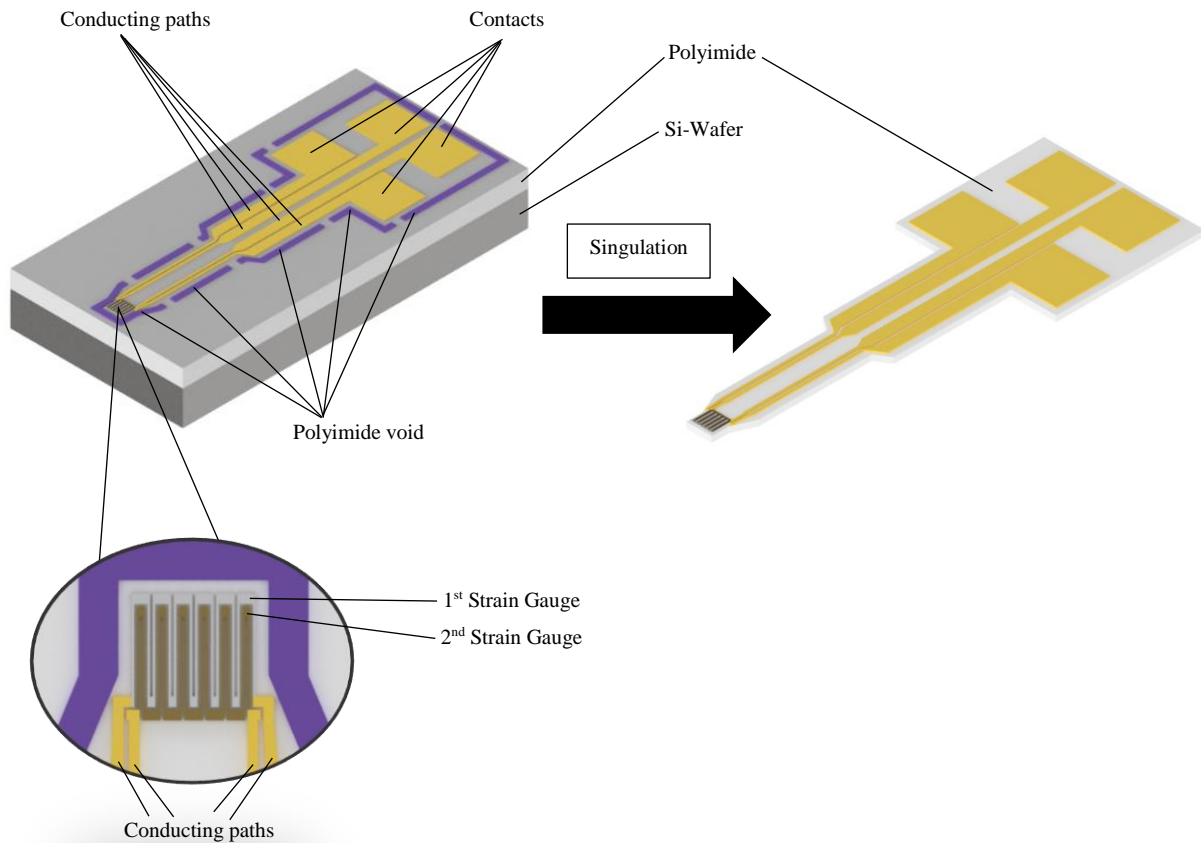


Figure 46: Sensor singulation process, before (left) and after singulation (right). Singulation is made by making an incision on the gaps between the polyimide voids followed by peeling off the sensor from the wafer.

### 3.3. Sensor Integration

After all the sensors has been fabricated, the next step involves integrating the sensor into the gasket in order to monitor the condition of the gasket by means of measuring its strain deformation and the temperature it is subjected to. As mentioned previously, the material chosen as the gasket in this master thesis is silicone PDMS (Polydimethylsiloxane). PDMS silicone gaskets are widely used in various applications such as in electrical application as insulators, aerospace application as seals, and the most prominent one which differ the use of silicone gasket from other type of gasket are those in the medical field and food processing where high biocompatibility possessed by silicone gasket is required. PDMS silicone gasket is chosen as the gasket material in this research due to the simplicity in its manufacturing process and possesses a quite similar elastomeric behaviour to most common rubber gasket, where large elongation is present due to the subjected forces acting upon it. Therefore, PDMS silicone is believed to be able to emulate this behaviour. Large elongation deformation caused by the low Young's modulus PDMS silicone gasket has, will introduce strains inside the gasket. Moreover, as the gasket ages as mentioned previously, these strains will vary overtime. These overall strain behaviour of the gasket over a period of time, is one of the main subjects of research in this master thesis. Integrating the sensor inside the gasket enables the possibility to

assess these behaviours, therefore unlocking the knowledge regarding the condition of the gasket.

Fabricating the PDMS silicone gasket involves mixing two components together, namely the silicone precursor and the curing agent. The silicone components used are SYLGARD® 184 silicone precursor and curing agent from DOWSIL™. The composition used is 10:1 silicone precursor and curing agent respectively. Mixing the silicone precursor and curing agent could be done manually by hand with a stirrer. Following the mixing process, the next step involves removing any air bubbles that may be introduced in the mixture. Air bubbles might compromise the mechanical integrity of the silicone gasket since it will introduce holes or pores in the system, making the deformation to be non-uniform throughout the whole system. Removal of the air bubbles could be done simply by placing the mixture in a vacuum chamber for 15 minutes which would absorb the bubbles out of the mixture. After the mixture is free from the bubbles, it is then poured into the gasket mould shown in Figure 47. The mould has a bracket which is utilized to fix the strain gauges from the sensor to be positioned exactly in the middle cross section of the gasket both horizontally and vertically. Ensuring the position of the strain gauges to be precisely in the middle cross section of the gasket is necessary due to the stress distribution affecting the gasket as simulated by Schotzko [53] and as shown in Figure 48.

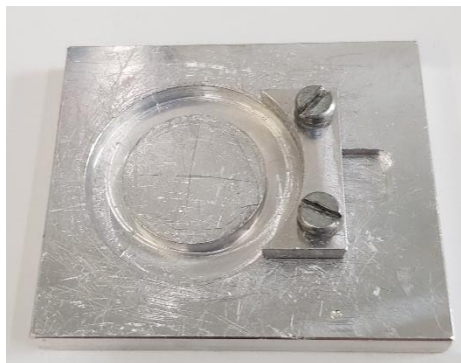


Figure 47: Silicone mould used to fabricate the silicone gaskets

As can be observed in Figure 48, positioning the sensor in location B will have an effect of the asymmetrical stress endured by the strain gauges, where part of the sensor facing the centre of the O-ring cord experienced the highest stress. As a result, sensor placed in this location will have the lowest amount of elongation [53]. On the other hand, sensor placed in location A is bent due to the forces applied from the top contact plates. Bending may be beneficial when measuring strain is involved since it will elongate the sensor further during initial compression by the top plate, as shown in the top right graph of Figure 48. However, this could lead to problem of, for example, plastically deformed the strain gauges vertically which could lead to the breakage of the sensor. Other example might be when the sensor is subjected to heat, due to the low thermal conductivity of the silicone O-ring gasket, the temperature measured by the sensor does not represent the temperature experienced by the whole gasket, i.e. it is only the temperature endured by one side of the gasket. Moreover, if the sensor is already vertically plastically deformed, further temperature gradient is experienced

by the strain gauges of the sensor since part of the strain gauge which is closer to the surface of the gasket is more sensitive to temperature. However, whether this effect is negligible or not due to the size of the strain gauges compared to the gasket, further testing is required. Therefore, location C is chosen to be the proper position for the sensor to be integrated to in order to avoid these problems.

After the silicone mixture is poured into the mould, it is then cured in order to stiffen the mould. Curing of the PDMS silicone could be achieved in room temperature as soon as the curing agent is introduced into the silicone precursor due to the cross link formed between the siloxane oligomers and PDMS chain. However, placing the mixture in an oven at 100°C for 20 minutes could accelerate this process. Precaution needs to be taken as to avoid placing the silicone mould in the oven for extended period of time which could formed more crosslink which eventually further stiffing the silicone gasket. Following the curing process the silicone O-ring gasket is cooled off for 15 minutes before removing it from the mould.

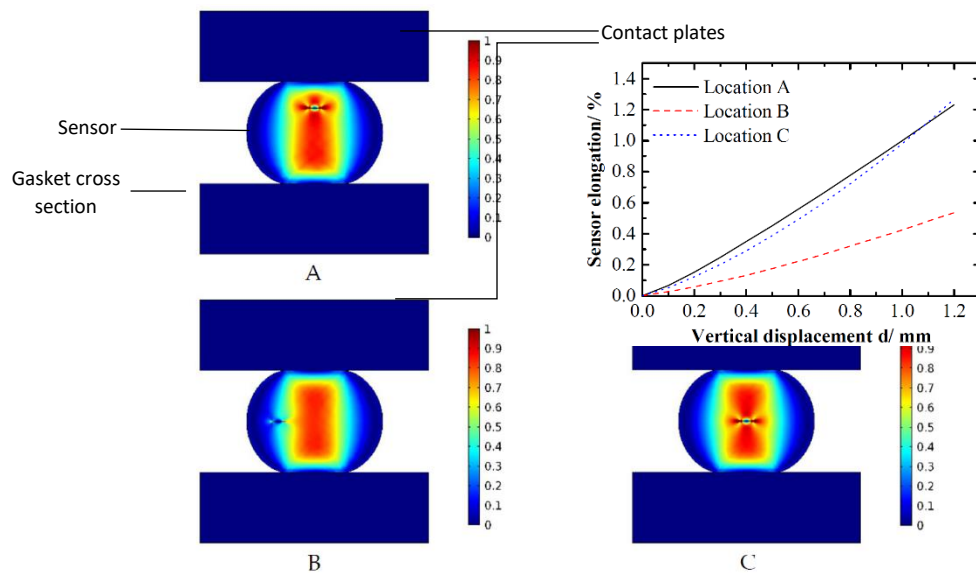


Figure 48: Von Mises stress distribution (N/mm<sup>2</sup>) of the O-ring gasket with integrated sensor in various locations. [53]



Figure 49: Integrated sensor in gasket

### 3.4. Wire Bonding

The last step in the whole process in creating the test specimens is to wire the sensors in order to obtain the measurement data. Wiring is done on the contacts of the sensor by utilizing an isotropic conductive adhesive Elecolit® 414 from Panacol™. This adhesive is based on polyester resin and contains flakes of silver in the size of 16  $\mu\text{m}$ , since the contacts area are 1.5  $\text{mm}^2$  and the closest gap between the conducting path near the contacts is 50  $\mu\text{m}$ . Therefore, the properties possessed by this adhesive is sufficient to minimize the possibility of shorting two adjacent contacts.

The wire bonding process is done by firstly combining copper wire with the contacts of the sensor with conductive adhesive. Precautions need to be taken in terms of selecting the size of the copper wire. A thick and heavy copper wire, noted by the large diameter will posed as a threat to the structural integrity of the sensor. Since the contacts of the sensor is sticking out of the gasket with no other support other than its polyimide substrate, a heavy wire will possibly damage the sensor during handling. Therefore, in this experiment the diameter of the copper wire chosen is less than 0.15 mm. After the contacts and the wire is combined, the sensor is heated on a hotplate at 70°C for 16 minutes, as required by the datasheet of the adhesive [70], in order to cure the adhesive glue.

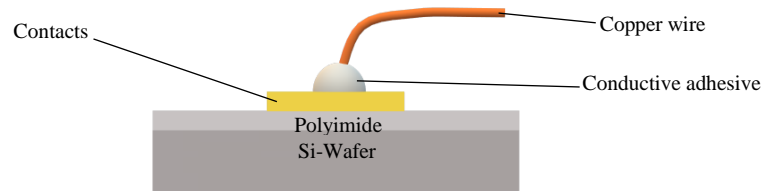


Figure 50: Wire bonding on top of the contacts of the sensor

### 3.5. Strain Gauge Characterization

The data obtained during the measurement regarding the condition of the gasket in its application in the gasket will be in form of changes in the electrical resistance of the strain gauges. As previously mentioned in Chapter 2, these changes in the electrical resistance of the strain gauges will be heavily contributed by two variables, namely the strain deformation the nested strain gauges endured and the temperature affecting them.

In order to precisely assessed the effect of these two variables to the changes in the electrical resistance of each strain gauge in the sensor, a characterization of these strain gauges is required. The characterization is done in order to obtain two coefficients which both will dictate the amount of electrical resistance changes to the strain gauges. These coefficients are the gauge factor ( $G_f$ ) and the thermal coefficient of resistance (TCR), which can be referred to in Equation 52 and Equation 73 respectively.

### 3.5.1. Gauge Factor ( $G_f$ ) Characterization

Characterizing the gauge factor of the strain gauges is done by means of applying a known strain deformation to the test specimen which contains the strain gauges on top of it, measure the change in the electrical resistance exhibited by the sensor caused by the strain deformation, and afterwards uses Equation 52 in order to obtain the gauge factor of the strain gauge. Applying the strain deformation is done by subjecting the test specimen to a tensile test as shown in Figure 51.

The test specimen used is a “dog bone” shaped steel bar. Fixating the sensor on top of the test specimen is done by firstly applying an epoxy adhesive (UHU plus endfest®) and afterwards placing the sensor on top of the adhesive. After the sensor is placed, the test specimen is placed on a hotplate to accelerate the curing process of the adhesive. Afterwards, the test specimen is mounted on to the fixator on the tensile test apparatus.

In tensile test, the test specimen is pulled with a force of 10 N/s until it reaches the maximum pull force of 1000 N in 100 seconds. The amount of strain applied to the specimen is measured manually by subtracting the final length of the test specimen after the test has reached its maximum force with its initial length before any force is applied. Real time strain could also be measured by the tensile test apparatus which could measure the displacement of its arm during the test. The electrical resistance of the sensors attached to the test specimen is also measured using a multimeter. Therefore, changes in the electrical resistance during any strain deformation occur throughout the period of the testing could be obtained.

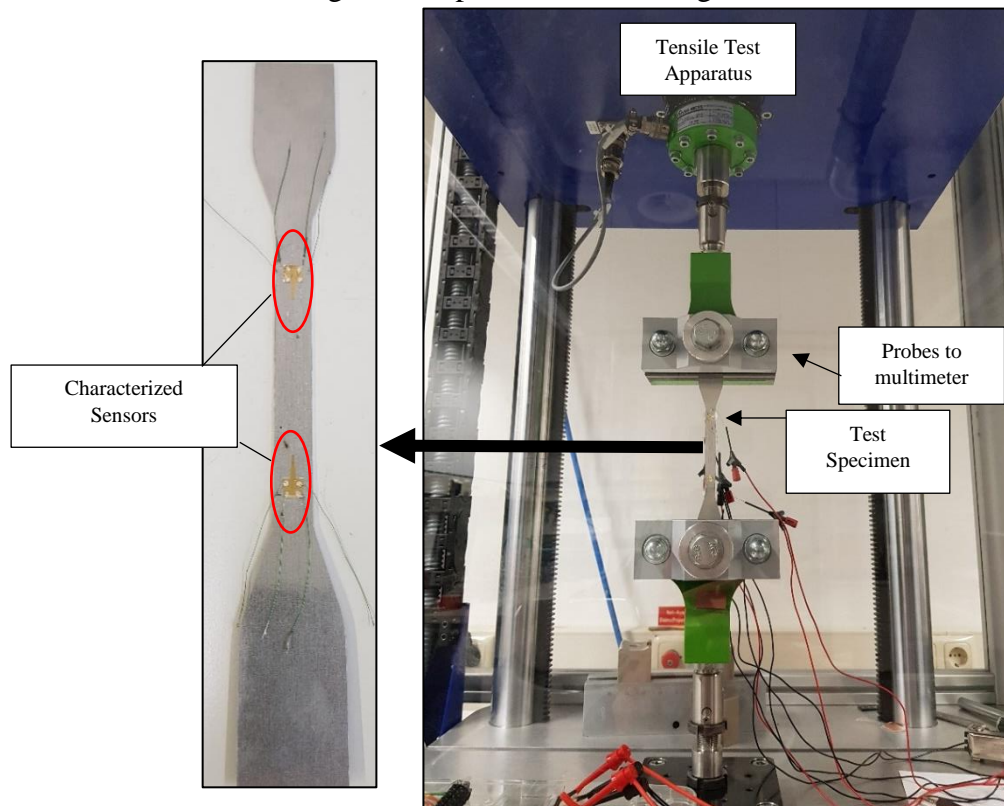


Figure 51: Gauge Factor Characterization Apparatus (right) and the test specimen (left).



### 3.5.2 Temperature Coefficient of Resistance (TCR) Characterization

Similar to characterizing the gauge factor of the strain gauges, characterizing the TCR is done by making sure that the changes in electrical resistance of the sensor is only affected by one variable, which in this case is the temperature. The test procedure is done placing the fabricated sensors on top of a hotplate and apply heat to them from 24 °C to 150 °C in ramps of 8°C. Since temperature changes does occur in the strain gauges, changes in electrical resistance of the strain gauges is expected. Determining the TCR is done by correlating the changes in temperatures with the changes in electrical resistance referring to Equation 73. The electrical resistance shown by the strain gauges at room temperature during the experiment (24°C) will be regarded as the reference resistance ( $R_{ref}$ ) of the strain gauges, therefore electrical resistance at temperature higher will be used to calculate the  $\Delta R$ .

The apparatus used in this characterization process is shown in Figure 52. Beside the sensors which are being characterized, a Pt 100 2-wire resistance temperature device (RTD) sensor is also placed on top of the hotplate. This temperature sensor is used to precisely measure the temperature on top of the hotplate in order to accurately correlate the temperature of the hotplate to the actual electrical resistance measurement of the sensors. Both electrical resistance exhibited by the tested sensors and the temperature readings exhibited by the RTD sensor will be measured by Keithley® 2100 multimeter. Polyimide adhesive tapes are used to stick the sensor on the hotplate, since the test will reach temperatures where most conventional adhesive tapes melt.

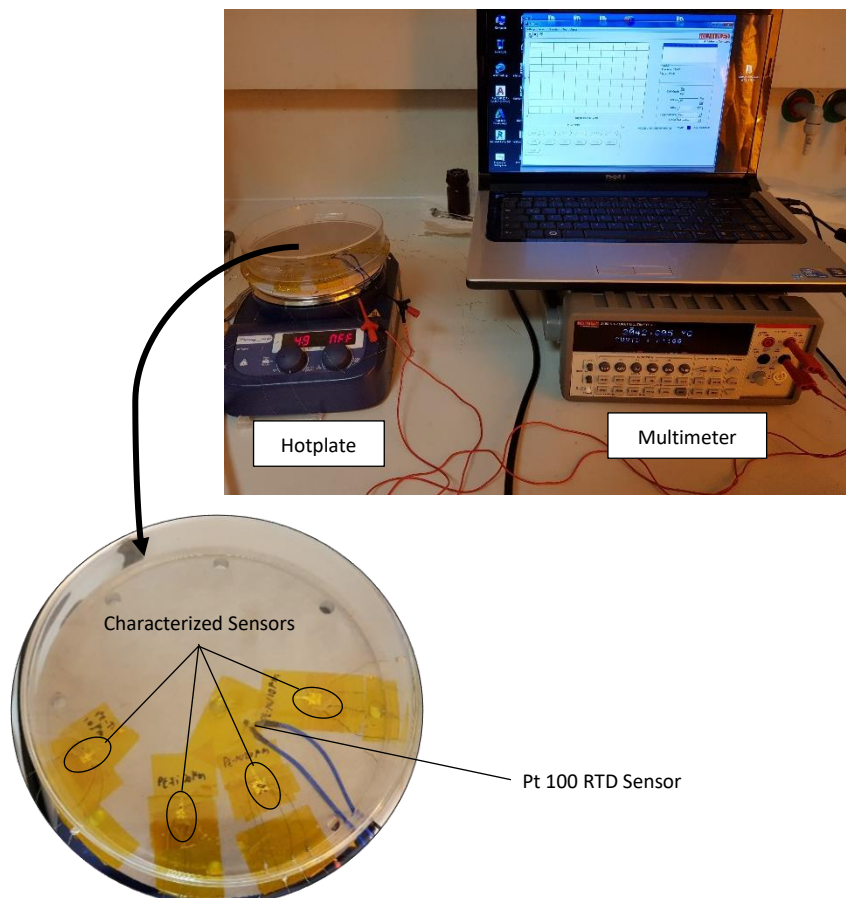


Figure 52: Temperature Coefficient of Resistance Characterization Apparatus

### 3.7. Gasket Condition Monitoring

In the first experiment, monitoring the condition of the gasket during its application is performed. The monitoring includes measuring the overall behaviour of the gasket by means of detecting the strain deformation it has and the temperature affecting it during the entirety of its application. Monitoring the condition of the gasket also involves performing an ageing test to the gasket. As mentioned previously, a gasket is considered to be aged whenever there is an irreversible deformation occur and it could be quantified by the compression set the gasket possesses after the simulated ageing process has completed.

Referring to the standard enacted by ISO 815 [28] regarding the determination of compression set at ambient, elevated or low temperatures, the compression set measurement in this master thesis is done by placing the fabricated gasket with the integrated sensor between two compression plates. Compression is done by means of tightening the bolt on the compression plates. Spacers are also used on this measurement to ensure that the compression done by the compression plates is approximately 25% of the original thickness of the gasket. Since the thickness of the gasket is approximately 3 mm, therefore spacers with thickness of approximately 2.25 mm is selected. During this measurement, strain deformation occurs in the gasket is detected by the sensor embedded inside. Therefore, providing an insight regarding the deformation behaviour of the gasket during the whole ageing process which includes compression, stress relaxation of the gasket, and decompression.

Measurement of the temperature affecting the gasket during ageing is also conducted by means of placing the compressed gasket between the compression plates inside an oven at 70°C. The purpose of this measurement is to prove that temperature measurement using two strain gauges placed in a nested configuration is possible. Other importance to measure the temperature affecting the gasket is in order to obtain a precise strain deformation measurement exhibited by the gasket, since resistance changes in the strain gauges is affected by both strain deformation and temperature affecting the gasket. If this measurement is achieved, a simultaneous measurement of strain and temperature during its application can be acquired. The electrical resistance produced by the sensor during measurement is monitored by a multi meter (Keithley DMM6500®) which is connected to a computer to be logged and stored.

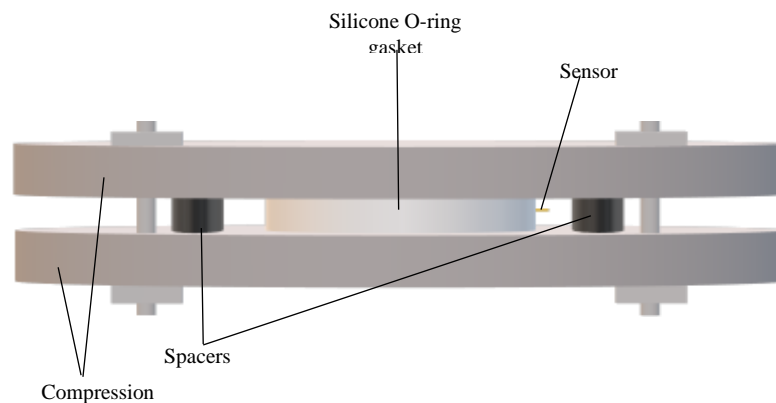


Figure 53: Compression plates configuration to be used as gasket ageing measurement



# CHAPTER 4

## Results and Analysis

### 4.1. Fabrication Results

In this subchapter, the results of each fabrication done in this research which involves various metal combination candidates to be used in the nested strain gauges and various processing methods are discussed. The metal combination candidates in this research are as follows:

1. Platinum (Pt) & Gold (Au) 10 $\mu$ m width strain gauges with Copper (Cu) contacts.
2. Platinum (Pt) & Gold (Au) 20 $\mu$ m width strain gauges with Copper (Cu) contacts.
3. Platinum (Pt) & Gold (Au) 10 $\mu$ m width strain gauges with Gold (Au) contacts.
4. Platinum (Pt) & Gold (Au) 20 $\mu$ m width strain gauges with Gold (Au) contacts.
5. Platinum (Pt) & Chromium (Cr) 10 $\mu$ m width strain gauges with Gold (Au) contacts.
6. Platinum (Pt) & Chromium (Cr) 20 $\mu$ m width strain gauges with Gold (Au) contacts.
7. Platinum (Pt) & Aluminium (Al) 10 $\mu$ m width strain gauges with Gold (Au) contacts.
8. Platinum (Pt) & Aluminium (Al) 10 $\mu$ m width strain gauges with Gold (Au) contacts.
9. Platinum (Pt) & Titanium (Ti) 10 $\mu$ m width strain gauges with Gold (Au) contacts.
10. Platinum (Pt) & Titanium (Ti) 20 $\mu$ m width strain gauges with Gold (Au) contacts.

However, only the sensors fabricated using the metal combination of platinum and gold with gold contacts structured using wet etching and direct writing lithography are proven to be functional, i.e. exhibit changes in electrical resistance due to changes in both temperature and strain. This subchapter is dedicated to explain the successful fabricated sensor while also delve deeper into the probable causes of failure in other metal combinations of the sensors.

#### 4.1.1. Platinum (Pt) & Gold (Au) strain gauges with Copper (Cu) contacts

Fabrication of platinum and gold strain gauges with copper contacts has been performed. Structuring processes conducted in this experiment results in a distinct structure fabricated for the strain gauges and the conducting paths as shown in Figure 54.

However, despite the perfect structure fabricated in this process, it was found that sensors fabricated using these metals tend to curl up after singulation. Curl observed in these sensors is caused by the intrinsic compressive stress occur in the contacts of the sensor where the thickness is five times thicker (500 nm) than the thickness for the metals in the strain gauges (100nm). Compressive stresses in the contacts are believed to be generated due to the atomic peening occur on the copper contacts surface during sputter deposition [73].

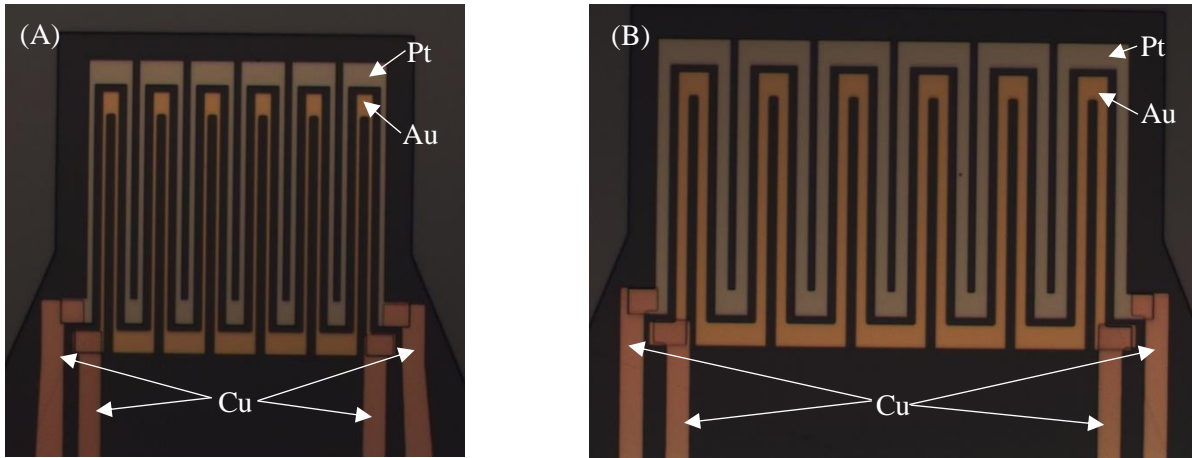


Figure 54: Fabricated platinum and gold strain gauges with copper contacts. Figure (a) represents strain gauges with 10  $\mu\text{m}$  width and Figure (b) represents strain gauges with 20  $\mu\text{m}$  width.

Energetic ions bombarding the bulk copper contact film during magnetron sputtering generates plastic deformation in form of a dimple on the top layer of the film. These dimples result in material displacement on the top layer which is resisted by the atoms below it. Resistance is done by creating compressive lateral stress that would restore the stretched material to return to its original shape as shown in Figure 55.

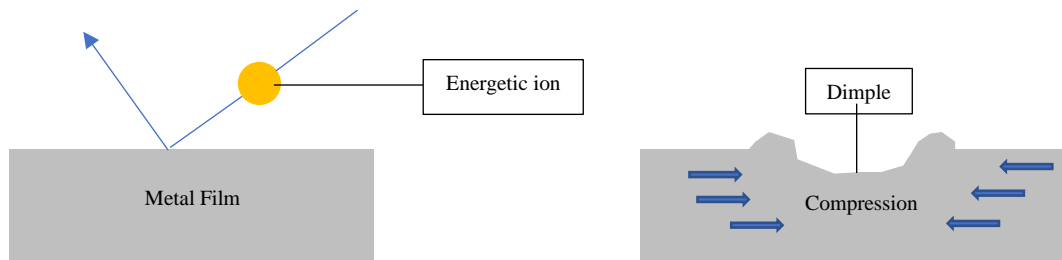


Figure 55: Dimple generated on the metallic film during sputtering

Since plastic deformation is involved during atomic peening of a film, the yield strength of the metal will inevitably affect the dimples created on the film during ion bombardment. It is believed that since thin film copper possessed lower yield strength (150.1 Mpa) than gold (240 Mpa) [74][75], higher concentration and area of dimples on the film generated by ion bombardment during sputtering occur. Due to this reason, the compressive stress occur in copper is higher than gold. Therefore, during the singulation of the sensor, these compressive stresses are able to curl the sensor more violently in copper contacts than in gold contacts. Curling will render the sensor to be unusable to be integrated in gasket since it will displace the position of the strain gauges inside the gasket during casting. Displacement of the strain gauges inside the gasket will affect the amount of strain and temperature affecting the gasket as mention in Section 3.3.

#### 4.1.2. Platinum (Pt) & Gold (Au) strain gauges with Gold (Au) contacts

Fabrication of the platinum and gold strain gauges with gold contacts and conducting paths is done by two different structuring methods, namely mask lithography with lift-off process and direct writing lithography with wet etching. The major difference between them during this research is regarding the thickness of gold contacts and conducting paths fabricated. Structuring by means of lift-off enables the opportunity to obtain different metal thickness between the gold contacts (500 nm) and the gold strain gauge (100 nm), whereas structuring by means of direct writing lithography and wet etching forces the thickness between the gold strain gauge and gold contacts to be the same at 100 nm thickness. Typical mask lithography with wet etching structuring process could not be conducted in this research due to the unavailability of the mask containing both the strain gauge and contacts.

The mask used in mask lithography and lift-off structuring process is shown in Figure 26. Problems arise during the removal of the negative resist, i.e. lift-off of the unwanted metal. Gold metals deposited outside the sensor are easily lifted by the negative resist remover (NMP). However, gold metals which are deposited between the structures such as those located between the contacts and conducting paths which are only 50  $\mu\text{m}$  apart are not easily peeled despite it has already been submerged in NMP for 14 days, as shown in Figure 56. Accelerating the removal of the resist by mechanical agitation has also been performed, it is done by means of placing the wafer containing the sensors in an ultrasonic bath containing deionized water. However, gold metals between the conducting paths, although slightly reduced, still remains and the mechanical agitation only damages the polyimide layer beneath it due to stresses applied during ultrasonic bath.

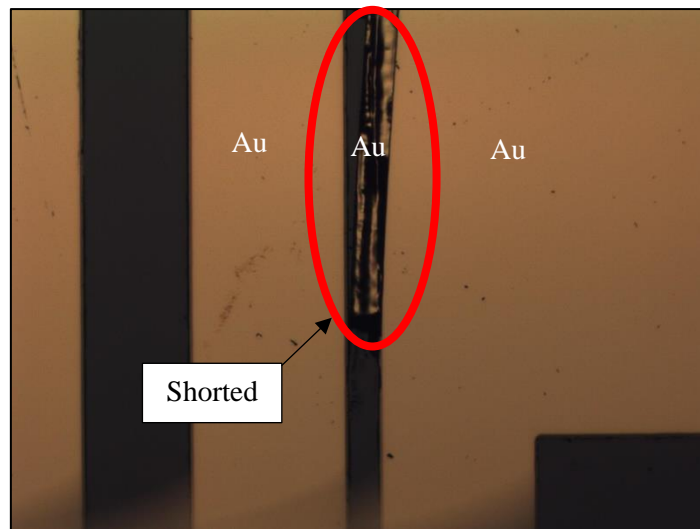


Figure 56: Shortages in the conducting paths for Pt & Au nested strain gauges structured using lift-off

It can be concluded that the problem during the removal of the resist is due to the lack of contact area between the resist remover NMP with the negative resist, since the resist are trapped between the two gold structures with only small distance between each other. Moreover, it is also possible that during the deposition of the gold metals after the development of the negative resist, a non-directional deposition during sputtering as shown in Figure 57 (a)

and noted by the red arrows, would cause the gold metal atoms to stick to the side walls of the negative resist, which could short circuited the two conducting paths, i.e. completely enveloping the negative resist as shown in Figure 57 (b). Therefore, there will be no contact between NMP and the resist in the sidewalls, the only possible point of attack for the NMP to remove the resist is only from the front end or back end of the negative resist as shown in Figure 57 (c). The possible solution to mitigate this problem is by designing the conducting path with wider gaps as those designed in this experiment. Wider gaps will minimize the possibility of gold atoms to stick to the sidewalls of the negative resist, i.e. more tolerable to non-directional sputtering.

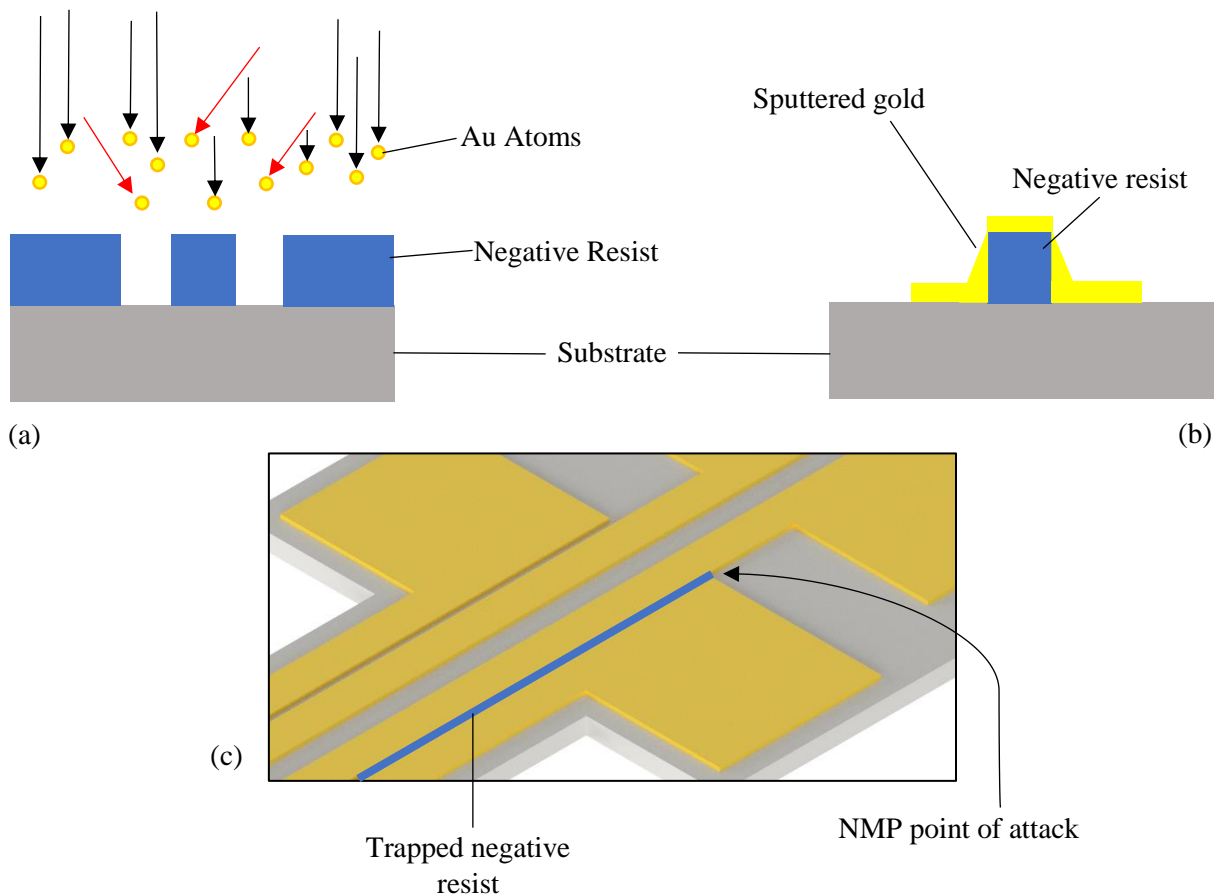


Figure 57: Explanation regarding the problem during negative resist removal. Figure (a) represents the non-directional sputtering during gold metal deposition after negative resist development, Figure (b) represents the gold metals sticking to the sidewalls of the negative resist, Figure (c) represents the point of attack of the NMP negative resist remover

Other method implemented in this research is by direct writing lithography with wet-etching. As mentioned in Chapter 3, this method is used to structure both the strain gauge and the conducting paths simultaneously from the same gold layer deposited on the wafer. Resulting in the same thickness produced between the strain gauge and the conducting paths and contacts. Naturally, if the same conducting paths and contacts design are used, increase in electrical resistance in these structures is expected due to the lower thickness deposited. Mitigation of this problem is done by fabricating new conducting paths and contacts design which have wider width compared to the previous design. Direct writing lithography used in this method enables the opportunity to structure the deposited metal based on this new design without the necessity to fabricate new masks to be used in mask lithography. The result of the strain gauge, conducting paths, and contacts which are structured using direct writing lithography also shows better alignment and distinction of the structures as shown in Figure 58.

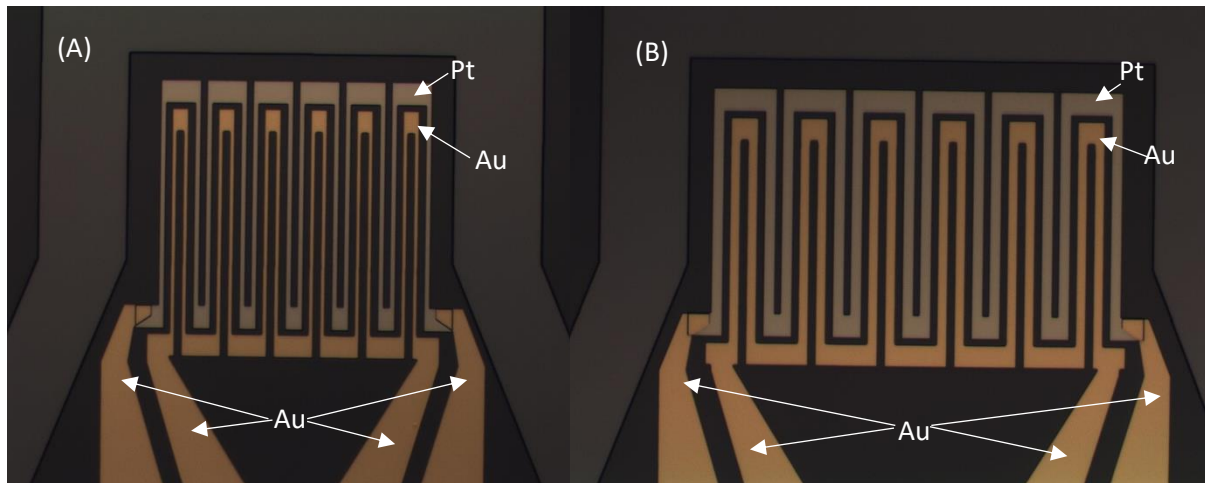


Figure 58: Fabricated platinum and gold strain gauges structured by direct writing lithography and wet etching. Figure (a) represents Pt & Au strain gauges with 10  $\mu\text{m}$  width, Figure (b) represents Pt & Au strain gauges with 20  $\mu\text{m}$  width.

#### 4.1.3. Platinum (Pt) & Chromium (Cr) strain gauges with Gold (Au) contacts

Platinum and chromium strain gauges with widths of 10  $\mu\text{m}$  and 20  $\mu\text{m}$  and thickness of 100 nm has been fabricated. The result of the fabrication can be observed in Figure 59. It is observed that cracks appear throughout the whole chromium structure for both strain gauge widths. The already fabricated platinum strain gauges are also affected, indicated by the appearance of buckles throughout its structure. Cracks in the chromium structure will ruin the electrical conductivity in these structures.

Similar cracks behaviour appearing in chromium thin films which are deposited on top of a polyimide substrate had also been observed by Cordill [76]. In her research, it is reported that chromium on top of a polyimide layer will initiate to form cracks at strain less than 1 percent and for chromium layer with a thickness of 100 nm crack is initiated at strain of only 0.32 percent. These cracks will continue to increase its density, i.e. number of cracks, as the strain percentage of the chromium layer is increased. The thickness of the chromium also dictates the percent strain the material will endure before cracks start forming and the density of the formed

cracks. It is known that the thicker the chromium layer, the smaller strain percentage required to form cracks, i.e. smaller fracture strain. However, thicker layer will produce less cracks density as the strain percentage increases from the initial fracture strain. Therefore, chromium is suitable whenever it is being used as adhesion layer where the thickness is only 5 to 15 nm. However, whenever it is being used as an active element material such as strain gauges in this experiment where the thickness used is up to 100 nm and also subjected to external mechanical deformation, the use of chromium metal is not suitable.

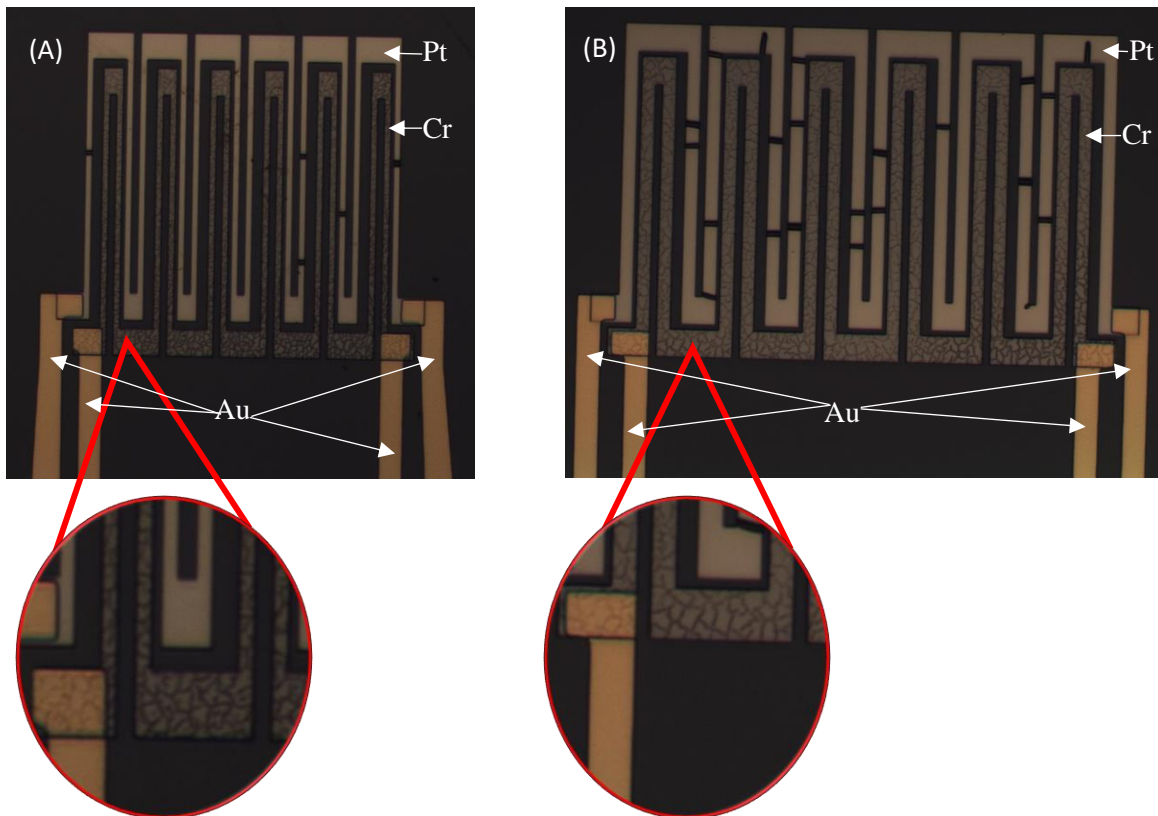


Figure 59: Fabricated platinum and chromium nested strain gauges. Cracks appear in both 10  $\mu\text{m}$  width (a) and 20  $\mu\text{m}$  width (b) chromium strain gauges.

Cracks appearing in the fabricated strain gauges is believed to be generated from the strain applied to the deposited chromium layer during handling of the wafer. Tweezers pressing down on the wafer during handling might introduce microstrains to the layer which would eventually generate micro fracture on the layer. The buckling observed in the platinum strain gauges is believed to be caused by the folds in the polyimide layer beneath it. During the deposition of the chromium layer via sputtering, internal stresses are generated in the polyimide layer due to the bonding made between polyimide and chromium. Naturally, polyimide will try to perform stress relaxation in order to reduce the stress by means of forming strain. However, since the polyimide is bonded with the chromium, the movement of the polyimide chains will be limited therefore strains could not be produced.

As soon as the chromium structure cracks, these limitations is lifted. Therefore, the polyimide chains could move freely to produce strain in order to remove the internal stress.



Since axial strain of the polyimide top layer is accompanied by the contraction of its lateral component, these contractions will in turn compressively stress the metal structures resting on top of it and due to the Poisson's ratio mismatch between the polyimide substrate and the metal on top of it, buckling is formed.

#### 4.1.4. Platinum (Pt) & Aluminium (Al) strain gauges with Gold (Au) contacts

In this research, the fabrication of the platinum and aluminium to be used as strain gauges with gold contacts did not succeed. The fabrication process is only performed until the structuring of the second strain gauge which was made using aluminium. The main reason of failure in this strain gauge candidate is due to the heavily under etched aluminium structure. The heavy under etch occur in this fabrication caused partial aluminium structure removal as shown Figure 60.

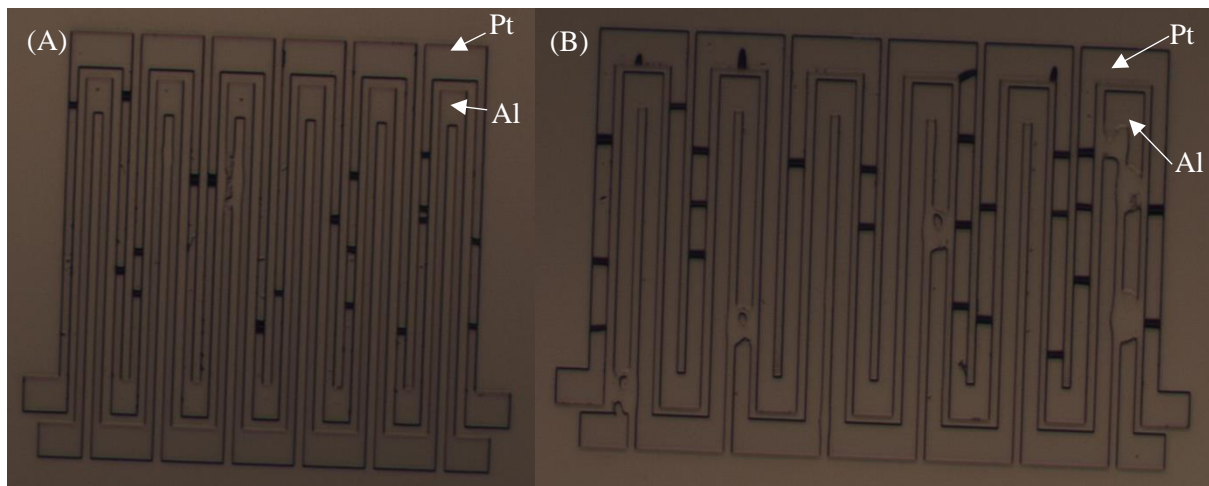


Figure 60: Under etch in aluminium strain gauge causes buckling in the adjacent platinum strain gauge. Figure (A) and (B) represent 10 m and 20 m width strain gauges respectively

As can be seen in the figure above, removal of the aluminium strain gauge structure induces buckling in the adjacent platinum structure. The phenomenon is similar to what have been encountered in the fabrication of chromium strain gauges. In the case of chromium strain gauges, the mobility of the polymeric chains in the polyimide layer to produce strain in order to undergo strain relaxation is increased due to the cracks formed in the chromium structure. In the case of aluminium thin film however, due to the removal of the aluminium structure during wet etching, the limitation to the mobility of the polymeric chains in the polyimide is removed. Therefore, stress relaxation of the polyimide layer occurs and buckles on the platinum structure are present.

It is also important to note that thin aluminium structures deposited on top of a polyimide has been reported to be prone to buckling and delamination [77]. It is suspected that after the deposition of the aluminium layer on top of the polyimide. Strains applied to the wafer during handling might form buckling and delamination of the aluminium. These buckles and delamination could increase the surface area in which the etchants could etch the aluminium

structure during wet etching, therefore accelerating the etching process which in turn leads to under etch the intended structure.

#### 4.1.5. Platinum (Pt) & Titanium (Ti) strain gauges with Gold (Au) contacts

Fabrication of platinum and titanium strain gauges with gold contacts has been conducted. The result of the fabrication exhibits a clear distinction between the structured strain gauges and conducting paths as shown in Figure 61. However, during titanium wet etching, residues are found all over the sensor, specifically on top of the platinum strain gauges. Beside residues, buckles are also observed in the platinum strain gauges.

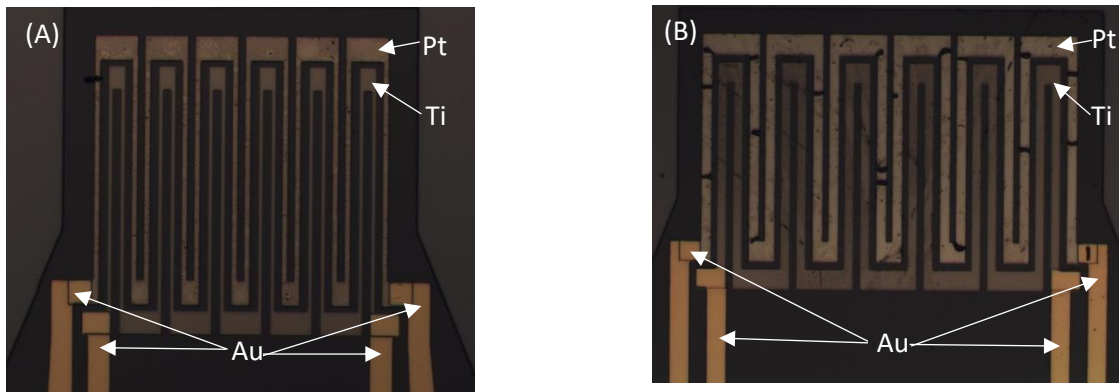


Figure 61: Fabricated platinum and titanium strain gauges with 10  $\mu\text{m}$  (a) and 20  $\mu\text{m}$  (b) strain gauge width

It is suspected that residues that are found on top of the platinum strain gauges are due to the titanium oxide ( $\text{TiO}_x$ ) diffused into the platinum structure. Previous research also suggests that the diffusion of  $\text{TiO}_x$  into platinum structure occur [78]. The diffusion of  $\text{TiO}_x$  into platinum is possible due to the deposition of titanium which is located on top of the platinum structure. In addition, during titanium wet etching using hydrofluoric acid (HF),  $\text{TiO}_x$  which are removed by the etchant could sticks and bonds with the adjacent platinum strain gauge.

HF acid is known to be able to etch silicon dioxides formed on top of the silicon wafer [71]. Since silicon dioxides which are bonded to the polyimide layer on top of it is etched, the adhesion of the polyimide layer to the wafer is compromised which would in turn buckle the platinum structure resting on top of it.

#### 4.2. Temperature Coefficient of Resistance (TCR) Characterization

The characterization of the TCR of each fabricated sensor has been done. The methods used in order to conduct this process can be referred to in Chapter 3. In this experiment, four types of sensor, which consists of two different strain gauge metal combinations and two different strain gauge widths, are subjected to characterization. These sensors are the nested platinum (Pt) and gold (Au) strain gauges and the platinum (Pt) and titanium (Ti) strain gauges.

During the experiment, only the strain gauges made up of platinum and gold shows conclusive changes in its electrical resistance due to the changes in temperature. Both platinum



and titanium strain gauges from both strain gauge widths exhibit inconclusive electrical resistance changes when heat is applied to them. It is suspected that this inconclusiveness in the electrical resistance changes readings is caused by the oxides formed in titanium whenever it is exposed to ambient temperature and pressure. Additionally,  $\text{TiO}_2$  formation is accelerated at elevated temperatures. This leads to the formation of a passivation layer which would also impair the thermal conductivity of the titanium structure hence compromising the result of the measurement, as can be seen in Figure 62.

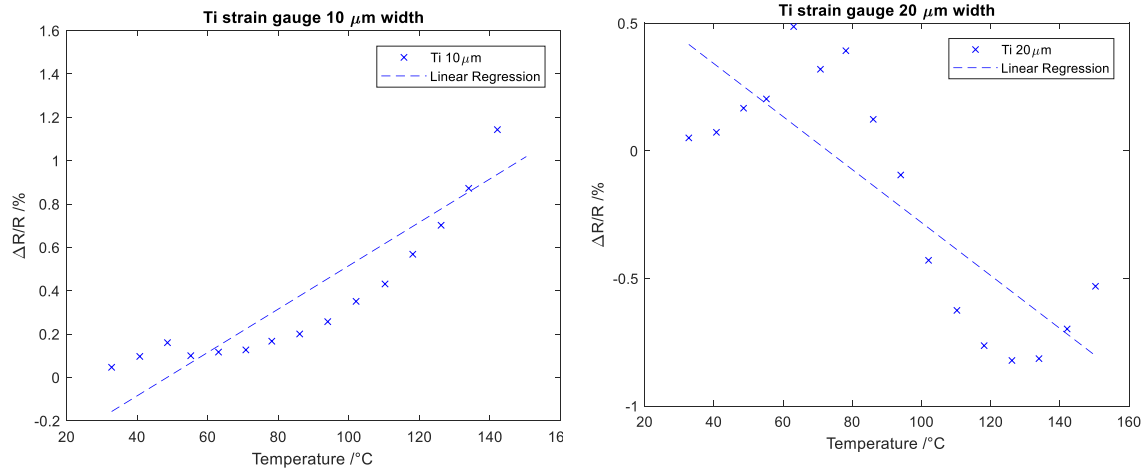


Figure 62: Relative changes in electrical resistance due to changes in temperature for Titanium strain gauge

Platinum and gold strain gauges on the other hand show promising results where a linear correlation occur between the changes in electrical resistance due to the changes in temperature. The result of TCR characterization in both 10  $\mu\text{m}$  and 20  $\mu\text{m}$  strain gauge width of platinum and gold nested strain gauges is presented in Figure 63.

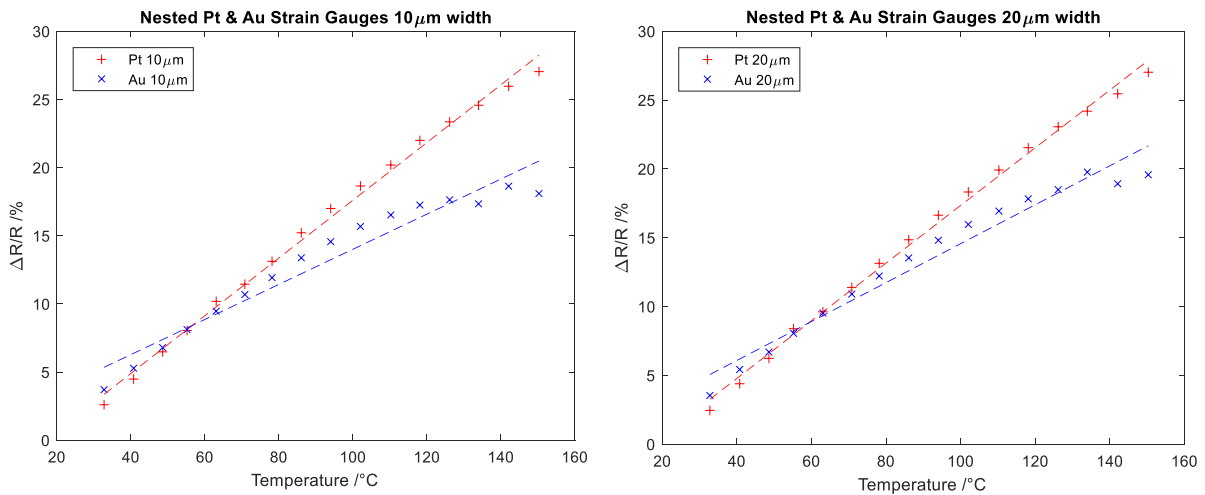


Figure 63: Relative changes in electrical resistance due to changes in temperature affecting the sensor (Rref is set to be the electrical resistance at 24.47°C)

By adhering to Equation 73 as written below,

$$\frac{\Delta R}{R} = \alpha \Delta T$$

where  $\alpha$  is the Temperature Coefficient of Resistance (TCR), determining the TCR could be achieved by means of linear regression (as noted by the dashed lines in Figure 60). In this research, the linear regression used in determining the TCR of each sensor applies the least squares method. After calculation, the TCR obtained are listed in Table 11.

	Pt 10 $\mu\text{m}$	Au 10 $\mu\text{m}$	Pt 20 $\mu\text{m}$	Au 20 $\mu\text{m}$
TCR	$2.1164 \cdot 10^{-3} \text{ K}^{-1}$	$1.2875 \cdot 10^{-3} \text{ K}^{-1}$	$2.0937 \cdot 10^{-3} \text{ K}^{-1}$	$1.4137 \cdot 10^{-3} \text{ K}^{-1}$
$R^2$	0.99614	0.95082	0.99684	0.96749

Table 11: TCR value of various strain gauges calculated by linear regression until 150.31°C

As can be seen from Table 11, both platinum strain gauges with different widths can be fitted to a linear equation more precisely compared to gold strain gauges, as noted by the higher  $R^2$  value. Therefore, it can be concluded that platinum strain gauges exhibited a more linear relationship between the changes in electrical resistance and changes in temperature compared to gold strain gauges. Besides its linearity, platinum strain gauges are also more sensitive to temperature than gold due to its higher TCR value. The relative change in its electrical resistance is around 2% at every 8°C temperature difference. This trait possessed by platinum might not be beneficial if it used as the active element material in normal strain gauge sensors without temperature compensation since the effect on temperature will heavily affects the electrical resistance measurement caused by strains which are being measured. However, in the application of nested strain gauges which are able to simultaneously measure and differentiate between the strain and temperature affecting the strain gauges, this sensitivity towards temperature is necessary to obtain a sensitive and accurate temperature measurement done by the strain gauges.

Gold on the other hand does not show linearity towards changes in temperature as well as platinum (noted by the low  $R^2$  value compared to platinum). It can be deduced that this low  $R^2$  value is mainly caused by the discrepancy from the linear regression line at elevated temperatures, i.e. above 110°C. After conducting the experiment, it is known that the gold target in the magnetron sputtering machine used to sputter gold onto the wafer is nearly depleted. Therefore, there is a probability that the sputtered metal is not entirely gold, it may also come from the holder of the sputtering target which is made from copper, resulting in the nonlinearity of the measurement at higher temperatures due the different behaviour it has at these temperatures. Nevertheless, gold strain gauges fabricated in this research possessed a good sensitivity towards temperatures as shown by the relative change in electrical resistance of more than 1% at every 8°C temperature difference. Therefore, similar to platinum, gold strain gauges strain measurement will also be moderately affected by temperatures in its application.

It is known that the TCR of platinum and gold in bulk to be  $0.0039 \text{ K}^{-1}$  and  $0.0034 \text{ K}^{-1}$  [72], therefore possessing the ratio of 1.147. The ratio obtained from this experiment, referring

to Table 11 which also taken into account the nonlinearity possessed by gold is 1,644 and 1.481 for the 10 $\mu$ m and 20 $\mu$ m strain gauge width respectively, which is quite higher than its bulk materials.

Another linear regression is performed, this time the linear regression does not take into account the nonlinear behaviour possessed by gold at elevated temperatures, i.e. regression is only performed until 110°C. The result can be seen in Figure 64 and the TCR value can be referred to in Table 12. The TCR ratio between platinum and gold obtained from the new TCR values is 1.362 and 1.295 for the 10 $\mu$ m and 20 $\mu$ m strain gauge width respectively. This ratio value is closer to the ratio of the bulk materials, and the TCR value obtained is still within the range as those obtained by Belser and Hicklin [79] for platinum and gold thin films up to 100°C. Linear regression done on this temperature range also exhibit a more linear relationship in the measured data proven by the higher  $R^2$  value for both gold and platinum strain gauges.

	Pt 10 $\mu$ m	Au 10 $\mu$ m	Pt 20 $\mu$ m	Au 20 $\mu$ m
TCR	$2.285 \cdot 10^{-3} \text{ K}^{-1}$	$1.6769 \cdot 10^{-3} \text{ K}^{-1}$	$2.252 \cdot 10^{-3} \text{ K}^{-1}$	$1.737 \cdot 10^{-3} \text{ K}^{-1}$
$R^2$	0.9986	0.9965	0.9987	0.9967

Table 12: TCR value of various strain gauges calculated by linear regression until 110.25°C

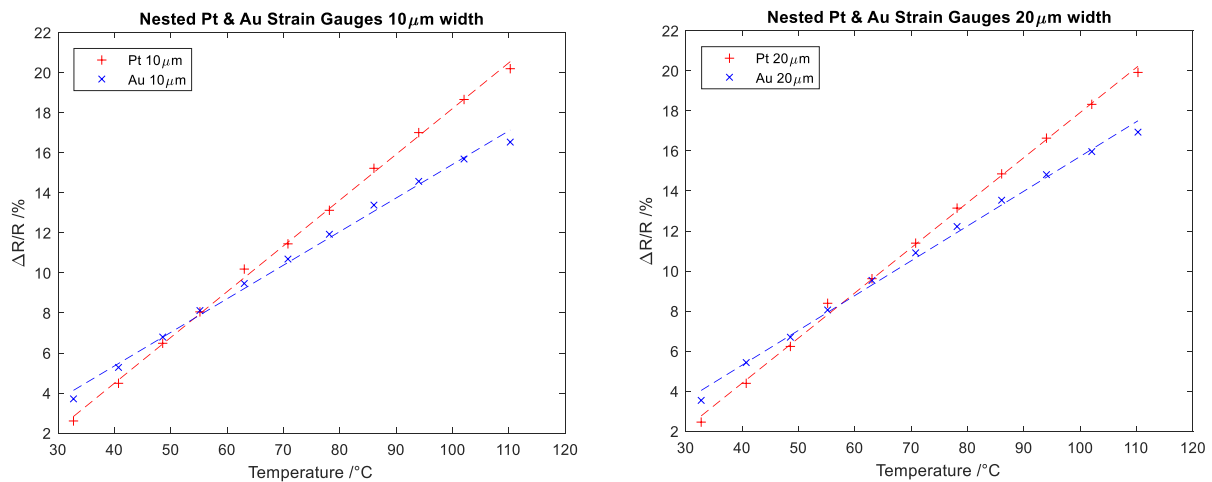


Figure 64: Relative changes in electrical resistance due to changes in temperature affecting the sensor ( $R_{ref}$  is set to be the electrical resistance at 24.47°C).

In this experiment it is also observed that different width size of the strain gauges does not influence the TCR of the strain gauges heavily. Naturally, since the thickness of all the strain gauges are set to 100 nm but the width of the strain gauges differs, the broader strain gauges exhibits lower electrical resistance compared to the thinner ones. However, this does not affect the relative change of electrical resistance. Therefore, the TCR remains relatively similar.

### 4.3. Gauge Factor Characterization

The results of gauge factor characterization are presented in Figure 65 through Figure 68. As mentioned previously in Chapter 3 regarding the process for gauge factor characterization, loads reaching 1000 N is applied to the test specimens containing the sensors in steps of 10 N/s. During experiment it is observed that these loads correspond to 0.2 % strain for the test specimens. In this characterization procedure, the sensors which are subjected to the experiment are the same nested strain gauge metal combination as those during TCR characterization.

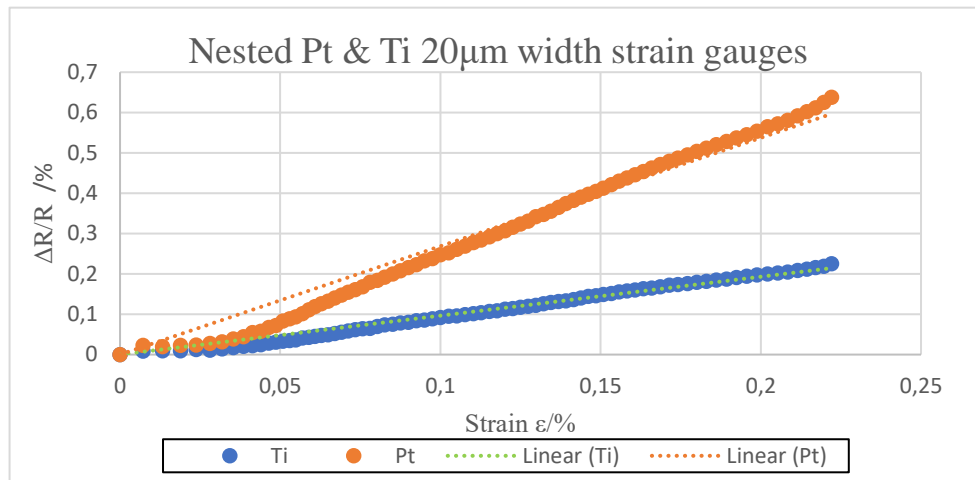


Figure 66: Relative change in resistance with respect to strain for 20 µm width Pt and Ti strain gauges

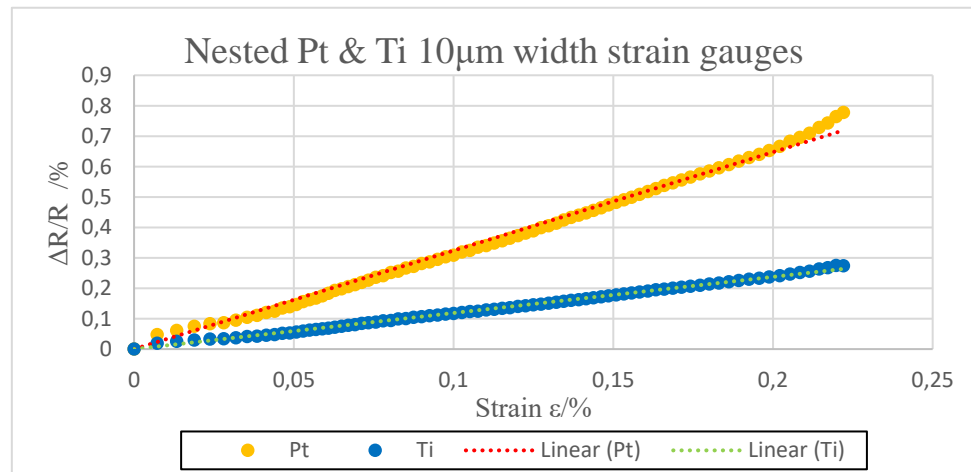


Figure 65: Relative change in resistance with respect to strain for 10 µm width Pt and Ti strain gauges

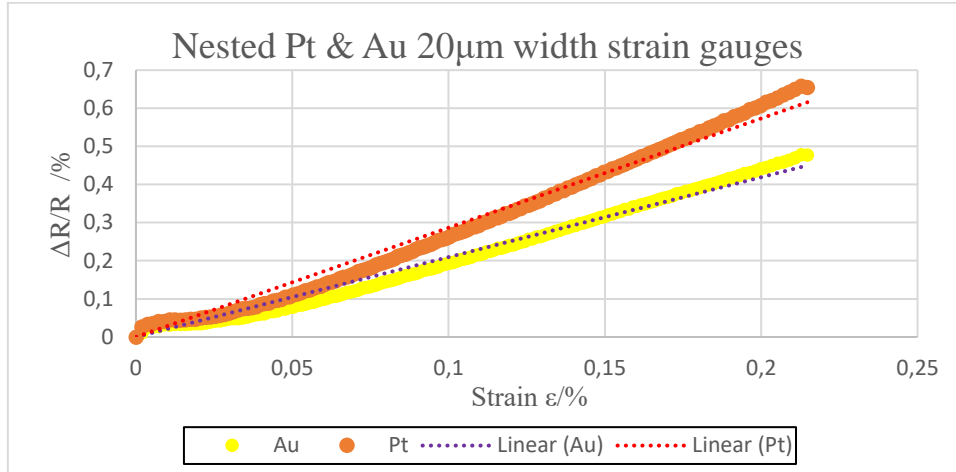


Figure 67: Relative change in resistance with respect to strain for 20 µm width Pt and Au strain gauges

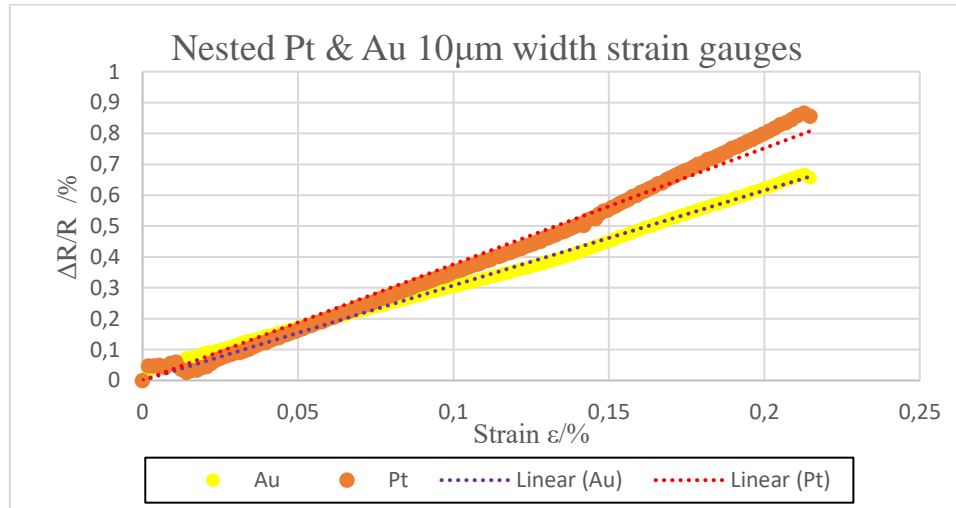


Figure 68: Relative change in resistance with respect to strain for 10 µm width Pt and Au strain gauges

Calculating the gauge factor from this characterization process could be done by linear regression by following Equation 52 as written below.

$$G_f = \frac{\Delta R/R}{\Delta L/L} = \frac{\Delta R/R}{\varepsilon}$$

The calculated gauge factor values for the characterized strain gauges is listed in Table 13.

	Nested Pt & Ti Strain Gauges				Nested Pt & Au Strain Gauges			
	Pt 20µm	Ti 20µm	Pt 10µm	Ti 10µm	Pt 20µm	Au 20µm	Pt 10µm	Au 10µm
$G_f$	2.687	0.965	3.236	1.187	2.866	2.095	3.761	3.077
$R^2$	0.973	0.982	0.993	0.997	0.982	0.983	0.986	0.993

Table 13: Gauge factor value of various strain gauges calculated by linear regression

As can be seen from the figures above, almost all strain gauges excluding the 10µm Pt & Ti strain gauges and the 10µm Au strain gauge exhibit a non-linear relationship between relative changes in resistance with strain. These non-linearities can be deduced to be affected by the non-linear relationship the strain of the test specimen has with respect to time as shown

in Figure 69 and Figure 70. Linear regression done on both of these figures results in the less  $R^2$  value obtained compared to the polynomial regression done on them which in turn describe the strain deformation with respect to time is not simply linear.

Strain deformation occurring in the test specimen is caused by the load applied to it by the pull test apparatus. The amount of the load is determined by the mechanical characteristics of the test specimen. In this experiment, a fairly thin steel bar (3 mm thick) is used, therefore dictating the amount of force needed at each step of the characterization procedure to strain the test specimen to be relatively small ( $10 \text{ N s}^{-1}$ ). The small force required by the test specimen could not be precisely given by the test apparatus, therefore a jump in strain during the initial step of the characterization procedure and the non-linearity of the strain with time throughout the experiment can be observed. It is advised for future work in characterizing the gauge factor of the sensor to utilize test specimens which require significantly more force to be strain deformed. The bigger the force required by the test specimen, the wider the allowance for fluctuations in the force applied to produce a linear relationship between strain and time.

It can be concluded that due to these non-linearities between the relative change in resistance and strain, linear regression used in order to determine the gauge factor of metals in Table 13 produces values which are differ from the already established gauge factor measurement for gold and platinum in other studies. The gauge factor for gold film with 100nm thickness obtained in this experiment is 2.095 and 3.077 for  $20\mu\text{m}$  and  $10\mu\text{m}$  width strain gauges respectively, whereas in the research conducted by Chunshien et al. [80] a 30nm thick gold film possessed a gauge factor of 2.6. Similarly, in the case for platinum the most similar gauge factor value obtained to the reported value in other studies was those found in the platinum and gold nested strain gauges with  $10\mu\text{m}$  strain gauge width where it possesses the gauge factor of 3.761 compared to the gauge factor of 3.85 obtained by Fricke [81].

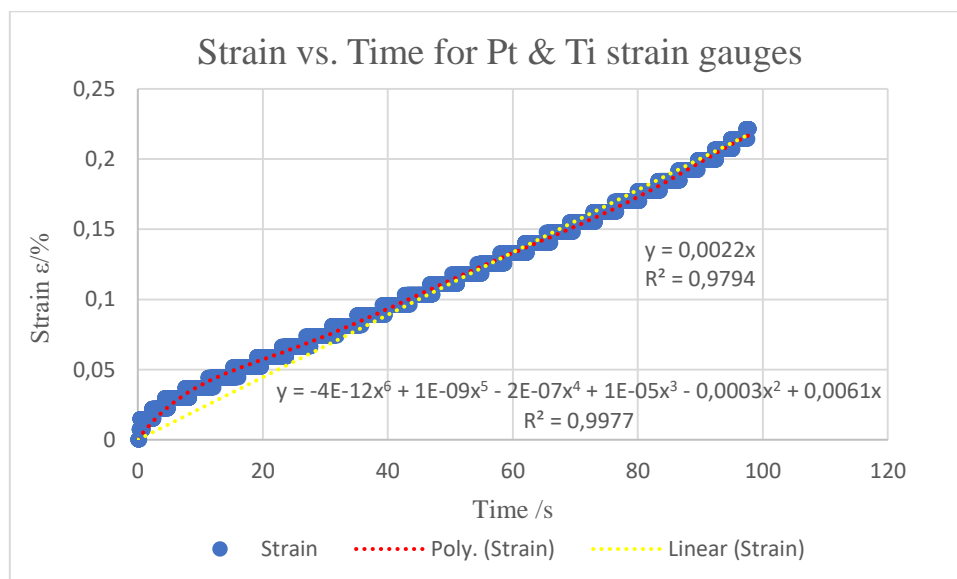


Figure 69: Strain of the test specimen containing sensors with Pt & Ti with respect to time

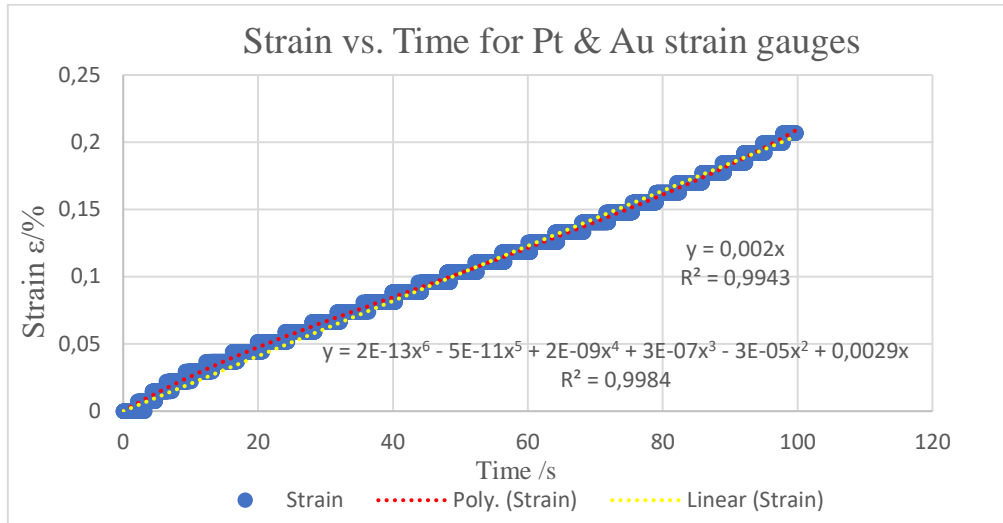


Figure 70: Strain of the test specimen containing sensors with Pt & Au with respect to time

#### 4.4. Gasket Condition Monitoring

The implementation of nested strain gauges sensor embedded inside the gasket to conduct condition monitoring has been performed successfully for nested platinum and gold strain gauges with gold contacts and conducting paths. The Pt & Au sensor embedded inside exhibits changes in its electrical resistivity due to various factors affecting the gasket such as compression, heating, aging, cooling down, and decompression. Condition monitoring done by the sensor inside the gasket which utilizes titanium strain gauges also exhibit changes in its electrical resistance. However, these changes are in an increasing trend over the whole period of the experiment despite various factors affecting the gasket has been altered which would increase as well as decrease the electrical resistance as observed in the Pt & Au sensor. The result of gasket condition monitoring done by nested Pt & Au 20μm width strain gauges sensor and the 10μm width strain gauge is presented in Figure 71 through Figure 73.

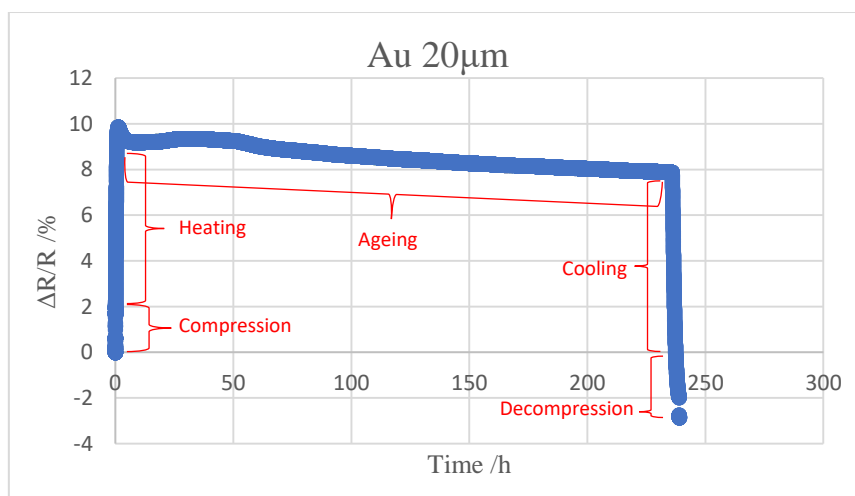


Figure 71: Relative changes in resistivity during gasket ageing for 20μm width Au strain gauge in Pt & Au 20μm width nested strain gauges.

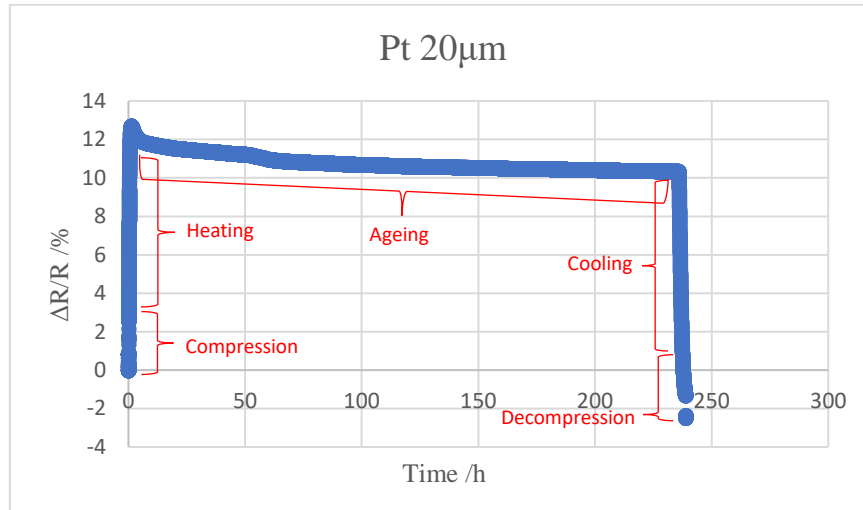


Figure 72: Relative changes in resistivity during gasket ageing for 20 $\mu$ m width Pt strain gauge in Pt & Au 20 $\mu$ m width nested strain gauges.

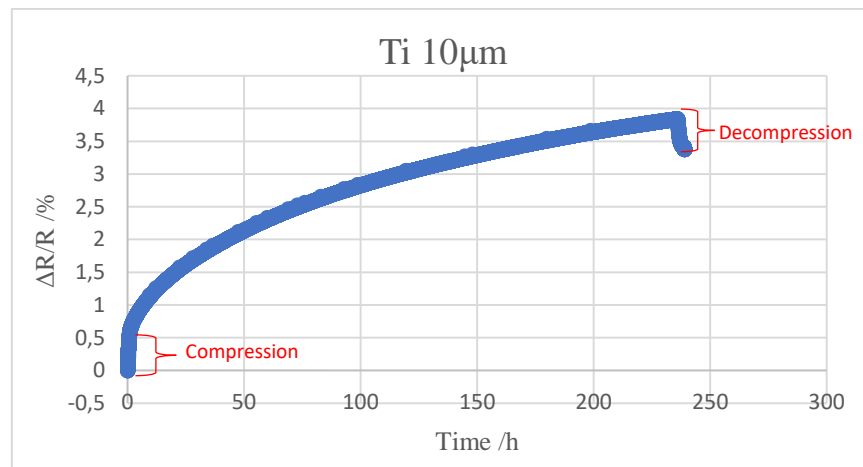


Figure 73: Relative changes in resistivity during gasket ageing for 10 $\mu$ m width Ti strain gauge in Pt & Ti 10 $\mu$ m width nested strain gauges

As can be seen from the figures above, a clear distinction between each step during the gasket condition monitoring can be observed for gold and platinum strain gauges. Titanium strain gauge relative change of resistance exhibits a more or less logarithmic behaviour as the duration of the experiment increases. The only distinguishable change in resistance for titanium strain gauge are only those during compression and decompression where significant loading and unloading done on the sensor will change the length of the sensor considerably therefore changing its resistance.

These increase in resistance is suspected to be caused by the growth of titanium oxides ( $\text{TiO}_x$ ) on the strain gauges when placed at elevated temperature during heating and ageing of the gasket. Beside the effect from temperature, prolonged exposure to elevated temperature will increase the concentration of these oxides [82]. Therefore, further increasing the electrical resistance of the strain gauge as the ageing continues. Despite the formation of oxides in the titanium strain gauges, changes in geometrical aspect of the titanium strain gauge which occur



during compression and decompression still leads to the changes in relative electrical resistance.

In the case of gold and platinum strain gauges embedded inside the silicone O-ring gasket, each process step during the gasket condition monitoring experiment produce change in resistance as theoretically expected. During compression of the gasket, the reduction in the height of the gasket is followed by the radial strain of the gasket. Strain gauges embedded inside the gasket will also be strained along with the gasket. Since no heat was applied in this process, it can be deduced that these changes in resistance is caused by the elongation of the strain gauges due to the compression of the gasket.

After compression by means of tightening the bolt of the compression plates, the gasket is placed in an oven to be heated to 70°C. In this step, the length of the strain gauges embedded inside is assumed to remain constant. Naturally, since the strain gauges are placed inside an oven at elevated temperature, thermal expansion of the strain gauges are expected to occur which would elongate or strain the strain gauges further. However, at temperature of only 70°C the thermal expansion is assumed to be miniscule and it can be regarded as negligible in contributing to the changes in electrical resistance. The main cause in electrical resistance changes in this step is due to the changes in temperature affecting both the gasket and the strain gauges embedded inside.

Ageing of the gasket starts when there is a reduction in the relative change in electrical resistance as noted in the figures above. Silicone gasket could be regarded as viscoelastic material [83]. Therefore, the reduction in electrical resistance are caused by the stress relaxation the silicone gasket performed during ageing. During stress relaxation, the strain of the gasket remains constant accompanied by the reduction in stress which occur inside the gasket. Since the Young's modulus of the strain gauges remains the same but the stress affecting it is reduced, the now reduced stress could not keep the strain deformation of the strain gauges as it was, resulting in the reduction of strain in the strain gauges. Due to the length of the strain gauges is now decreased, its resistance is also reduced as explained in Equation 54, which leads to the overall reduction in relative change in electrical resistance as the ageing continues since more stress relaxation is continued by the gasket.

Cooling and decompression of the gasket exhibit an opposite behaviour compared to heating and compression done on the gasket regarding the relative change in electrical resistance. Both of these processes will produce negative change in electrical resistance. Based on Equation 73 and 52, the removal of heat which would lead to the negative change in temperature will produce negative change in electrical resistance. Similarly, since external stresses applied by the compression plates is now removed, the gasket will try to return to original state by contraction. The contraction will eventually reduce the length of the strain gauges which would reduce the relative change in electrical resistance.

The final thickness of all the gaskets tested in this experiment after decompression is found to be 2.5 mm from its original thickness of 3 mm. It can be calculated from Equation 1 that the compression set of the gasket to be 66.7% which indicates that a prolonged gasket ageing has

occurred. This statement is also backed by the fact that in the case of gold and platinum strain gauges, both of them exhibit a negative relative change in electrical resistance. A negative value indicates that the final electrical resistance of the strain gauge is lesser than those before ageing, i.e. the electrical resistance of the strain gauge after sensor integration into the gasket. Smaller electrical resistance is caused by the reduction of the length of the strain gauges embedded inside the gasket (assuming there are no changes in the ambient room temperature). The probable explanation regarding this phenomenon is due to the lesser stress affecting the strain gauges inside the gasket after the gasket has been aged.

Initially during the integration of the sensor inside the gasket, the sensor acts as a foreign body to the gasket which results in the internal stresses formed inside the gasket since the polymeric chains in the gasket could not form crosslinks with the sensor. These internal stresses will in turn strained the strain gauges embedded inside even when there is no external load affecting the gasket. However, based on the experiment done on this research, these internal stresses seem to be reduced due to the prolonged stress relaxation done by the gasket during ageing. As a result, since less internal stresses are now present in the gasket after ageing, the strain gauges length are now shortened compared to the initial length after sensor integration into the gasket. Thus, a negative relative change in electrical resistance is observed.

It is also important to note that during the silicone gasket condition monitoring using strain gauges done by Schotzko [53], the final resistance of the strain gauge after decompression is higher than its initial, i.e. producing a positive relative change in electrical resistance. In his experiment, the final compression set he obtained after 72 hours of ageing is 34% which indicate that ageing has occur albeit not as much as what is presented in this master thesis report where the duration of the ageing is 239 hours. It can be concluded from both researches that the duration of the ageing will further induce stress relaxation inside the gasket, where at shorter ageing duration the stress relaxation could not reduce the internal stress of the gasket during sensor integration and for ageing at longer duration the stress relaxation done by the gasket is long and high enough to reduce the internal stress during sensor integration.

Distinguishing the effect of strain and temperature affecting the gasket from the relative change in electrical resistance using Equation 77 and Equation 78 had not been successful. The result of this calculation is presented in Figure 74. It can be concluded that the calculation is invalid due to several reasons explained in the following sentences. The result show changes in temperature during compression and decompression where changes in temperature is expected to be constant. Changes in strain is also observed during heating, assuming that thermal expansion of the strain gauges is negligible, strain during this step is expected to be constant. Ageing exhibit huge fluctuations in temperature where it supposes to be constant. In addition, the value of the change in temperature is significantly higher compared to the anticipated values. Gasket decompression exhibit an increase in strain where it is expected that due to the retraction of the gasket to return to its original form the strain of the strain gauges embedded inside should be decreased.

The reason of failure in this calculation is caused by the uncertainty in the values obtained during the strain gauge characterization. Referring to Equation 77 and Equation 78, a

proper characterization of the gauge factor and temperature coefficient of resistance is required in order to obtain valid calculation in distinguishing the strain and temperature affecting the gasket. Difficulties such as non-linearities occur during the sensor characterization especially in gauge factor characterization compromise the validity of the obtained gauge factor data.

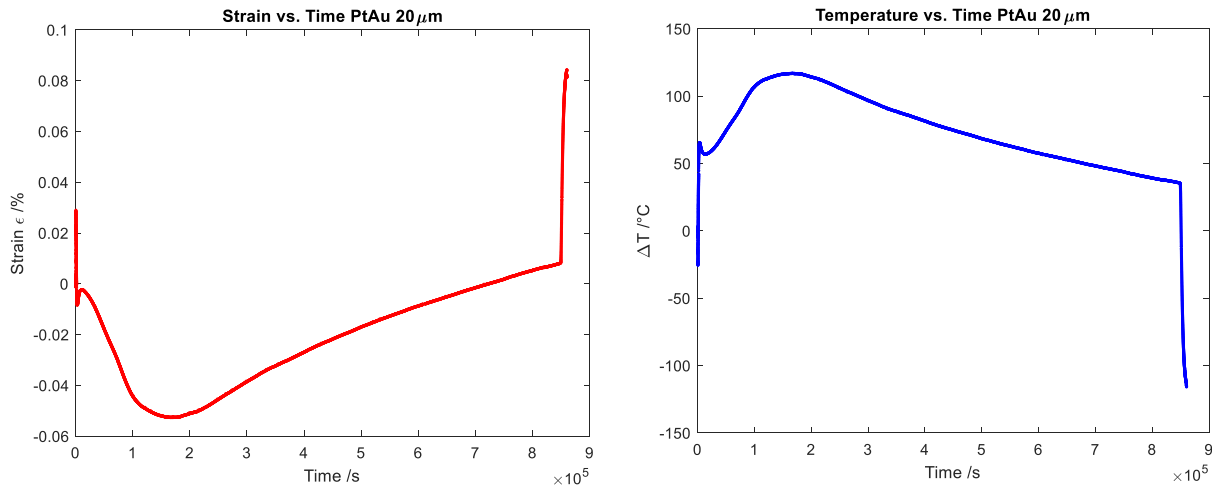


Figure 74: Calculated strain and temperature affecting the gasket during condition monitoring

# CHAPTER 5

## Conclusion and Future Outlook

### 5.1. Conclusion

The main objective in this research regarding the simultaneous measurement for strain and temperature in a gasket by utilizing nested strain gauges has been carried out. The research starts with the fabrication of the sensor from various metal combination candidates to be used as the nested strain gauges material and the conducting paths along with contacts. Suitability of the metal combination to be used in the sensor will take into consideration the fabrication process involved, the result of the fabrication, and the measurement data it produces during application.

The metal combination candidates for strain gauges investigated in this thesis are the nested platinum-gold, platinum-titanium, platinum-aluminium, and platinum-chromium strain gauges. Whereas the candidate material for the conducting paths along with the contacts are gold and copper. From all the metal combination candidate available, only nested platinum-gold strain gauges with gold conducting paths structured using direct writing lithography exhibit reasonable measurement data during its application inside a gasket. On the other hand, platinum-gold strain gauges with gold conducting paths structured using lift-off showed electrical shortages in the conducting path due to the inability of the NMP etchant to remove the negative resist with the deposited gold on top of it located between the conducting paths. In this research, sensors which are made with platinum-gold strain gauges with copper conducting paths and contacts are also successfully fabricated. However, these sensors are found to be incapable to be integrated into the gasket since compressive stresses occur on the metallic film on top of the polyimide substrate will significantly curl the sensor.

Investigation regarding the fabrication of the sensor using other metal combination candidate have shown that both platinum-aluminium and platinum-chromium nested strain gauges exhibit buckling in the platinum strain gauge structures for both sensor due to the defects occur in chromium and aluminium. At thickness of 100nm the chromium strain gauge exhibits cracks all over the structure whereas for aluminium strain gauge heavy under etching occur caused by the increased surface area due to the buckling in the aluminium structure. Platinum-titanium nested strain gauges has been successfully fabricated, although some defects in form of residues which is believed to be the oxide from titanium during wet etching appear on top of all the fabricated structures. These defects are believed to be the cause of the inconclusive measurement data during the TCR characterization and gasket condition monitoring measurement using platinum-titanium nested strain gauge sensor.

Characterization on the sensor in order to obtain the temperature coefficient of resistance (TCR) and gauge factor ( $G_f$ ) of the strain gauges inside the sensor has also been investigated. Characterization of the TCR is done by heating the sensor on top of the hotplate from room temperature to 150°C. TCR obtained for gold 10 $\mu$ m and 20 $\mu$ m width strain gauges to be 1.6769

$K^{-1}$  and  $1.737 K^{-1}$  respectively. Whereas for platinum  $10\mu m$  and  $20\mu m$  width strain gauges to be  $2.285 K^{-1}$  and  $2.252 K^{-1}$  respectively. Determining the gauge factor of the strain gauges inside the sensor produce an inconclusive result due to the non-linearity found in strain of the test specimen with respect to time during pull test. The gauge factor values obtained for platinum-gold nested strain gauges sensor with  $10\mu m$  strain gauge width are 3.0767 for gold and 3.7611 for platinum, whereas the one with  $20\mu m$  strain gauge width are 2.0952 for gold and 2.866 for platinum. Gauge factor characterization is also investigated for the platinum-titanium strain gauges. The values obtained for platinum-titanium  $10\mu m$  strain gauge width is 1.1869 for titanium and 3.2369 for platinum, whereas the one with  $20\mu m$  strain gauge width is 0.9652 for titanium and 2.6869 for platinum.

Investigation result regarding the conditioning monitoring function of the strain gauges inside the gasket has shown that changes to the various factor affecting the gasket such as loads and heats is detected by the sensor embedded inside the gasket in form of changes in the electrical resistance of the strain gauges. However, in this research it is found that only platinum-gold strain gauges which are able to perform this function. These strain gauges exhibit a negative value for the relative change in electrical resistance after the whole artificial ageing of the gasket which corresponds to 66.7% compression set. Platinum-titanium strain gauges exhibit a logarithmic rise in terms of its changes in resistance with disregard to the various factor affecting the gasket during the whole duration of the experiment. The only factors affecting the gasket which are detected by the platinum-titanium strain gauges are during compression and decompression.

Calculating the amount of strain and temperature affecting the gasket during ageing has also been performed. However, the result is believed to be invalid due to the changes in strain and temperature at regions where it is not expected to occur, e.g. changes in strain during heating and cooling down or changes in temperature during compression and decompression. It is believed that this invalidity is caused by the invalid data obtained during the characterization of the sensor, especially in determining the gauge factor of the strain gauges in the sensor.

All of the data recorded during the whole duration of this master thesis can be referred to in the CD attached to this report.

## **5.2. Future outlook**

In terms of fabrication of the sensors and gaskets. It is advised in future work to investigate the possibility to use other metal combination to be used as the nested strain gauges and conducting paths for gasket condition monitoring. Enlarging the contacts area of the sensor such as those found in platinum-gold structured with direct writing lithography could also be beneficial to ease the wire bonding process. Fabricating the strain gauges on top of a different substrate than polyimide, preferably utilizing the similar rubber material as the host gasket material, should also be investigated to determine the effect of sensor integration into the gasket in terms of the internal stresses generated. Investigation regarding the integration of the nested

strain gauges with other gasket material such as rubber should also be conducted to determine the effectiveness of the sensor in all commercially available material for the gasket.

In terms of characterization of the strain gauges, determining the gauge factor of the sensor is known to be heavily affected by the linearity of strain affecting the test specimen with respect to time. Since the linearity of the test specimen is affected by the linearity of load applied to it, a thicker test specimen compared to the one used in this research is advised to obtain a linear strain result due to the more tolerance in load fluctuations during pull-test. Therefore, a more credible gauge factor value could be obtained which would enable the opportunity to distinguish the strain and temperature affecting the gasket during condition monitoring.

In terms of gasket condition monitoring, it is observed in this research that the final value of the relative change in electrical resistance is smaller than its initial one, i.e. before ageing. It is assumed that it is caused by the internal stress generated during the integration of the sensor into the gasket. It is therefore beneficial to determine how much internal stress generated during integration by measuring the resistivity of the strain gauges before and after integration into the gasket.

## REFERENCES

- [1] Presidential Commission, "Report of the Presidential Commission on the Space Shuttle Challenger Accident," *Report to the President; NASA History Office: Washington, DC, USA*, June 1986.
- [2] J. Berk, "Leaks", *In Systems Failure Analysis*, ASM International: Materials Park, OH, USA, pp. 131–139, 2009.
- [3] F. Awaja, et al. "Cracks, microcracks and fracture in polymer structures: Formation, detection, autonomic repair", *Progress in Materials Science* 83, pp. 536–573, 2016.
- [4] J. Sauer, G. Richardson, "Fatigue of polymers", *International Journal of Fracture*, Vol. 16, No. 6, pp. 499–532, December 1980.
- [5] M. Jaunich, et al., "Understanding the low temperature properties of rubber seal", *PATRAM 2010 Conference Paper*, 2010.
- [6] J. Unwin, M. Coldwell., et al., "Airborne Emissions of Carcinogens and Respiratory Sensitizers during Thermal Processing of Plastics", *Ann. Occup. Hyg.* 57 (3), pp. 399–406, 2013.
- [7] J. White, "Polymer ageing: physics, chemistry or engineering? Time to reflect", *C. R. Chimie* 9, 2006.
- [8] S. Stivala, "Structure vs stability in polymer degradation", *Polym. Eng. Sci.* 20 (10), pp. 654–661, 1980.
- [9] Y. Neo, et al., "Influence of heat curing on structure and physicochemical properties of phenolic acid loaded proteinaceous electrospun fibers", *J. Agr. Food Chem.* 62 (22), pp. 5163–5172, 2014.
- [10] S. Ray, A. Bhowmick, "Influence of untreated and novel electron beam modified surface coated silica filler on dynamic mechanical thermal properties of ethylene-octene copolymer", *Polym. Eng. Sci.* 44 (1), pp. 163–178, 2004.
- [11] A. Wahab, A. Farid, "Correlation between Compression-Set and Compression Stress-Relaxation of Epichlorohydrin Elastomers", *Polymers & Polymer Composites*, Vol. 19, No.8, 2011.
- [12] D. Gräbner, G. Dumstorff, W. Lang, "Simultaneous Measurement of Strain and Temperature with two Resistive Strain Gauges made from Different Materials", *Procedia Manufacturing*, 2018.
- [13] E. Brinksmeier, et al., "Process Signatures – an Alternative Approach to Predicting Functional Workpiece Properties", *Procedia Engineering* 19, pp. 44–52. 2012.
- [14] G. Kahandawa, J. Epaarachchi, et al., "Use of FBG Sensors for SHM in Aerospace Structures", *Photonic Sens.* 2, pp. 203–214, 2012.
- [15] A. Rytter, "Vibration Based Inspection of Civil Engineering Structures", Ph. D. Dissertation, Department of Building Technology and Structural Engineering, University of Aalborg, Denmark, 1993.



- [16] A. Güemes, C. Fritzen, D. Balageas, “Introduction to Structural Health Monitoring. In Structural Health Monitoring”, *ISTE: London*, UK, pp. 13–44, 2006.
- [17] “Aircraft Accident Report, Aloha Airlines Flight 243, Boeing 737-100, N73711, Near Maui, Hawaii, April 28, 1998”. National Transportation Safety Board. June 14, 1989.
- [18] F. Semperlotti, “Structural Damage Detection Via Nonlinear System Identification and Structural Intensity Methods”, Ph. D. Dissertation, The Pennsylvania State University, USA, pp. 297, 2009.
- [19] T. Schotzko, W. Lang, “Embedded Strain Gauges for Condition Monitoring of Silicone Gaskets”, *Sensors 2014*, pp. 12387-12398, 2014.
- [20] G. Dumstorff, S. Paul, W. Lang, “Integration Without Disruption: The Basic Challenge of Sensor Integration”, *IEEE Sensors Journal*, vol. 14, no. 7, pp. 2102-2111, July 2014.
- [21] P.C. Hill, B.J. Eggleton, “Strain gradient chirp of fiber Bragg gratings”, *Electronics Letters*, vol. 30, no.14, pp. 1172–1174, 1994.
- [22] M. LeBlanc, S. Y. Huang, et al., “Tunable chirping of a fiber Bragg grating using a tapered cantilever bed”, *Electronics Letters*, vol. 30, no. 25, pp. 2163–2165, 1994.
- [23] M. Catrysse, R. Puers, et al., “Towards the integration of textile sensors in a wireless monitoring suit”, *Sensors and Actuators*, vol. 114, Issues 2-3, pp. 302-311, 2004.
- [24] Fraunhofer ISI; dena; VDMA, Compressed Air Facts. *Druckluft Effizient* 2003.
- [25] Z. Nakutis, P. Kaskonas, “An Approach to Pneumatic Cylinder on-Line Conditions Monitoring”. *Mechanika*, 4, pp. 41–47, 2008.
- [26] M. Kincart, J. Stark, “Determining Reasons for Head Gasket Failures in Air-Cooled Engines with a Simple Testing Methodology”, *SAE World Congress Paper*, 2004.
- [27] ASTM D 395—03, “Standard Test Methods for Rubber Property—Compression Set”, *ASTM International*.
- [28] ISO 815, "Rubber, Vulcanized or Thermoplastic – Determination of Compression Set at Ambient, Elevated or Low Temperatures."
- [29] F. Simon, “Über den zustand der unterkühlten flüssigkeiten und gläser”, *Z. Anorg. Allg. Chem.* 203, pp. 219–227. 1931.
- [30] K. Dill, S. Bromberg, “Molecular Driving Forces: Statistical Thermodynamics in Biology, Chemistry, Physics, and Nanoscience”, Garland Science. 2010.
- [31] L.C.E. Struik, “Physical Aging in Amorphous Polymers and Other Materials”, Elsevier. Amsterdam, 1978.
- [32] A.J. Kovacs, “Applicability of the Free Volume Concept on Relaxation Phenomena in the Glass Transition Range”, *Rheologica Acta*, Band 5, Heft 4, 1966
- [33] White, J.R., *Polymer Testing* 4 (1984) 165.



- [34] G.F.L. Ehlers, K.R. Fisch, “The Effect of Aging on the Glass Transition Temperature of some Polymers”, *Final Technical report Nov. 1974 - Nov. 1975*, Air Force Materials Laboratory, 1977.
- [35] S. Ray, R. P. Cooney, “Thermal Degradation of Polymer and Polymer Composites”, Hybrid Polymers Research Group, The University of Auckland, Auckland, New Zealand.
- [36] J. Cheng, Y. Pan, et al., “Mechanisms and kinetics studies on the thermal decomposition of micron Poly(methyl methacrylate) and polystyrene”, *J. Loss Prevent Pro*, 40, pp.139-146, 2016.
- [37] G.Y. Li, J.L. Koenig, “A review of rubber oxidation”, *Rubber Chem. Technol.* 78 (3), pp. 0355-390. 2005.
- [38] K.A. Holland, I.D. Rae. “Thermal-degradation of a compound which models the head-to-head linkage in poly(methyl methacrylate)”, *Aust. J. Chem.* 40 (4), pp. 687-692. 1987
- [39] A.K. Bhowmick, S. Ray, et al., “Photomechanical degradation of thermoplastic elastomers”, *J. Appl. Polym. Sci.* 99 (1), pp. 150-161. 2006.
- [40] I. Jakubowicz, “Evaluation of degradability of biodegradable polyethylene (PE)”, *Polymer Degradation and Stability*. 80: 39–43. 2003.
- [41] D.R. Tayler, “Mechanistic aspects of the effect of stress on the rate of photochemical degradation reactions in polymers”, *J Macromol Sci Part C Polym* 44(4):351-88, 2004.
- [42] B. Singh, N. Sharma, “Mechanistic implications of plastic degradation”, *Polym. Degrad. Stabil.* 93 (3), pp. 561- 584, 2008.
- [43] Gowariker, V. R. (Vasant R.), Viswanathan, N. V and Sreedhar, Jayadev Polymer science. Wiley, New York, 1986.
- [44] <https://polymerdatabase.com/polymer%20chemistry/Thermal%20Degradation.html>. Accessed on 25 March 2019, at 15:54.
- [45] M. Cerrada, “Introduction to the Viscoelastic Response in Polymers”, *Thermal Analysis. Fundamentals and Applications to Material Characterization*, pp. 167-182, 2005.
- [46] P. Hauseux, J. Hale, S. Bordas, “Calculating the Malliavin derivative of some stochastic mechanics problems” , 2017
- [47] T. Osswald, G. Menges, “Material Science of Polymers for Engineer, 3rd Edition”, Hanser Publishers, Munich
- [48] D. Roylance, “Engineering Viscoelasticity”, Cambridge, MA 02139: Massachusetts Institute of Technology. 2001
- [49] Lawrence E. Nielsen (1969 Cross-Linking–Effect on Physical Properties of Polymers, *Journal of Macromolecular Science, Part C*, 3:1, pp. 69-103, 1969.
- [50] C.A. Sciammarella, F.M.Sciammarella, “Experimental Mechanics of Solids”, John Wiley and Sons Publication, 2012.

- [51] V. Button, “Principles of Measurement and Transduction of Biomedical Variables”, *Academia Press*, pp. 155-219, 2015.
- [52] A. A. Barlian, P. Woo-Tae, J. R. Mallon, A. J. Rastegar, and B. L. Pruitt, "Review: Semiconductor Piezoresistance for Microsystems." *Proc IEEE Inst Electr Electron Eng*, vol. 97, 3, pp. 513-552, 2009.
- [53] Schotzko, T., “Sensor Integration in Silicone and Rubber Gaskets for Structural Health Monitoring”, Doctorate Dissertation, Universität Bremen, 2015.
- [54] Application Note 078, Strain Gauge Measurement – A Tutorial, National Instruments
- [55] M. Davies, T. Ueda, R. M'saoubi, B. Mullany and A. Cooke, "On the measurement of temperature in material removal processes," *CIRP Ann. Manuf. Technol.*, no. 56, pp. 581-604, 2007.
- [56] H. Tönshoff, T. Friemuth and J. C. Becker, "Process monitoring in grinding," *CIRP Ann Manuf. Technol.*, no. 51, pp. 551-571, 2002.
- [57] Abbas, Khawar. "Characterization of the mechanical properties of freestanding platinum thin films", 2013.
- [58] İ Tunçöz, et.al., “A Hybrid Trailing Edge Control Surface Capable of Camber and Decamber Morphing”, 2015.
- [59] P. G. Slade, “Electrical Contacts: Principles and Applications”, New York, USA: Marcel Dekker, 1999.
- [60] C. Li, P. Hesketh, G. Maclay, “Thin gold film strain gauges”, *Journal of Vacuum Science & Technology*, 1994
- [61] I. Sinclair, “Passive Components for Circuit Design”, Newnes, pp.32-63, 2001
- [62] <http://www.goodfellow.com/E/Polyimide.html>. Accessed on 28 May 2019, at 15:31
- [63] R.M. Jennings, “An Investigation of the Effects of Curing Conditions on the Residual Stress and Dimensional Stability in Polyimide Films”, Doctorate Dissertation, University of Massachusetts, 1993.
- [64] S. Chang, Y. Huang, C. Chang, “Effect of Residual Stress on Mechanical Properties and Interface Adhesion Strength of SiN Thin Films”, National Chung Shing University.
- [65] [http://www.upilex.jp/en/varnish\\_grade.html#01](http://www.upilex.jp/en/varnish_grade.html#01). Accessed on 28 May 2019 at 16:08.
- [66] W. Chen, et al., “Thermal imidization process of polyimide film: Interplay between solvent evaporation and imidization”, *Polymer* 109, pp. 205-215, 2017.
- [67] S. Hau-Riege, “An introduction to Cu electromigration”. *Microel. Reliab.*, vol. 44, pp. 195–205, 2004.
- [68] B. Li, T. D. Sullivan, T. C. Lee, et al. “Reliability challenges for copper interconnects”, *Microel. Reliab.*, vol. 44, pp. 365–380, 2004.

- [69] F. Faupel, R. Willecke, A. Thran, “Diffusion of metals in polymers”, *Materials Science and Engineering: R: Reports*, Vol. 22, Issue 1, pp. 1-55, 1998.
- [70] Technical datasheet *Elecolit*® 414, *Panacol Adhesive*.
- [71] V. Matylitskaya, S. Partel, S. Kasemann, “Study of selective wet etching of titanium towards copper in hydrofluoric free etchant”, 2015.
- [72] Smithell, “Metals Reference Book”, Butterworth's Scientific Publications, Ltd., London, 1949
- [73] E. Chason, et al., “A kinetic model for stress generation in thin films grown from energetic vapor films”, *Journal of Applied Physics* 119, 2016.
- [74] S. Zhang, et al., “Mechanical Properties of Copper Thin Films Used in Electronics Devices”, *Procedia Engineering* 10, pp. 1497-1502, 2011.
- [75] K. Timpano, “Mechanical Characterization of Gold Thin Films for RF-MEMS”, 2005.
- [76] M. Cordill, et al. “Fracture and Delamination of Chromium Thin Films on Polymer Substrates”, *Metallurgical and Materials Transactions A*, 2009.
- [77] R. Lucchini, et al. “Delamination phenomena in aluminium/polyimide deformable interconnects: In-situ micro-tensile testing”, *Materials and Design*, pp. 121-128, 2016.
- [78] A. Ababneh, et al., “Electrical and Morphological Characterization of Platinum Thin-Films with Various Adhesion Layers for High Temperature Applications”, *Microsyst. Technol.*, 2017.
- [79] R. Belser, W. Hicklin, “Temperature Coefficients of Resistance of Metallic Films in the Temperature range 25°C to 600°C”, *Journal of Applied Physics* 30, 313, 1959.
- [80] C. Li, P. Hesketh, G. Maclay. “Thin gold film strain gauges”. *Journal of Vacuum Science & Technology A: Vacuum, Surfaces, and Films*, 12, 1994.
- [81] S. Fricke, A. Friedberger, G. Mueller, H. Seidel and U. Schmid, "Strain gauge factor and TCR of sputter deposited Pt thin films up to 850°C," *SENSORS, 2008 IEEE*, Lecce, pp. 1532-1535, 2008.
- [82] R. Padma, et al. “Growth of titanium oxide overlayers by thermal oxidation of titanium”, *Journal of Materials Science* 23, pp. 1591-1597, 1988.
- [83] A. J. Goldberg, “Viscoelastic Properties of Silicone, Polysulfide, and Polyether Impression Materials”, *Journal of Dental Research*, 53(5), 1033–1039, 1974.